MODULATION OF LIKE-CHARGE ATTRACTION BY LIPID AND PROTEIN FUNCTIONALIZED SILICA MICROPARTICLES

by

YUPENG KONG

A DISSERTATION

Presented to the Department of Physics
and the Graduate School of the University of Oregon
in partial fulfillment of the requirements
for the degree of
Doctor of Philosophy

December 2010

"Modulation of Like-charge Attraction by Lipid and Protein Functionalized Silica Microparticles," a dissertation prepared by Yupeng Kong in partial fulfillment of the requirements for the Doctor of Philosophy degree in the Department of Physics. This dissertation has been approved and accepted by:

Dr. Stephen D. Kevan, Chair of the Examining Committee

November 8, 2010

Date

Committee in Charge:

Dr. Stephen D. Kevan, Chair
Dr. Raghuveer Parthasarathy, Advisor
Dr. Hailin Wang
Dr. Miriam Deutsch
Dr. Marina G. Guenza

Accepted by:

Dean of the Graduate School

An Abstract of the Dissertation of

Yupeng Kong for the degree of Doctor of Philosophy

in the Department of Physics to be taken December 2010

Title: MODULATION OF LIKE-CHARGE ATTRACTION BY LIPID AND PROTEIN FUNCTIONALIZED SILICA MICROPARTICLES

Approved: _____

Dr. Raghuveer Parthasarathy

Controlling colloidal interactions continues to receive a great deal of attention due both to basic scientific interests as well as industrial applications. However, many aspects of interactions between microparticles remain poorly understood, including the attraction observed between particles with the same kind of charge (like-charge attraction). This situation hinders progress in the generation of colloidal self-assembled structures.

This thesis focuses on measurements of pair interactions of functionalized silica microspheres and the resulting insights into colloidal interactions. Silica microparticles were functionalized in two ways. For one method, each particle was coated with a lipid bilayer membrane. The charge density of the particle surface can thereby be easily tuned by controlling the type or amount of charged lipids. For

the other method, the cholera toxin subunit B protein (CTB) was bound to lipid-functionalized microparticles.

To measure pair interactions, we invented a line optical trap that enables nearly free one-dimensional Brownian motion of particles. Pair interaction energies of functionalized particles above the bottom of the experimental chamber can be extracted via a Boltzmann relationship.

Both lipid-only and lipid-plus-protein functionalized microparticles show tunable, attractive pair interactions. For lipid-only coatings, the attraction becomes stronger by increasing the fraction of positively charged lipids. There is a linear relationship between pair potential and molar percentage of positively charged lipids. For lipid-plus-protein coatings, attractive potentials were weakened monotonically by binding more CTB. Decompositions of potential curves allow identification of directly charge-dependent and charge-independent contributions to colloidal like-charge attraction.

Analysis shows that the correlations between attraction strength and range are opposite in these two sets of particles. Moreover, the correlations between particle-wall separation and attraction strength in lipid-only and lipid-plus-protein functionalized particles are also opposite. These comparisons show that like-charge attraction may result from more than one mechanism.

Finally, we measured pair potential energies of lipid functionalized silica particles above a lipid functionalized glass chamber bottom, which exhibit a quadratic relationship between the attraction strength and the fraction of positively charged

lipids. Compared with the situation of particle functionalization only, this relation indicates that confinement-induced like-charge attraction can be modulated by altering electrostatic properties of the confining wall.

CURRICULUM VITAE

NAME OF AUTHOR: Yupeng Kong

GRADUATE AND UNDERGRADUATE SCHOOLS ATTENDED:

University of Oregon, Eugene, OR, USA
Institute of Physics, Chinese Academy of Sciences, Beijing, China
Beijing University of Technology, Beijing, China

DEGREES AWARDED:

Doctor of Philosophy in Physics, 2010, University of Oregon
Master of Science in Physics, 2008, University of Oregon
Master of Science in Physics, 2004, Institute of Physics,
Chinese Academy of Sciences
Bachelor of Science in Applied Physics, 2001,
Beijing University of Technology

AREAS OF SPECIAL INTEREST:

Soft condensed matter physics
Biophysics
Advanced microscopy imaging technique
Colloidal physics

PROFESSIONAL EXPERIENCE:

Research Assistant:
Parthasarathy Lab, University of Oregon, 2006 - 2010
Teaching Assistant:
Department of Physics, University of Oregon, 2004-2008
Research Assistant:
Institute of Physics, Chinese Academy of Sciences, 2002-2004

GRANTS, AWARDS AND HONORS:

Highest score prize of PhD's Qualifier Exam, Department of Physics, University of Oregon 2005

Highest score prize of Master's Qualifier Exam, Department of Physics, University of Oregon 2005

Outstanding Undergraduate Student Fellowships (Third Class), Beijing University of Technology 1999

Outstanding Undergraduate Student Fellowships (Second Class), Beijing University of Technology 1998

Outstanding Undergraduate Student Fellowships (Second Class), Beijing University of Technology 1997

PUBLICATIONS:

Yupeng Kong and Raghuveer Parthasarathy, "Different modulation mechanisms of attractive colloidal interactions by lipid and protein functionalization", Langmuir. **26**, 10541 (2010).

Yupeng Kong and Raghuveer Parthasarathy, "Modulation of attractive colloidal interactions by lipid membrane functionalization", Soft Matter **5**, 2027 (2009).

Gregory T. Tietjen, **Yupeng Kong** and Raghuveer Parthasarathy, "An efficient method for the creation of tunable optical line traps via control of gradient and scattering forces",Opt.Express. **16**, 10341 (2008).

Yupeng Kong, Xuechun Lin, Ruining Li,Zuyan Xu, and Xuekun Han, "A novel blue light generation by frequency doubling of a diode-pumped Nd:YAG thin disk laser",Opt.Commun.**237**, 405 (2004).

Lin Xue-Chun, Zhang Ying, **Kong Yu-Peng**, Zhang Jie, Yao Ai-Yun, et.al, "Low-threshold mid-infrared optical parametric oscillator using periodically poled $LiNbO_3$", Chin.Phys.Lett. **21**, 98 (2004).

ACKNOWLEDGMENTS

I want to first thank my advisor Professor Raghuveer Parthasarathy. I joined Raghu's lab in summer 2006 when he started a lab in Physics department. I appreciate the opportunity he gave me to work in his lab and the project to work on to demonstrate my research ability. During the past four years, not only did Raghu's fantastic ideas, insightful suggestions and spiritual encouragements help me to overcome challenges on my research, but also his enthusiasm for science, rigorous scientific attitude and diligence gave me deep impressions and will serve as the standard for my future career.

I would like to thank all other members of my thesis committee — Dr. Stephen Kevan, Dr. Hailin Wang, Dr. Miriam Deutsch and Dr. Marina Guenza, for their interests on my work and helpful suggestions.

I would also like to thank all the people in Parthasarathy lab for their help in my research.

Finally, I want to thank my parents for their encouragements, supports and understandings throughout my graduate study. A special acknowledgment goes to my girlfriend, Wei Wei, who always stands by my side for better or worse.

TABLE OF CONTENTS

Chapter Page

Chapter Page

LIST OF FIGURES

CHAPTER I

INTRODUCTION

1.1 Colloids

1.1.1 Properties of Colloids

A colloid is a kind of mixture, in which one substance is distributed uniformly throughout another. The diameters of dispersed particle in colloidal system are usually in the range between 10nm and 10μm, which are substantially larger than that of atom, ion or ordinary molecule. Colloidal systems are homogeneous mixtures, which means that particles are distributed uniformly in dispersion media. Considering all possible phase (gas, liquid, solid) combinations between dispersed particles and dispersion medium, there are eight categories of colloidal systems except gas/gas dispersion. For example, sol (i.e. ink, paint) is the system with solid particles dispersed in liquid. If immiscible liquid droplets are dispersed, an emulsion (i.e. mayonnaise, milk) can be formed, whereas gas particles in liquid are known as foam (i.e. soap foam).

Due to the size of dispersed particles, colloidal systems have some important properties. Colloidal particles undergo Brownian motion, which was first studied

by Robert Brown when he observed pollen suspensions in 19th century. Brownian motion is a visible exhibition of the motion of solvent molecules, as colloidal particles gain kinetic energies by collision with surrounding molecules. Consider a colloidal particle with momentum $\vec{p}$ and mass m, its motion can be described by Langevin equation [1, 2].

$$\frac{d\vec{p}}{dt} = -\frac{\gamma}{m}\vec{p} + \vec{f}(t) \tag{1.1}$$

The net force exerted on the particle is the sum of friction force $-\frac{\gamma}{m}\vec{p}$ and a random force $\vec{f}(t)$ due to collision. The time-average of the random force vanishes $\langle \vec{f}(t) \rangle = 0$. For a particle of radius a, friction coefficient $\gamma = 6\pi\eta_0 a$, where η_0 is the viscosity of solvent. Deduced from Langevin equation, the mean squared displacement of particles can be expressed as

$$\langle \vec{r}^2 \rangle = 6D_0 t \tag{1.2}$$

where D_0 is the diffusion coefficient which can be written by Einstein relation

$$D_0 = \frac{k_B T}{\gamma} = \frac{k_B T}{6\pi\eta_0 a} \tag{1.3}$$

The time τ for a particle to diffuse over distance comparable to its radius a will be on the order of second. Colloidal particles are big enough to be observed under optical microscope. However, their Brownian motions imply that energy equipartition theorem can still be hold for them as well as for atoms or molecules. Therefore, colloidal systems can be visible models [3, 4] for nucleation, cystallization or phase

transition of atomic or molecular systems, imaging of colloids have provide some understandings of properties of glassy materials [5, 6].

Unlike a solution, if a light beam penetrates a colloidal suspension, it will trace a visible light path. Because the scale of colloidal particles are comparable with that of the wavelength of light, light will be scattered by particles in all directions. This is called Tyndall effect [7], which was used for ultramicroscope [8] to detect motions of small particles. Another consequence of the similarity between particle size and optical wavelength is that, colloidal particles can be used to create photonic band gap crystals [9, 10, 11]. In these periodic dielectric structures, there is a frequency of light, in which electromagnetic waves are forbidden to transmit. Therefore, such materials can guide and control light propagation.

Another important property of colloidal systems is stability against aggregation. When immersed in an eletrolyte solution, most colloidal particles are electrically charged. Surface charges can come either from the ionization or dissociation of surface groups, or the absorption of ions in solutions. For example, surface of silica in water can be negatively charged by dissociation of silanol group [12]

$$SiOH \rightleftharpoons SiO^- + H^+ \tag{1.4}$$

Counterions in solvent can be attracted to form diffuse electrical double layers around charged particle surface. The resulting repulsive Coulomb interaction can compete with attractive Van Der Waals interaction to keep particles from

aggregation. This theory was first proposed and elaborated by Derjaguin, Landau, Verwey and Overbeck and named as DLVO theory [13, 14]. The potential energy of particles is the sum of the two mentioned interactions above. There are also some non-DLVO interactions between colloidal particles, such as steric interactions and hydration interactions, which also play important roles in stabilizing colloidal dispersions. Colloidal interactions can affect lots of industrial applications. For example, water can be purified by adding aluminum ion (Al^{3+}) to attract negatively charged impurities, which will coagulate and be filtered out. Colloidal particles coated with certain hydrophilic polymers can escape the capture of body's immune system. Consequently, drugs, carried by such particles, can achieve longer blood circulation times and reach sick organs or tissues.

1.1.2 Like-charge Attraction

Colloidal interactions have been investigated intensively, not only due to their important roles in phase behaviors of colloidal suspensions, but also for their potentials in industrial applications. However, some interactions still remain unclear. According to DLVO theory, colloidal particles, with the same sign of charges (positive or negative) in monovalent electrolyte solutions, should always exhibit long-range repulsions due to electrolyte-mediated Coulomb interactions (In a short separation between particles, Van Der Waals attraction can be significant). In fact, unexpected attractions between such particles, called like-charge attraction, have

been observed not only in hard-sphere colloidal dispersions [15, 16, 17] but also between biomolecules in solutions [18, 19].

Like-charge attraction was first reported by Kepler and Fraden in 1994 [15]. In their experiments, polystyrene particles were confined between two glass plates in a H_2O/D_2O (1:1) solution. Pair potentials, obtained from pair-correlation function, show a long-range (in μm scale) attractive interaction between particles, which is at least 100 times larger in magnitude than Van Der Waals attraction. Since then, various confined systems, in which, colloidal particles were confined by single [16, 20] or double [17, 21] charged glass walls, have been used to experimentally study like-charge attraction.

Confinement-induced like-charge attraction has also attracted attentions of theorists. The presence of a confining wall, often of the same charge sign as the particles, appears necessary to generate colloidal attractions. However, DLVO theory, which has successfully described interactions between isolated particles, failed to account for such mysterious colloidal attractions under confinements. Squire and Brenner [22] attributed like-charge attraction observed in Larsen's experiments [16] to hydrodynamic coupling. When one particle moves away from the wall, the surrounding liquid flow will pull the other particle nearby, which causes the appearance of the attractive well in the pair potential. However, this explanation cannot be applied to double-wall system, and since such hydrodynamic coupling relates with repulsive particle-wall interaction, the magnitude of resulting attraction

cannot be so large as they thought. Some calculations [23] also show stronger, long-range attractive interactions followed by the increased particle densities. In this case, such attraction was attributed to the coupling between charged particles and induced counterion distributions. It has been speculated that the densely packed particles can be analogous to the charged wall in the generation of colloidal attractions. However, no related theoretical work has been proposed to account for attractions between pair of like-charged colloidal particles under confinement in solutions with low salt concentrations. Grier, who thought this attraction was due to the interaction between electrical double layers of charged wall and particles, suggested an phenomenological form [20, 24] to explain this wall-mediated attraction, in which, the experimentally observed attraction can be interpreted via a supposed charge density due to the nonuniform conterion distributions around particles. However, confinement-induced like-charge attraction is still an unsolved mystery in colloidal science. It should depend on the properties of particle, confining wall and surrounding solutions. These factors, especially the properties of particle itself, have not previously been systematically varied in experiments. An important biomaterial, lipid membranes, can provide a means of addressing these issues.

1.2 Lipid Bilayer

1.2.1 Properties of Lipids

Lipids are the primary structural constituents of cell membranes. The structure

of lipid molecules shows them an amphiphilic nature, which can be broken down into two main components. One is a polar, hydrophilic head; the other is an apolar, hydrophobic tail. Hydrophilic head and hydrophobic tail are covalently linked by a glycerol group. Hydrophilic head may contain some charged groups, like phosphate, choline...etc. There are a variety of lipids with various charge arrangements in their headgroup. Phosphatidylcholine (PC), sphingomyelin (SM) and phosphatidylethanolamine (PE) are the most common lipids in biological membranes, their heads have both positively charged and negatively charged groups without net charges. Such lipids are called ziwitterionic lipids. For other lipids, their headgroups maybe have net negative charges (e.g. phosphatidylserine (PS)), positive charges (e.g. sphingosine) or lack charged residues (e.g. diacylglycerol). Hydrophobic tails are composed of one or two fatty acid chains, on average, 14 to 20 carbon atoms per chain. Fatty acid chains can be saturated or unsaturated. Lipid tails can be defined by the length and degree of saturation of hydrocarbon chain. Both PC and PE lipids have two fatty acid chains, each of which usually has an unsaturated carbon-carbon bond. The presence of unsaturated bond reduces the number of possible configurations of fatty acid chains, which yields an increased volume occupied by tails.

When lipid molecules expose to aqueous environments, their headgroups show affinity to water molecules, whereas, non-polar fatty acid chains will repel water due to the high entropic cost of ordering water near the chains. At low concentrations,

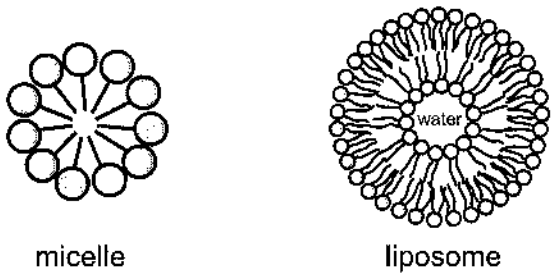

FIGURE 1.1: Cross sections of a micelle and a liposome. Hydrophobic single-chain tails are enveloped in the center of micelle. For the liposome, an aqueous core is enclosed by lipid bilayer. In each plot, circles and lines represent hydrophilic heads and hydrophobic tails, respectively.

lipid molecules will exist as monomers. Aggregation will be triggered by the reach of the critical concentration. The shape of aggregation is strongly influenced by the structure of lipid molecule. Single-chain lipids, with a critical concentration of 10^{-6}M usually form micelles. In contrast, lipids with two fatty-acid chains have a lower critical concentration (about 10^{-10}M) and usually form bilayers with a thickness of 4$\sim$5nm. Without confining surfaces, lamellar bilayers will form a closed structure to minimize the contact between hydrophobic core and water. The closed lipid body in three dimension is called lipid vesicle or liposome. The difference between micelle and lipid vesicles are shown in Fig.1.1. Instead of a hydrophobic core in micelle, there is an amount of solution trapped inside lipid vesicle.

1.2.2 Supported Lipid Bilayers

The real cell membrane is a complex structure, which is primarily composed of phospholipids and proteins with small amount of other molecules, such as

carbohydrates. Our current understandings of cell membrane are based on fluid mosaic model, proposed by Singer and Nicolson in 1972 [25]. Phospholipids are organized in the form of bilayers, which are fluid in the membrane plane. Various proteins can incorporate into lipid bilayer in different ways: Peripheral proteins are attached to the membrane surface, whereas transmembrane proteins penetrate through membranes and connect intra- and extra- cellular environments. Cell membrane exhibits heterogeneity across lipid bilayers. Unlike outer leaflet of bilayer, which mainly consists of zwitterionic lipids (e.g. PC, SM), many lipids in intracellular side are charged (e.g. PS). Such properties of cell membrane are very important to maintain cell functions. Lipid bilayer serves as a barrier to separate cell's interior from outer environments, proteins can make membrane selectively permeable to substances. In this way, cell machinery can transport stuff across membrane in a controlled way.

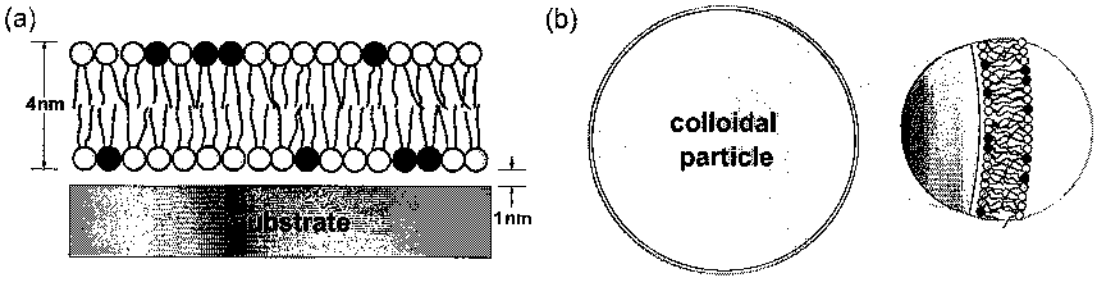

FIGURE 1.2: (a) The deposition of lipid bilayers on planar substrate. There is a thin water layer (1nm) between substrate and hydrophilic heads of lipids. (b) Self-assembly of lipid bilayers on colloidal particle. The type of lipid is denoted by the color of its hydrophilic head.

Supported lipid bilayer has been widely used to model real cell membranes

since early 1980s [26, 27, 28, 29]. Harden McConnell's group [27] first developed a lipid bilayer system on an oxidized silicon. Lipid bilayers were usually deposited on substrates with hydrophilic surfaces, such as fused silica [27, 30], mica [31, 32], borosilicate glass [27, 33] or oxidized silicon [27]. Sometimes soft polymers were inserted between lipid bilayers and substrate to serve as a cushion to minimize membrane-substrate interactions [34] or keep transmembrane proteins from contacting with substrate [35, 36]. The fusion of small unilaminar vesicles (SUVs) [27, 37] is the most common method to form supported lipid bilayers. SUVs first adhere to the surface of substrates, then they will rupture [37] and self-assemble on the substrate to form supported lipid bilayer (Fig.1.2(a)). We will discuss the method to make supported lipid bilayer in later chapters. The process of vesicle deposition and rupture depend on properties of lipids, substrates and surrounding solutions [33, 38]. Interactions involved in this process include electrostatic, Van Der Waals as well as hydration interactions. Instead of being tightly bound, the lipid bilayer is separated from substrate by a thin layer (1nm) of water, which is very important to keep it fluid. The fluidity of supported lipid bilayer can be easily quantified by fluorescence recovery after photobleaching (FRAP) techniques [39]. An area of fluorescence-labeled lipid bilayers is photobleached, Brownian motion will made the fluorescent lipids outside diffuse in, finally, the fluorescence of the photobleached area can return. The fluorescence recovery time can be used to determine the diffusion coefficient of fluorescence-labeled lipids. The measured diffusion coefficients

of supported lipid bilayer are about $1\sim10\mu m^2/s$. Stabilized and confined by substrates, lipid bilayer is still a fluid with the feasibility of protein incorporation, and asymmetric lipid distributions can also be made [40]. Therefore, the environment of cell membranes can be mimicked. Such structure can make lipid bilayers be easily accessed by imaging systems, such as atomic force microscopy(AFM) [38, 41] and total internal reflection florescence microscopy(TIRFM) [42, 43]. Not only can molecular interactions [43, 44] happening on surfaces be precisely probed, but also some important processes in cell biology, such as membrane fusion [45, 46], cell adhesion and signaling [29, 47] can be studied.

1.3 Research Motivation on Like-charge Attraction

Despite of studies over last two decades, confinement-induced like-charge attraction is still poorly understood. The whole system consists of colloidal particles, confining wall and electrolyte solutions, which seems simple. However, the relations between attractive potentials and some properties of the system components are still not well investigated. For example, in Larsen's experiments [16], the interaction between $0.65\mu m$ diameter polystyrene particles is purely repulsive when the distance between glass chamber bottom and particle is $9.5\mu m$, instead, decreasing the distance to $2.5\mu m$, there is an attractive interaction between particles. However, what does the interaction look like with particle-wall separations between $2.5\mu m$ and $9.5\mu m$, which span several particle's diameters? what is the relationship

between the magnitude of attractive interaction and particle-wall separation? In previous experiments, controlled parameters were the ionic strength of solutions [20], particle-wall separation [16, 21], particle density [15, 48], and not intrinsic properties of particles themselves, such as surface charge density. We believe that this lack of particle control has contributed to the lack of satisfactory explanations for confinement-induced like-charge attraction. To provide more insights into such a mysterious phenomenon, we need an experimental system with tunable, attractive colloidal interactions.

The lipid and protein functionalization can be a good candidate for our needs. Fluid lipid bilayers can self-assemble on the surface of a colloidal particle shown in Fig.1.2(b). Deposited on colloidal particles, lipid bilayers are more stable and uniform than liposomes, which makes this cell-like structure a good cell membrane model [49, 50], and it can also be applied in biosensing [51] and drug design [52]. The electrostatic properties of colloidal particles, i.e. surface charge density, can be easily, finely adjusted by tuning the lipid composition. Bound peripheral proteins on the surface can provide additional specific linkages between particles in addition to the adjustments of lipids distribution and surface fluidity. Moreover, Some experiments have already shown that lipid and protein functionalization can trigger phase transition [53, 54] in many-body colloidal dispersions, which implies that surface lipids and proteins can alter interparticle interactions. Therefore, lipid bilayers and bound proteins could be powerful tools to control colloidal interactions.

1.4 Dissertation Goals and Accomplishments

This dissertation presents an experimental investigation of confinement-induced like-charge attraction. With an emphasis on modulation process, we attempt to provide more profound understandings about this question. Unlike previous experiments, we want to control attractive interactions by modifying surface properties of colloidal particles, i.e. particle functionalization. Biomolecules, especially protein and DNA, has been used for a while to control colloidal interactions due to their variety and binding specificity. However, such controls were either poor or only in a short range, which cannot meet our needs. Lipid bilayers supported by colloidal particle shed a new light on the control of colloidal interactions. Surface properties of colloidal particles can easily controlled by lipid and protein as mentioned above.

In our experiments, two different kinds of functionalized particles were used, lipid-only-coated silica particles, in which, colloidal surface charge density was modulated by the control of charged lipid compositions, and lipid-plus-protein-coated particles, in which, the amount of proteins bound on surface was controlled. Instead of quantifying interparticle interactions via many-body measurements, we want to determine the fundamental pair interactions of such particles under a confinement of single wall.

Optical tweezers have long been used to characterize colloidal interactions. We invented a new set of tunable line optical tweezers via holographic optical tweezers (HOTs) technique to facilitate our pair interaction measurements. Pair interaction

can be deduced from the probability distribution of particle's center-to-center separations. The applicabilities of line trap setup and method to figure out true pair interaction energies were first demonstrated by measuring pair potentials of bare silica particles.

Both lipid-only and lipid-plus-protein functionalized silica microparticles were found to show long-range, tunable, attractive pair colloidal interactions. The linear relation between attractive depth and molar percentage of charged lipids in lipid-only case allowed us to separate charge-dependent and -independent terms of pair potential, which yields a purely repulsive interaction for the charge-dependent term. A similar procedure of term separation was also applied to lipid-plus-protein case.

We employed reflection interference contrast microscopy (RICM) to measure mean separations between particles and confining chamber wall. The revealed different relationships between attractive depth and mean height, or effective attractive range for the two particle types, imply that maybe not only one mechanism is in charge of confinement-induced like-charge attraction.

Our data indicate that particle-wall interaction dominates pair potential measurements. To further quantify the effect of confining wall on colloidal pair potential measurements, we deposited lipid bilayers with different compositions on glass bottom of chamber. The subsequent experiments show these modifications can modulate like-charge attraction between two lipid-coated silica microparticles.

1.5 Dissertation Overview

In Chapter II, after a short historical introduction of optical tweezers, we will first discuss the theory of optical trapping, Following that, studies of Brownian motion of a colloidal particle in a single point trap will be presented. Holographic optical tweezers (HOTs) technique will be discussed in the last part.

The method to measure pair colloidal interactions will be discussed in Chapter III, we will first overview DLVO theory and analyze possible existing interactions between micron-size silica particles. Then the setup of line optical traps will be discribed after a short review of previous methods in pair interaction measurements using optical tweezers. Before we present our measured pair potentials of bare silica particles, we will analyze all the possible factors that will affect pair interaction measurements, and the corresponding methods or procedures to eliminate such effects. The generation of tunable line trap has been reported with G.T.Tietjen and R.Parthasarathy in Optics Express [55].

In Chapter IV, RICM technique will be introduced. The principle and the validation of the methods to measure particle-wall separation by single-wavelength RICM will be presented.

Pair interaction energy measurements of lipid-only functionalized silica particles will be presented in Chapter V. Following the introduction of experimental methods, colloidal pair interactions tuned by lipid compositions will be shown. The linear relationship between the colloidal pair potential and the fraction of charged lipids

allows us to decompose interaction energy into charge-dependent and -independent terms, in which the interaction related with lipid charges is purely repulsive. Results shown in this chapter have been reported with R.Parthasarathy in a published paper[56].

In Chapter VI, we will first introduce tunable pair colloidal interactions by lipid-plus-protein functionalization, Similar as lipid-only functionalized microparticles, pair interaction energies of CTB-bound particles can be also decomposed into CTB- and membrane-related terms. Then, two sets of tunable like-charge attractions by lipid-only and lipid-plus-protein functionalization will be compared. We find that the relationships between the depth of attractive potential and effective attractive range are opposite. Furthermore, we measured particle-wall separations via RICM, the opposite relationships between the depth of attractive potential and mean height of particle in these two kinds of functionalization suggest that more than one mechanism may be in charge of confinement-induced like-charge attraction. Results shown in this chapter have been reported with R.Parthasarathy in a published papers [57].

In Chapter VII, we will introduce pair potential measurements of lipid-coated silica particle confined by electrostatically-modified chamber bottoms, which were also coated with lipid bilayers to tune charge densities. Our data indicate the modified electrostatic properties of confining wall can modulate like-charge attractions between colloidal particles.

We will draw the conclusion and give some directions for future work in Chapter VIII.

CHAPTER II

OPTICAL TWEEZERS

Most of experiments described in this dissertation are related with optical tweezers. In this chapter, we will first provide a basic overview emphasizing on the physics of optical trapping. Holographic optical tweezers (HOTs) is a recently developed technique to control positions of multiple point optical traps in three-dimension, which were implemented by us and others using liquid crystal spatial light modulators (SLMs). We will describe the use of SLMs to modulate optical wavefronts and the method to generate phase masks. Finally, after a description of HOTs system setup in our lab, we will investigate the motions of a silica microparticle trapped in a single point trap.

2.1 Introduction

The origin of optical tweezers comes from the study of radiation pressure. According to quantum theory, light can behave like particles, each of which possesses a momentum p,

$$p = \frac{h}{\lambda} \tag{2.1}$$

where h is the Planck constant, and λ is the light wavelength. Due to forces exerted by radiation pressure on objects, momentum will be transferred from photon to objects

upon their collision. Ashkin, the pioneer in laser-based optical trapping, designed a series of experiments to examine particles' motion under radiation pressure forces in the 1970s [58, 59]. In his experiments, he found an unexpected force acting on latex particles near a focused argon laser spot, which could pull the particle from the edge to the center of focus. This force, later known as the gradient force, leads to the development of optical tweezers.

Optical tweezers are powerful tools to control and manipulate the motion of roughly micron-size objects. With lasers and couple of lens, by focusing laser beam through objective lens in an inverted microscope, a single-point trap system can be simply set up. Depending on laser power, optical trap can provide gradient forces that are large enough to suppress particle's Brownian motion and gravity. Motions of dielectric particles, as small as 25nm [60] in diameter, can be confined. Viruses [61], bacteria [61, 62] and cells [63, 64], which do not have regular, uniform geometries, can also be trapped without damage. The strength of trap can be modulated by laser power, whereas, beam steering systems, such as scanning mirrors, acoustic-optic deflector (AOD), can provide precise, real-time control of the trap position. Trapped objects can be easily manipulated and moved laterally in focusing plane.

Combined with high-resolution imaging systems, the position of a trapped microparticle can be determined with nanometer precisions. Therefore, Forces applied on it, as small as several piconewtons, can be detected. This property makes optical tweezers useful for measuring forces related with motions of biomolecular

motors, or mechanical properties of biomolecules. One of such experiments was done by Svoboda et.al. [65], who found that single kinesin molecule walks along a microtubule with each step of 8nm. In these similar experiments, trapped beads were attached to molecules, real-time displacements of particle away from trapping center were tracked, which can reveal the subtlety of biomolecular motions. The hidden biomolecular interactions can thereby be easily probed.

2.2 Optical Trapping Physics

The most common method to make optical trap is focusing a laser beam through an objective lens. Consider the Mie scattering regime [58], in which, the radius of particle a is much larger than wavelength λ ($a \gg \lambda$). When a dielectric particle is near the focused spot, it will experience two kinds of forces due to momentum transfer from photon to it. When light is incident on the particle surface, photons involved in reflection will give a momentum to particle along light propagation direction, and the resulting force, scattering force F_s, will push the particle away from focus. Some of the light is also transmitted through the particle. Indexes of refraction are usually different between particle and outside environment, which will make propagation direction of transmitted light different from that of incident light. The resulting momentum change of photons after transmittance will also exert a force on particle, which is called gradient force, F_g. If index of refraction of particle is greater than that of surrounding medium, gradient force will be along the direction of intensity

gradient and pull particle to the center of focus, where the light intensity is the highest. Otherwise, it will push the particle away from focus. Propagating beam ray trajectories and resulting forces exerted on particles are shown in Fig 2.1.

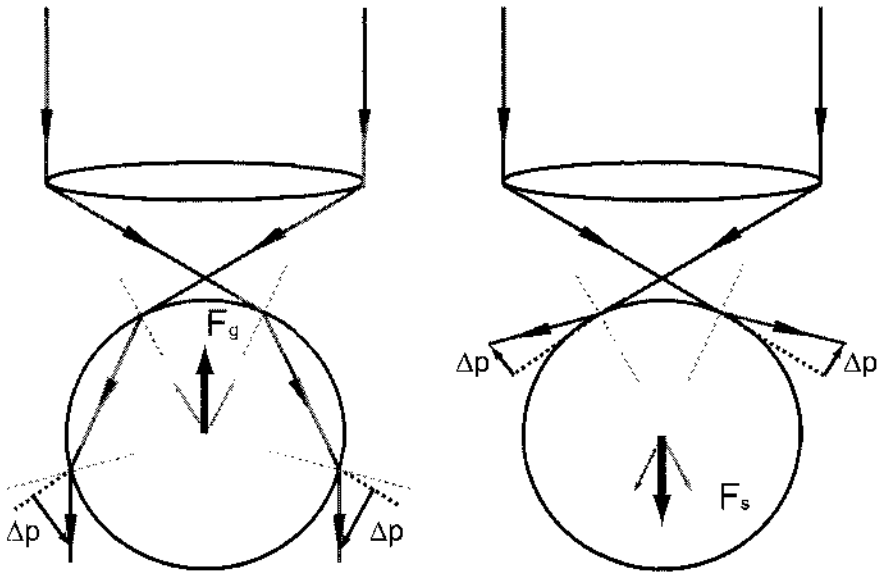

FIGURE 2.1: Interactions between a dielectric particle and beam rays near focus. The gradient force F_g originates from the refraction of light through particle. Light reflection on the surface of particle gives rise to scattering force F_s. Δp denotes the change of light momentum.

Force analysis in the Rayleigh regime, in which particle's size is much less than light wavelength ($a \ll \lambda$), can offer the physical insight of optical trapping. Dielectric particles can be simplified as an induced point-dipole in electromagnetic fields. The dipole moment $\vec{P}(r,t)$, induced by electromagnetic fields $\vec{E}(r,t)$, can be expressed as [66, 67]

$$\vec{P}(r,t) = 4\pi n_2 \epsilon_0 a \frac{m^2-1}{m^2+2}\vec{E}(r,t) \tag{2.2}$$

where ϵ_0 is the dielectric constant in vacuum, a is the radius of particle, and $m =$

n_1/n_2 is the ratio of refractive index of particle and medium. Gradient force comes from the interaction between induce-dipole and electric field, which is similar to forces involved in dipole alignment in electrostatics.

$$\vec{F}_g(r,t) = [\vec{P}(r,t)\cdot\nabla]\vec{E}(r,t) = 2\pi n_2\epsilon_0 a\frac{m^2-1}{m^2+2}\nabla^2\vec{E}(r,t) \tag{2.3}$$

The force exerted on particle can be derived from the time-average of above equation.

$$\vec{F}_g(r) = \pi n_2\epsilon_0 a\frac{m^2-1}{m^2+2}\nabla I(r) \tag{2.4}$$

where $I(r)$ is the intensity of light. First, the above equation clearly shows the dependence between the magnitude of gradient force and the intensity gradient. Moreover, a particle can move towards or away from focus under gradient force, which is determined by the refractive index of particle relative to its surrounding medium. The induced dipole also follows the oscillation of external electric field, which results in the emissions of electromagnetic waves. The field generated by oscillating dipole will interact with external field, which gives rise to the scattering force, F_s [67]

$$\vec{F}_s(r) = \frac{n_2}{c}\sigma I(r)\hat{z} \tag{2.5}$$

where c is light speed in vacuum, and σ is the scattering cross section, given by

$$\sigma = \frac{8\pi}{3}\frac{a^6}{\lambda^4}\left(\frac{m^2-1}{m^2+2}\right)^2 \tag{2.6}$$

The scattering force is along the direction of light propagation, and proportional to light intensity.

In the Mie regime, although above formula are not valid, trapped objects are still balanced by gradient force and scattering force. To stably trap micron-size objects, first, refractive index of objects should be higher than that of surrounding medium ($n_1 > n_2$), which guarantees that the direction of gradient force points to the focus center. Then, the gradient force must be greater than the scattering force $F_g > F_s$, which can keep the trapped object from escaping. In experiments, an objective lens with high numerical aperture (NA) is usually used. Due to its high convergence angle, the focused beam spot can have a steep gradient, which can overcome scattering force and make objects tightly trapped.

2.3 Holographic Optical Tweezers

Since their first demonstration in 1986 [60], optical tweezers have opened a new avenue for studying microscopic phenomena involved in cells, biomolecules and colloids. Some developments have enhanced the ability of optical tweezers to trap multiple objects and objects with non-standard geometries. Double-point optical tweezers [68] can be constructed by focusing two split beams from a laser through objective lens. With a beam steering system equipped in each optical path, these two traps can be separately controlled. Two trapped beads connected by biopolymers is a very common setup in biomolecular interaction measurements with high stability. One of dual trap setups reported by Moffitt et.al. [69] reaches an angstrom-scale spatial resolution. Moreover, the generation of multiple point optical traps can favor

studies involved in many-body systems, such as cell ensemble and colloidal dispersion. In these situations, a well-controlled ensemble can be achieved by introducing optical trap arrays. Each individuals are trapped simultaneously with a well-defined distribution, which can provide a reproducible, consistent initial ensemble state for study. Acoustic-optical deflector (AOD) is a widely used equipment to deflect a laser beam with a repetition rate of kilohertz. Particles at multiple spots can be trapped in a 'time-shared' style [70], if the timescale of laser beam deflection is much smaller than that of particles' Brownian motion. However, besides the complicated setup of optical trap array based on AOD , the increase of number of trapping sites requires a faster scanning speed, whereas, focused beam needs to spend sufficient time in each site to guarantee a stable trapping. Compromise of these two factors will limit the number of effective trapping sites. The need to generate optical trap array in a more effective way drove the development of Holographic Optical Tweezers (HOT's) technique.

The pioneer work in HOTs was done by Fouriner in 1995 [71] when he created multiple optical traps with a glass hologram. Glass-etched diffractive optical elements (DOE) [71, 72], encoded with spatial phase profiles, were directly illuminated by laser. With the wavefront modulated by DOE, incident beam, by transmission or reflection, can be diffracted to form desired intensity distribution (i.e. multiple optical traps) near the focal plane of objective lens. However, for each given spatial distribution of optical trap array, a hologram needs to be made with corresponding phase profile. A

hologram library is needed to perform desired control of trapping system, which is very inefficient, and such control are limited by hologram scanning rate. Therefore, in order to dynamically manipulate each individual traps, lately, computer-based DOEs [73, 74, 75], especially spatial light modulators (SLM) began to appear.

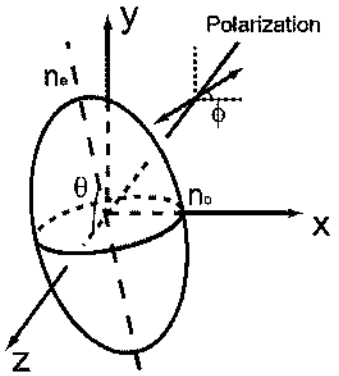

FIGURE 2.2: Refractive index ellipsoid of liquid crystal for a linear polarized light beam propagating along z-axis. See text for details of denotations.

SLMs are devices that can modulate the wavefront of an incident light beam. Each pixel of SLM is made by nematic liquid crystal which is uniaxial. One axis, which is the director, is longer and preferred with index of refraction n_e, the other two axis are equivalent with index of refraction of n_o. Therefore, when traveling inside liquid crystal, incident beam with certain polarization direction will break down into two components with different traveling speeds, which is called birefringence. Let us consider this situation shown in Fig.2.2. A linear polarized beam travels along z-direction into a liquid crystal with an angle ϕ between its polarization direction and x-axis. The director of liquid crystal locates in y-z plane and forms an angle θ with

z-axis. According to its polarization direction, the beam can be decomposed into two parts, x-components propagates with refractive index of n_o, and y-component propagates with refractive index of $n(\theta)$, which can be expressed by

$$n(\theta) = n_o n_e (n_e^2 \cos^2\theta + n_o^2 \sin^2\theta)^{-1/2} \tag{2.7}$$

Therefore, after these two components recombine together upon emerging from liquid crystal, not only the polarization state of the beam possibly has changed, but also a phase shift, which depends on the orientation of liquid crystal, happens

$$\Delta\phi = \frac{2\pi}{\lambda}(n(\theta) - n_o)d \tag{2.8}$$

where λ is the light wavelength and d is the thickness of liquid crystal sample. Note that if the polarization direction is parallel or perpendicular with the direction of director, no phase shift (birefringence phenomena) will happen. The possible phase shifts should be between 0 and $\frac{2\pi}{\lambda}(n_e - n_o)d$. Therefore, to realize phase modulations in a full 2π range, first, SLM must be illuminated by a linear polarized beam. Second, its thickness needs to be appropriately selected. Usually, reflective SLM was adopted due to its efficiency, in which the contribution of thickness to phase shift is doubled due to reflection.

A liquid crystal flows like ordinary liquid, but its orientation can be easily aligned by an external electromagnetic field. θ mentioned above, can be set by applied voltage, which consequently can control phase shift of reflected light. For computer-based SLM control, voltage applied on each pixel depends on its grey level value assigned

by computer. The HOLOEYE 1080P SLM used in our experiments has a 1920×1080 pixels resolution with a 8 μm pixel pitch, and it can provide 8-bit grey-level phase control. The possible gray-level values assigned to each pixel are integers between 0 and 255, each of which can address different applied voltages , then the resulting phase shifts relevant to tilted angles of each pixel can be a series of discrete values at an interval of $\frac{2\pi}{2^8}$in a full 2π range. Therefore, phase of reflected light can be finely manipulated pixel by pixel. The resulting phase shift distribution on SLM , which is encoded by gray-level value on each pixel, can modulate the wavefront of reflected beam to form a desired intensity distribution on the focal plane of objective lens.

Strictly speaking, phase mask displayed on SLM should be calculated from inverse Fourier transform of the desired intensity distribution on focal plane. It is seldom that an analytic solution for corresponding phase distribution can be found, instead, iterative algorithms needs to be applied to numerically reconstruct wavefront. Luckily, only two simple, analytically solvable phase masks are often sufficient to generate multiple point traps in three-dimension. If the position of a pixel in SLM plane can be denoted by $\vec{\rho} = (\mu_j\ ,\ \nu_k)$, the phase of a single point trap appearing at $\vec{r_p} = (x_p\ ,\ y_p)$ in focal plane can be expressed by a phase function that varies linearly with position [75].

$$\varphi_{prizm}(x_p, y_p) = \sum \frac{2\pi}{\lambda f}\vec{\rho} \cdot \vec{r_p} = \sum_{j,k} \frac{2\pi}{\lambda}(\mu_j \frac{x_p}{f} + \nu_k \frac{y_p}{f}) \tag{2.9}$$

In this case, the function of SLM is similar to that of prism, which diffracts a beam to focus on any desired positions in focal plane. To move single point trap out of focal

plane, the phase of Fresnel lens needs to be applied

$$\varphi_{lens}(z_p) = \sum \frac{2\pi\rho^2 z}{\lambda f^2} = \sum_{j,k} \frac{2\pi(\mu_j^2 + \nu_k^2)z_p}{\lambda f^2} \tag{2.10}$$

where z_p is the displacement of a trap away from focal plane. Phases of each single trap need to be added together to generate optical trap array.

$$\varphi = \sum_p \varphi_{prizm}(x_p, y_p) + \varphi_{lens}(z_p) \tag{2.11}$$

Due to the phase superposition, each individual trap can be controlled independently by modifying corresponding part of phase mask.

Compared with AOD, the control of computer-based SLM to generate multiple point traps has two advantages. First, instead of single-beam scanning with AOD, each trapping site generated by SLM is formed by a static focused spot. Due to the lack of time-sharing, more effective point traps can be generated with a relative low laser power. Second, optical array layers can be generated by AOD with a partial control in three dimension [70], which is based on a complicated optical design. In comparison, A true three-dimensional control of multiple point traps can be easily achieved by the input of phase masks on SLM. Phase superposition allows independent control of each individual trap. In addition, the nature of phase modulation enable SLM to generate some novel optical trap geometries. For example, optical vortex beams [76] carry orbital angular momentums, which can make trapped particles rotate around their axis. However, the dynamic control of SLM is limited by its relatively low refresh rate, which is about 60Hz.

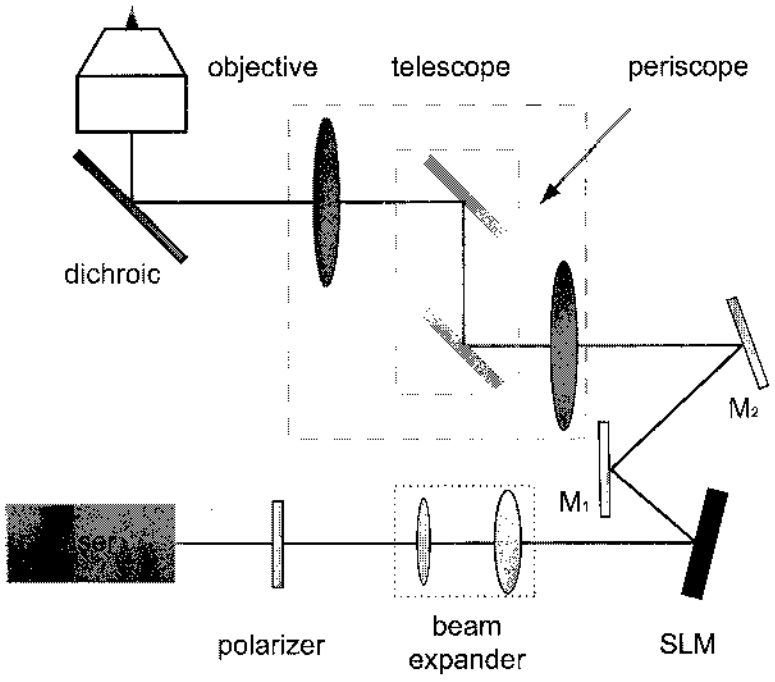

FIGURE 2.3: A schematic diagram of HOTs system setup. See text for details

2.4 System Setup

The schematic of our HOTs system setup is shown in Fig.2.3. Optical tweezers were powered by a diode laser (Meshtel RS655-70) with a wavelength of 655nm and maximum output power of 70mW. Its transverse beam profile is circular with a diameter of 2.5mm. In order to make the beam cover the maximum area of SLM, which is 16.6 $\times$ 10.2 mm^2, an 4X beam expander, consisting of two convex lens, with focal lengths of 15mm and 60mm, respectively, was inserted into optical path following a polarizer. The laser beam illuminated SLM with such a small incident angle ($\theta < 10°$) that the resulting additional phase shift can be neglected. Then the

beam with the modulated wavefront, steered by two mirrors M_1 and M_2, was coupled through a telescope system, which is composed of two convex lens with the same focal length of 250mm and elevated by a periscope. After reflected by a 45° dichroic mirror, finally, it was focused by a water-immersion objective lens (Nikon, NA=1.2, 60X) on an inverted optical microscope (Nikon TE-2000). Images were captured by a CCD camera (Optronics Microfire). After calibration, we found that the ratio between the number of pixels and the actual spatial interval for this camera equals to 8.1 pixels/μm. Phase masks were generated by home-made MATLAB program, and via a monitor output splitter they can be simultaneously displayed on SLM as well as a monitor, which can make them visualizable.

We want to further comment on our design. The front lens used in beam expander was an aspherical lens, which can help decrease spherical aberration due to its small focal length. In addition, large aperture lens can help decrease nonparaxial aberration. Lens with diameter of 2 inches were used in telescope system, which can make beam be easily aligned to pass through their centers. A band pass filter was also put inside the eye side of microscope to protect eyes from laser damage. When SLM is not addressed, acting only as a conventional mirror, The efficiency of 0th order is about 60%, which means 40% of the incident intensity is lost. By adding intensity losses from other optical elements (mainly from the polarizer and the dichroic filter), we roughly estimate that at most, 20% of the intensity emitted from laser is left on the focal plane of objective lens.

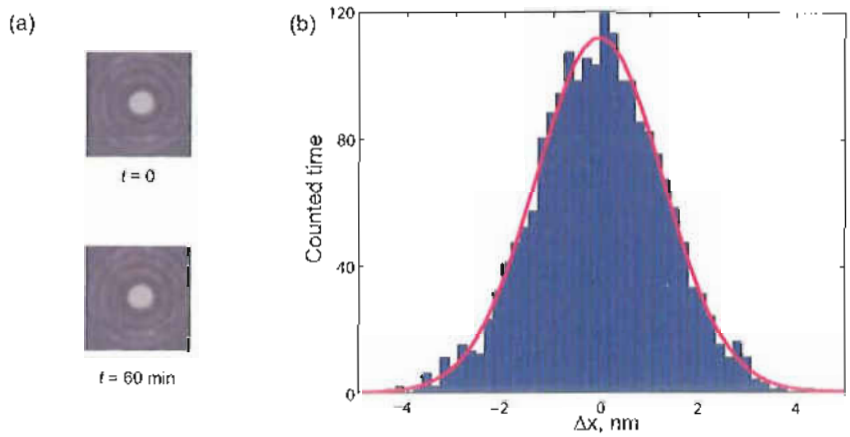

FIGURE 2.4: (a) Profiles of focused laser beam through objective lens show the absence of focus drift in one hour. (b) Histogram of tracked positions for a stuck particle with 3.2 μm in diameter. The red line is a Gaussian fit.

Stability is another experimental concern. For our later experiments, we usually need to observe Brownian motion for hours, which requires a focal plane with high mechanical stability in a long term. Our original stage (Nikon) had a large focal drift and so we replaced it with an automated stage with feedback control of position(ASI MS-2000, nominal 50nm resolution). To test the stability of this stage, we focused a laser beam through a glass chamber bottom containing water, and observed time-varying change of focus. The results are shown in Fig.2.4(a), no focus drift beyond the tracked position of 10nm was detected after one hour.

In later experiments, particles' lateral positions were determined by image analysis based on well-established particle tracking algorithms [77]. To characterize their precision for our setup, first, the condenser of microscope was adjusted so that a colloidal particle appeared as a bright central spot with symmetrical intensity

distribution in the field of view. Then, positions of a stuck silica particle with 3.2μm in diameter in a solution were tracked in a short period. The histogram of positions is shown in Fig.2.4(b), which gives a precision of 10nm in locating the center of particle. Note that this precision should be also related with vibration noise.

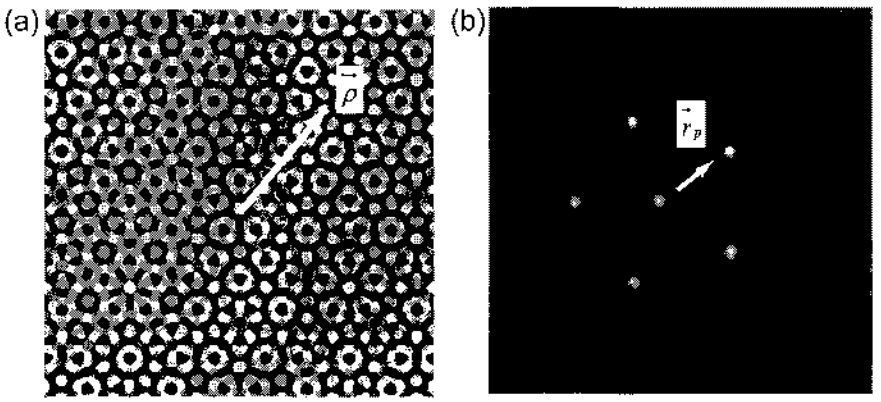

FIGURE 2.5: (a)Phase mask incorporated in SLM to generate multiple point traps with a distribution of pentagon shape. (b)The consequent trapped 3.2μm diameter silica particles on focal plane. The particle trapped in center is due to the undiffracted zero-order intensity. Coordinates $\vec{\rho}$ and $\vec{r}_p$ are defined in Eq(2.9).

An example of holographic optical trapping in our system is shown in Fig.2.5. A phase mask of five point traps, distributed evenly around a circle with a radius of 20μm, was incorporated in SLM, which is illuminated by laser with output power of 60mW. Correspondingly, five 3.2μm diameter silica particles were trapped in the focal plane. The intensity of focused spot from zero-order of diffraction is still strong enough to trap an additional particle in the center. In principle, the zeroth order spot can be blocked. In practice, we conduct our colloidal experiments with line traps generated away from this center trap.

2.5 Motions of Trapped Single Particles

To characterize trapping ability of our system, we measured the stiffness coefficients of a single trap. For a trapped particle, its Brownian motion caused by collision with surrounding liquid molecules is confined. It can only fluctuate around the trapping position in three dimension. Consider positions along the x-axis, the force exerted on particle can be described by a harmonic oscillator.

$$F = -\alpha(x - x_0) \tag{2.12}$$

where x is the displacement of particle away from the equilibrium position of x_0, and k is the stiffness coefficient of trap which cannot be directly measured. However, the probability distribution of the trapped particle's positions can be described by a Boltzmann relationship

$$P(x) \propto \exp(-\frac{U(x)}{k_B T}) = \exp(-\frac{\frac{1}{2}\alpha(x - x_0)^2}{k_B T}) \tag{2.13}$$

where k_B is the Boltzmann constant and T is the temperature. Suppose that $P(x)$ obtained from experiment can be fitted with a standard gaussian function with a width of σ, $\frac{1}{\sqrt{2\pi\sigma^2}}\exp(-\frac{(x - x_0)^2}{2\sigma^2})$. Therefore, α can be determined from σ with

$$\alpha = \frac{k_B T}{\sigma^2} \tag{2.14}$$

In experiments, a single point trap was formed by directly focusing the laser beam on the focal plane of objective lens. Silica particles with diameters of 0.9μm and 3.2μm were put in a 8-well chambers with No.1.0 borosilicate coverglass

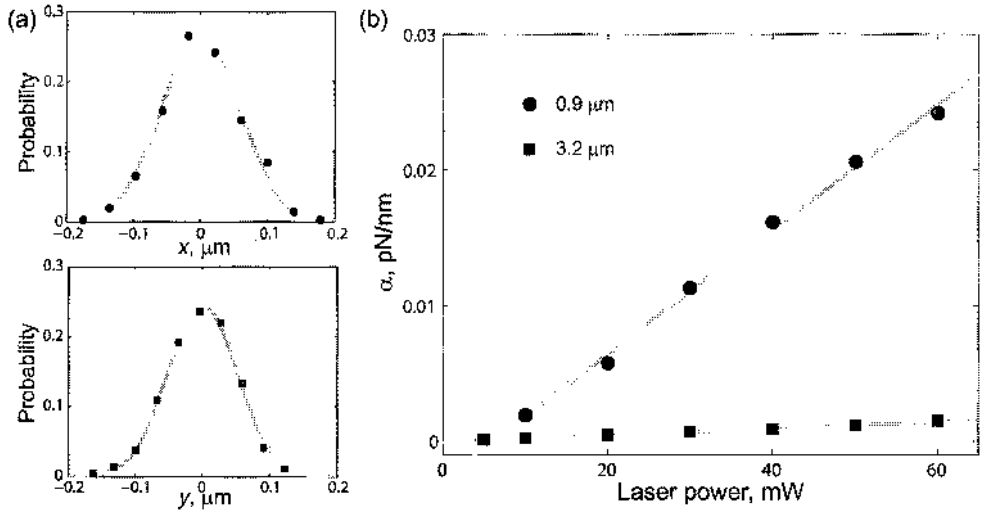

FIGURE 2.6: (a) Displacement distributions of a trapped 3.2μm diameter silica particle in x and y direction of focal plane,respectively (points), both of which can be fitted by Eq(2.13) (solid gray curves). (b) Plots of stiffness coefficent α versus laser power for 0.9μm and 3.2μm diameter silica particles, respectively (points). Solid lines are linear fits.

bottoms (Lab-Tek, Nalge Nunc International) surrounded by deionized (DI) water (Millipore,18.2MΩ·cm). In each measurement, motions of trapped single particles were captured by the camera with a rate of 10 frames per second for 5 minutes. For 3.2μm diameter silica particles under a laser power of 60mW, its displacement distributions in x and y directions are shown in Fig.2.6(a). Both $P(x)$ and $P(y)$ can be fitted by Gaussian forms with slightly different widths, which implies a dependence of trapping stiffness on the direction of focused spot on focal plane. Such dependence is related with the transverse intensity distribution of laser beam. Performing such measurements for different laser powers, We found that there is a linear relationship between laser power and stiffness coefficient (Fig.2.6(b)) for

particles of each size as expected. However, the stiffness coefficient depends on both laser power and particle size. Trapped with the same laser power, the smaller particle will be trapped more tightly. Note that each stiffness coefficient measured in Fig.2.6(b) is the result of averaging corresponding α_x and α_y. The smaller the particle is, the bigger the stiffness coefficient is on the trapped particle under the same applied laser power. However, the minimum laser power to provide stable trapping will be higher as the size of particle decreases. For example, as shown in Fig.2.6(b), 3.2μm diameter silica particles can be stably trapped with a laser power as low as 5mW, which is not high enough to stably trap 0.9μm diameter silica particle. In order to stably trap a smaller particle, higher laser powers are needed to suppress collision forces by fluid molecules due to the low mass and low friction coefficient γ ($\gamma \propto a$, a is the radius of particle) of particle itself. Once particles are trapped, from Eq (2.4) and (2.5), $F_g \propto a$ and $F_s \propto a^6$. Therefore, 3.2μm diameter silica particles will experience much larger scattering force than 0.9 μm diameter silica particles. Correspondingly, the measured stiffness coefficients of 0.9 diameter silica particles are larger than that of 3.2 diameter silica particles under the same applied laser power(Fig.2.6(b)).

2.6 Summary

In this chapter, we first reviewed the history, properties and applications of optical trapping in Sec.2.1. Then, in Sec.2.2, we analyzed the forces exerted on particles near

a focused light field in both Raleigh and Mie field, and gave the conditions for a stable optical trapping. Based on the review of techniques applied in optical tweezers in Sec.2.3, we gave an introduction of HOTs techniques, which focused on the mechanism of phase modulation in SLM, and the method to dynamic control optical trap array system. In Sec.2.4, we gave a description of the established HOTs system in our lab and analyzed several factors we considered in system design. The usability of our system was demonstrated by an example of holographic optical trapping. Finally, the trapping ability of our system were characterized by stiffness coefficient measurements in Sec.2.5

CHAPTER III

COLLOIDAL PAIR INTERACTION MEASUREMENTS

In this chapter, we will describe experimental methods to quantify colloidal pair interactions, specifically line trap generation. We will first give a brief introduction of methods that have been used in the past to characterize colloidal interactions, in which the motivation to make line traps will be presented. Then, following descriptions of some unsuccessful attempts we have tried, we will discuss the design of tunable line traps based on HOTs, which can make trapped particles experience nearly free, one-dimensional Brownian motion. Finally, after introducing procedures to determine true pair interaction potentials from particles' trajectories, we will describe the test of our line traps involving the measurements of the pair potentials of bare silica particles.

3.1 Introduction

As pointed out in Chapter I, interactions between colloidal particles play important roles in colloidal stability, phase behavior and rheology. The experimental techniques used to quantify colloidal interactions depend on the size of particle.

For particles less than about $1\mu m$ in diameter, it is difficult to isolate single particles due to vigorous Brownian motion and low optical scattering cross-sections.

Such colloidal systems can be studied by dynamic light scattering technique (DLS) [78, 79, 80], which is based on the Tyndall effect introduced in Chapter I. The measured intensity and angular dependence of scattered light can be used to calculate the particles' translational diffusion coefficient, which can be modeled as a function of particle density with several fitting parameters related with colloidal interactions. DLS is ideal for the study of particles with sizes of several tens nanometers, such as proteins [81]. As particle size increases to microns, the occurrence of multiple scattering hinders the investigation of colloidal interactions with DLS, which make other techniques take its place.

With Atomic Force Microscopy (AFM) [82, 83], two colloidal particles immersed in a solution can be finely controlled to move towards each other. One particle is glued on the tip of cantilever as a probe, the other is mounted on a substrate attached with piezoelectric crystal, which can control the separation between particles in a range of 100nm with a precision of 1nm. As particles approach, the force between particles can be deduced from deflections of cantilever with a calibrated spring constant. AFM can provide a measurement of force in a range of 10^{-10}~10^{-8}N with a high resolution. However, AFM is incapable of measuring long-range interactions due to the limited vertical moving range of piezoelectric crystal. Moreover, the existence of tip and substrate will interfere the measurement, because interactions among the tip, substrate and particles will also contribute to the final measured results, which will affect the determination of true particle interactions.

In colloidal suspensions, colloidal particles undergo Brownian motion and separations between them continuously fluctuate. In order to characterize such dynamic colloidal interactions, new techniques need to be developed to achieve non-intrusive measurements. For a particle larger than about 1μm, its fluctuating position above transparent planar surface can be measured via total internal reflection microscopy (TIRM) [84, 85, 86]. When it is illuminated by evanescent waves, the scattering intensity due to the particle will decay exponentially with the distance from the surface. The histogram of measured scattering intensity can be related to the probability distribution of particle's height, which can be used to characterize the energy profile of particle-surface interaction via the Boltzmann relationship. Similarly, in reflection interference contrast microscopy (RICM), when a particle is illuminated by a conventional light source, its height can be analyzed from the interference pattern produced by lights reflected from the medium-particle and medium-substrate interfaces. We will investigate RICM technique in detail in the next chapter. TIRM (RICM) can detect weaker forces (10^{-12}N) than AFM due to the nature of the thermodynamic energy unit k_BT. In such particle-surface systems, interaction measurements depend on the determination of particle heights.

Even though TIRM (RICM) can only be used to characterize particle-substrate interaction, the underlying physics~Boltzmann relationship illuminates a way to measure particle-particle interactions. To characterize colloidal interactions, it is very important to precisely locate the position of each particle. Digital video microscopy

[77] can allow direct observation on a colloidal suspension. Illuminated by the condenser of microscope, each particle appears as a bright circular spot surrounding with dark rings in the field of view. Fitting the intensity of particle's image with a Guassian, the well-established algorithm allows the determination of the center of each particle with a precision of 20nm. With the tracked in-plane position of each particle in equilibrium, pair correlation function can be contructed and used to calculate the mean force of interacion via Boltzmann relationship , which can be reduced to pair potential if the suspension is very dilute.

However, the pair potential calculated from pair correlation function of dilute suspension still depends on the distribution of particles. To characterize pair interaction energy only related with two particles, two colloidal particles need to be isolated to completely eliminate many-body effect. Due to their ability to manipulate colloidal particles, optical tweezers have been employed to measure colloidal pair interactions, first done by Crocker et.al. [87] using a 'blinking' optical trap setup. The separation between two particles was initially set by dual optical tweezers. Then, particles can be allowed to drift under interparticle interaction for a short period by switching off the optical traps('blinking'), after which the traps are again turned on. By Repeating this process for a range of separations, the energy profile of pair interactions can be obtained. An advantage of the 'blinking' trap setup is that measurements are only executed when optical traps are turned off so that no optically-induced interactions are possible. However, despite some modifications [88],

measurements of pair interaction using this method still require intensively sampling different separations, which will cost lots of time to acquire and analyze data.

To get a more efficient way to characterize colloidal pair interactions, let us reexamine the Boltzmann relationship. Considering two particles, the pair potential $U(r)$ relates with probability distribution of separation between two particles $P(r)$ by

$$P(r) \propto \exp(-\frac{U(r)}{k_B T}) \tag{3.1}$$

which can be used to determine pair interaction energy through position sampling of each particle in experiment. Because the range of interaction usually cannot exceed the length of several particle's diameters, only separations in a short range contribute to the interaction energy characterization. Therefore, pair potential can be determined more efficiently if particles are confined in a narrow space, which allows an intensive sampling of short separations between them. In our experiment, such confinements are achieved by line optical tweezers, in which colloidal particles can only diffuse in one dimension.

3.2 Tunable Line Trap Generation

In conventional optical tweezers, a beam is focused with intensity symmetrically distributed around center, which leads to similar trapping abilities along all directions on focal plane. In comparison, for a line trap, focused beam spot extends in one direction to form a line-shaped intensity distribution, which simultaneously allows

particle to move along this line and to be perpendicularly trapped. In the past, line traps were usually generated by rapidly scanning a point trap via an AOD [89, 90]. Line traps formed by non-scanned light were first reported by Biancaniello et.al. [91, 92]. In their experiments, short-range interactions between two DNA-grafted colloidal particles were measured in a line trap, which is constructed by redistributing laser intensity with a cylindrical mirror.

Returning to our HOTs setup, to measure pair potentials of colloidal particles, we need to use the SLM to generate a line trap which has a flat potential so that $P(r)$ and $U(r)$ are simply related by Eq(3.1). An example of such generations is given by Roichman et.al. [93], who made a line trap by means of the Fourier relationship between the optical intensity in the focal plane and the aperture function in the conjugate (SLM) plane. When light illuminates a rectangular aperture, the intensity of Fraunhofer diffraction pattern is given by a sinc function via Fourier transform. Contrarily, if a phase mask encoded with a sinc function in one dimension is input in SLM, it is possible to form a line-shaped intensity distribution on the focal plane. However, this method requires SLM to be modulated by amplitude as well as phase due to the sinc-function aperture, which will make most power of the incident light not contribute to the line trap generation. The efficiency of this approach is extremely low [93]. Therefore, we need to develop other SLM-based methods in order to create useful line traps.

A SLM, as a programmable diffractive optical element (DOE), can be also used

to redistribute intensity to form desired patterns on image plane. As we know, a line-shaped pattern can be easily constructed by incorporating a cylindrical mirror phase mask in SLM and reshaping a flat (planar) incident laser wavefront. The tranverse profile of laser used in our HOTs setup is not flat. However, phase functions that map a Gaussian beam profile onto a flat focal plane intensity function are known [94, 95] and can be easily applied. Suppose a Gaussian transverse intensity profile of incident beam,

$$I_0(\vec{\rho}) = I \exp(-\frac{\vec{\rho}^2}{2\sigma_0^2}) \tag{3.2}$$

where $\vec{\rho} = (\mu,\nu)$ denotes the coordinate in SLM plane. σ_0 represents the width of gaussian profile, which can be determined by image analysis in experiment. A flat line trap parallel to x-axis with a length of l can be formed by incorporating a phase mask in SLM, which corresponds to the phase distribution $\phi(\vec{\rho})$ [94]

$$\phi(\vec{\rho}) = \frac{k\vec{\rho}^2}{2f_0} + \frac{kl\sigma_0}{\sqrt{2}f_0 erf(\frac{A}{\sigma_0\sqrt{2}})}\{\frac{\mu}{\sigma_0\sqrt{2}} erf(\frac{\mu}{\sigma_0\sqrt{2}}) - \frac{1}{\sqrt{\pi}}[1 - \exp(-\frac{\mu^2}{2\sigma_0^2})]\} \tag{3.3}$$

where k is the wave vector of incident beam, f_0 is the focal length of objective lens, and SLM is illuminated with a rectangular area of A×B.

In experiments, the transverse intensity profile of our laser is almost flat so that a relatively large value was assigned to σ_0 in calculation. A phase mask (Fig.3.1(a)) encoded with above phase distribution was displayed in SLM with an area of 600×600 pixels ($4.8\times4.8\text{mm}^2$), which is illuminated by a laser with output of 60mW. The resulting line trap (Fig.3.1(b)inset) with a length of 25μm was focused through a glass-bottom chamber, which contained a dilute colloidal suspension. The captured

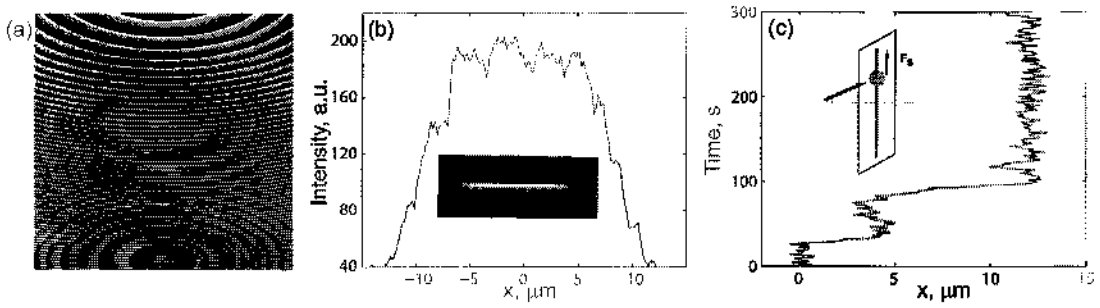

FIGURE 3.1: (a) Phase mask for a 25μm line trap with flat intensity. (b) The consequent intensity distribution of focused line trap in focal plane, which shows a flat top. Inset: the image of line trap. (c) The trajectory of a trapped 3.2μm diameter silica particle, which was initially put in the center of line trap. Inset: scattering force exerted on trapped particle to push it to the end of the line. The red line with arrow represents incident beam rays on particle.

image of line trap was analyzed by imaging processing toolbox of MATLAB software with data plotted in Fig.3.1(b), which shows a uniform intensity distribution along the line. Then, a 3.2μm-in-diameter silica particle was put on the center of line trap, and the motion of trapped particle was monitored for 5 minutes, which yields a trajectory of particle along line trap shown in Fig3.1(c). Surprisingly, instead of free Brownian motion, the particle heads irreveribly to an end of line. This is further quantified in [55], which includes measurements of the outward-directed force. A line trap with uniform intensity distribution can not provide a flat trapping potential for particles to diffuse freely along it, which makes it impossible to simply measure pair interaction energy of colloidal particles via the Boltzmann relationship.

To explain this observed phenomenon, let us re-examine the physical principle behind optical trapping. If a point trap can provide gradient force greater than

scattering force, a particle with refractive index greater than that of surrounding solution can be trapped. For a particle in a line trap, the situation is shown in Fig.3.1(c)inset. Once a particle departs away from center due to thermal collision with solution molecules, there is always a component of the scattering force exerted on it that is along the line, which is proportional to its displacement away from center. On the contrary, due to the uniform intensity distribution of the line trap($\bigtriangledown I = 0$), particle will not experience any gradient forces along the line. This situation will make particle be pushed toward the end of line, where the regained gradient force due to discontinuity of intensity can balance the scattering force to allow particle to be trapped there. Therefore, we need to tune the intensity of line trap to balance scattering force.

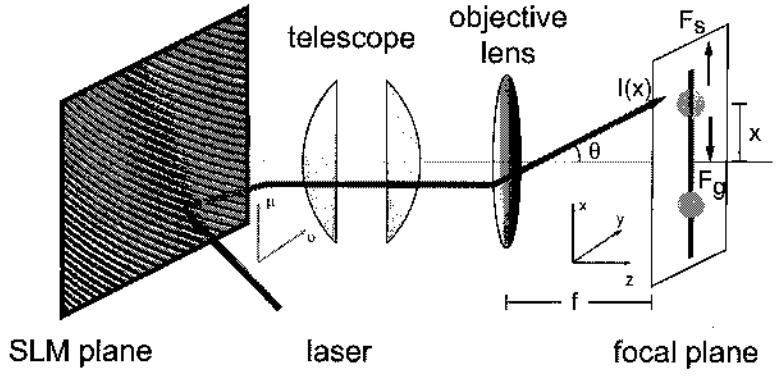

FIGURE 3.2: A schematic diagram of line trap generation and resulting forces exerted on trapped particles (solid light green circle) with intensity $I(x)$. In SLM plane, the grey pattern is the phase mask of line trap. See text for details.

Consider a line trap along x-axis and centered in origin as shown in Fig.3.2, the

scattering force F_s exerted on particle at position x is proportional to x and I:

$$F_s(x) \propto I(x)\theta \propto xI(x) \tag{3.4}$$

which is along x direction. To balance it, a gradient force F_g needs to be added in the opposite direction by tuning intensity $I(x)$

$$F_g(x) \propto \frac{dI(x)}{dx} \tag{3.5}$$

Free Brownian motion of a particle in the line trap requires $F_g = F_s$, which yields an equation

$$xI(x) - C\frac{dI(x)}{dx} = 0 \tag{3.6}$$

where C is a position-independent constant related to some optical factors such as particle size, index of refraction, wavelength, etc. The equation can be satisfied by an intensity profile with a Gaussian distribution

$$I(x) = A\exp(-\frac{x^2}{2\sigma^2}) \tag{3.7}$$

where A is a normalization factor. The balance of forces depends on σ. If $\sigma^2 > C$, scattering force will dominate the motion of particle to push it towards the end of line trap. On the contrary, particle may be confined in a small area near line trap center by an overbalanced gradient force. Eq(3.7) gives us the desired $I(x)$. We are left with the question of how to realize this using the phase modulation of the SLM, as in [55]. Let us start from the diffraction of a single point trap. The coordinates of the SLM plane and focal plane are shown in Fig.3.2. A diffracted point trap can be

generated by modulating the wavefront of incident beam with a prism phase mask. If it focuses on $(x, 0)$ in the focal plane, the corresponding phase distribution on SLM can be expressed by

$$\varphi(\mu) = \frac{2\pi}{\lambda}\mu\theta \tag{3.8}$$

where λ is the light wavelength, $\theta = \frac{x}{f}$ and f is the focal length of objective lens. Beam rays reflected from all the illuminated pixels are transmitted to $(x, 0)$ for the formation of single point trap, which gives rise to an independent relationship between the position of trap and the number of pixels used to generated it. However, this relation is changed when the focused spot is extended in one direction to form a line shape. If the intensity distribution of a line trap is uniform, each unit of the line dx should be illuminated by beam rays reflected from an equal small amount of pixels du on SLM so that $\frac{du}{d\theta} = \frac{du}{dx}$ =constant. Therefore, back to Eq(3.8), $\varphi(\mu) \sim \mu^2$. For a uniform line trap between $x = \pm\frac{l}{2}$ along x-axis, the phase distribution on SLM can be expressed by

$$\varphi(\mu) = \frac{\pi l \mu^2}{2\lambda f \mu_{max}} \tag{3.9}$$

the range of pixels along μ-axis used for line trap generation is between $\pm\mu_{max}$. This is a cylindrical mirror phase which is similar as the first part of Eq(3.3). Analogously, for a line trap with a Gaussian intensity distribution $I(x)$ in Eq(3.7), the number of pixels du on SLM used to generate a unit dx in line trap should vary with position x, in which, more pixels should be distributed to position with a higher intensity based on $\frac{du}{dx} = I(x)$. According to Eq(3.8), we have $\varphi' = \frac{d\varphi}{du} = \frac{2\pi}{\lambda f}x$, which yields

$\frac{dx}{d\varphi'}$ =constant. Therefore, from Eq(3.7), we have

$$\frac{du}{d\varphi'} \sim \exp[-(\frac{\lambda f}{2\pi})^2 \frac{\varphi'^2}{2\sigma^2}] \tag{3.10}$$

which yields

$$\mu \sim \frac{\pi\sqrt{2\pi}\sigma}{\lambda f} erf(\frac{\lambda f \varphi'}{2\pi\sqrt{2}\sigma}) \tag{3.11}$$

where erf is the error function. A line trap with a Gaussian distribution along x axis with endpoints at $x = \pm\frac{l}{2}$ can be obtained by integration

$$\varphi'(\mu) = \frac{2\sqrt{2}\pi\sigma}{\lambda f} erfinv[\frac{\mu}{\mu_{max}} erf(\frac{l}{2\sqrt{2}\sigma})] \tag{3.12}$$

where $erfinv$ is defined as the inverse of erf. As $\frac{l}{\sigma} \to 0$, it can be reduced to the cylindrical mirror phase function in Eq(3.9).

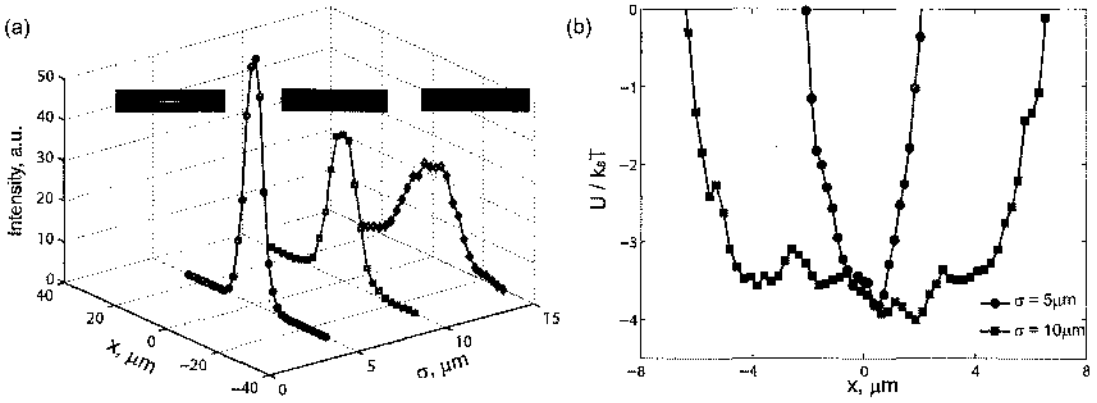

FIGURE 3.3: (a) Measured intensity profiles of Guassian line traps. Inset: images of line traps with σ of 5μm, 10μm and 15μm repectively. (b) Trapping potential profiles of Gaussian line traps with σ of 5μm and10μm.

Because it is hard to calculate the constant C in Eq(3.6), the appropriate value of σ, which can provide a flat trapping potential to particles, cannot be theoretically

determined. In experiments, several values of σ have been tried to generate line traps with tunable Gaussian intensity distributions, each of which was about 60μm in length powered by laser power of 20mW. Motions of trapped single particle with 3.2μm in diameter were captured with 16 frames per second in 50 minutes for each σ. For example, when a line trap was generated with $\sigma = 5\mu$m, Fig.3.3(a)inset shows its Gaussian intensity distribution with a narrow width. Correspondingly, the motion of the particle on it was confined in a small range near its center, which is about 4μm as shown in Fig.3.3(b). The optimal value we found for σ is about 10μm, in which even though the resulting intensity distribution of line trap is still a Gaussian with a wider width instead of uniformity, the potential profile shows an almost flat potential well with a length of 9μm, which suggests the balance between F_s and F_g. For σ values greater than 10μm, the position of the deepest trapping potential began to move to either end of the line. Finally when σ is fairly large (greater than 17μm), the behaviour of trapped particle will be similar as that in a line trap with uniform intensity distribution, in which particle will quickly drift to one end and stay there. The actual one-dimensional space, which can be sampled by the particle, is much smaller than the length of line trap set in phase mask calculation. Even in the condition of optimal σ value, the range of free diffusion is only about one fifth of the length of line trap for a silica particle with 3.2μm in diameter. However, this distance, which is about three times of particle's diameter, is still long enough to measure pair potential over a significant interaction range. The actual length

for free diffusion depends on particle size and laser power. Smaller particle with larger optimal σ values can provide a broader free diffusion range. We have tried particles with 2μm in diameter, which can give a maximum free distance of 11μm with the same experimental conditions. However, with our weak laser power, such small particles are easy to escape from line trap. Therefore, for subsequent pair interaction measurements, we still use 3.2μm-in-diameter silica particles.

3.3 Pair Potential Measurements of Bare Silica Particles

So far, we have shown the generation of tunable line traps using a SLM, which can provide a flat trapping potential for particles in one dimension by balancing gradient and scattering forces. Next, we want to demonstrate its ability to measure pair interaction energies of colloidal particles.

Colloidal Interactions in Electrolyte Solutions

For a silica particle, when it is immersed in an electrolyte solution, its surface will be charged with SiO^- due to the deprotonation of silanol group. Some counterions in solutions such as Na^+, H^+ will be attracted to tightly bind on the surface of particle, which yields an immobile counterion layer to partially balance the surface charge. Ions outside this layer form a diffuse layer, in which ions are under thermal motion with a distribution determined by the electric field around particle. When two silica particles approach each other, the repulsive Coulomb interaction between them is screened by the diffuse layer. If the number of surface charge on each particle remains constant,

it can be described by [96]

$$U_e(r) = \frac{Z^2 e^2}{\epsilon} \frac{e^{\kappa a}}{1+\kappa a} \frac{e^{-\kappa r}}{r} \tag{3.13}$$

where r is the center-to-center separation between particles, Z is the number of effective surface charge, e is the elementary charge, ϵ is the dielectric constant of solution, a is the radius of particles and κ is the inverse Debye length, which is defined by

$$\kappa^2 = \frac{4\pi e^2}{\epsilon k_B T} \sum_j z_j^2 \rho_j \tag{3.14}$$

where ρ_j is the number density of j-th ions with valency of z_j in electrolyte solution. For a solution with 1:1 electrolyte, such as NaCl, κ^{-1} can be expressed by [96]

$$\kappa^{-1} = \frac{0.304}{\sqrt{[NaCl]}} nm \tag{3.15}$$

where [NaCl] denotes the molar concentration of salt in M in the solution. The range of Coulomb interaction is characterized by the Debye length, which only depends on the type and concenteration of counterions in the solution.

Another kind of interaction between particles is Van Der Waals attraction, which comes from fluctuating electric dipoles. Motion of electrons in an atom can provide transient polarity. Even though such temporary change can disappear as quickly as it appears, the interaction between fluctuating electric dipoles can make atoms attract each other with a decay of $1/r^6$, where r is the separation between two atoms. Such attraction between two macroscopic particles should be derived from the summation of those between constituent atoms. For two particles with radius a, Van Der Waals

attraction between them can be expressed by [96]

$$U_v(r) = -\frac{A}{6}[\frac{2a^2}{r^2 - 4a^2} + \frac{2a^2}{r^2} + \ln(1 - \frac{4a^2}{r^2})] \tag{3.16}$$

where r is the center-to-center separation between particles, A is the effective Hamaker constant which depends on dispersion medium the material is immersed in. For silica in water, $A_{silica} = 4.8 \times 10^{-21} J$ [97].

According to DLVO theory, the total potential energy between colloidal particles should be the suppoposition of Coulomb repulsive potential $U_e(r)$ and Van Der Waals attractive potential $U_v(r)$

$$U(r) = U_e(r) + U_v(r) \tag{3.17}$$

By roughly observation of two silica particle on the line trap, we found that the minimum center-to-center separation sampled is about 4μm. Two particles always separate from each other without aggregation, which implies the dominance of Colomb repulsion over Van Der Waals attraction. In addtion, the estimated Van Der Waals attraction at such separations is about $0.04k_B$T, which is small enough to be neglected. Therefore, we would expect the measured pair interaction energies of bare silica particles will be solely the screened Colomb repulsive potental.

Nonuniform Line Trap Potential

From Fig.3.3 we can see, even though the one-dimensional space for free diffusion provided by a line trap with a Gaussian intensity distribution is long enough to sample particle's separation in the full interaction range, the trapping potential is

not quite flat, which usually happens due to the imperfection of optical alignment. In addition, in order to reduce sampling time, we wish to intentionally introduce a net gradient force to hold particles in short separations around the center of the line trap. Therefore, the measured separation distribution is related with not only the true pair potential between particles but also the uneven trapping potential, which needs to be accounted for. Considering two interacting particles in a line trap with length l available to sample between $x = \pm\frac{l}{2}$, $P_1(x_1)$ and $P_2(x_2)$ denote probabilities of particle 1(2) as position $x_1(x_2)$ respectively. Due to colloidal interactions, the position of one particle affects that of the other. The observed probability distribution of separation $P_{obs}(r)$ along a line trap can be expressed by

$$P_{obs}(r) = A\int_{l/2}^{l/2-r} P_1(x_1)P_2(x_1 \mid x_1 + r)dx_1 \tag{3.18}$$

where A is a normalization constant, $P_2(x_1 \mid x_1 + r)$ denotes the probability of finding particle 2 at $x_2 = x_1 + r$ while particle 1 is at x_1. For particle 2 at $x = x_2$, it will feel interactions from particle 1 at $x = x_1$ and the trapping potential at $x = x_2$. The total enerey is

$$U_2(x_2) = U_{pair}(r) + U_{ext}(x_2) \tag{3.19}$$

The corresponding probability distribution can be denoted by

$$P_2(x_1 \mid x_1 + r) = \exp(-\frac{U_2(x_2)}{k_BT}) = \exp(-\frac{U_{pair}(r)}{k_BT})\exp(-\frac{U_{ext}(x_2)}{k_BT}) = P_{pair}(r)P_2(x_2) \tag{3.20}$$

Returning to Eq(3.18), and considering that the trapping potential experienced by particle 2 at x_2 equals to that by particle 1 at $x_1 + r$, the observed probability

distribution of separation $P_{obs}(r)$ is

$$P_{obs}(r) = A\int_{-l/2}^{l/2-r} P_1(x_1)P_{pair}(r)P_2(x_2)dx_1 = AP_{pair}(r)\int_{-l/2}^{l/2-r} P_1(x_1)P_1(x_1+r)dx_1 \tag{3.21}$$

Finally, with $P_1(x_1)$ replaced by $P(x)$, the true pair distribution function, $P_{pair}(r)$, is related to the observed pair distribution function, $P_{obs}(r)$ by

$$P_{pair}(r) = \frac{P_{obs}(r)}{\int_{-l/2}^{l/2-r} P(x)P(x+r)dx} \tag{3.22}$$

To measure pair potential energy in experment, first, positions of single particle along a line trap need to be sampled to obtain $P(x)$, which is related to the trapping potential profile. Then, $P_{obs}(r)$ can be constructed by pulling another particle into line trap and sampling separations between particles. Finally, the true pair potential can be deduced from Eq(3.22) via the Boltzmann relationship. To guarantee that a particle samples all available space in a line trap, positions of particle need to be measured over a time much greater than $\frac{l^2}{2D}$, where D is the diffusion coefficient of particle. For a 3.2μm diameter particle in water, its diffusion coefficient is about 0.2μm^2/s. Considering an available distance of 10μm in a line trap, we usually measure positions of particles in 50$\sim$60 minutes in experiments.

Optical Binding

The optical intensity of line trap can not only provide an uneven trapping potential to complicate the determination of true pair interaction energy, but can also in principle induce attractions between particles. Two trapped particle will

behave as two dipole ocillators, which are powered by the polarized optical field. The resulting Lorentz force due to the interaction between induced current in the two synchronized oscillators will make particles attract each other, which is more obvious when particles are aligned in the direction perpendicular to the polarization of laser beam. This so called optical binding effect was first investigated by Burns [98]. Such effect can add additional interactions between particles, which made the measured pair potential different from the true pair interaction energy of particles. In experiment, we made a line trap along the same direction as the polarization of laser beam to minimize orientation-dependent optical binding effect. Considering the dependence of such attractions on laser power, we will measure pair potential of the same two bare silica particles in line traps illuminated with different laser powers.

Errors in Particle Localization

When illuminated by the light from microscope condenser, a particle appears as a bright central spot surrounding with series of dark rings, which can span a distance comparable to the radius of particle. By fitting the intensity distribution of central spot with a Guassian, particle can be located at the position with the maximum intensity. However, when two identical particles apporach each other, dark rings of one particle maybe overlap with the bright spot of the other. The resulting changes in intensity distribution will affect the determination of particle's position, and hence the separation between particles. In order to calibrate the measured separation, we adopt the method reported by Baumgartl et.al. [99]. A stuck particle sitting on the

bottom of chamber serves as a reference at position (x_0,y_0), which is measured when it is isolated from other particles far enough so that no image ovevlap happens. Then, we manipulate another mobile particle by optical tweezers to approach to the stuck one step by step. During this process, the measured separation between two particles can be expressed by

$$r(t) = \sqrt{[x(t) - x_0'(t)]^2 + [y(t) - y_0'(t)]^2} \tag{3.23}$$

where $(x(t), y(t))$ denotes the measured positions of mobile particle, ($x_0^{'}(t)$,$y_0^{'}(t)$)are the measured positions of the stuck particle, which are different from (x_0,y_0) due to image overlap. The error in separation measurement can be characteraized by

$$\Delta r(t) = r(t) - \sqrt{[x(t) - x_0]^2 + [y(t) - y_0]^2} \tag{3.24}$$

With the time-averaged $r(t)$ and $\Delta r(t)$ denoted as r and Δr,respectively, and the consideration of symmetrical image distortion on both particles, the true separation can be given by

$$r_t = r - 2\Delta r \tag{3.25}$$

In experiments, the stuck particle was made by coating bare silica particle with excess amount of positively charged lipids, The resulting posively charged particle can be attracted to sit on the negatively charged glass bottom of chamber due to Van Der Waals attraction. The lipid-coated layer is so thin (5nm) that the change of particle size can be neglected. Each moving step of the optical trap towards the

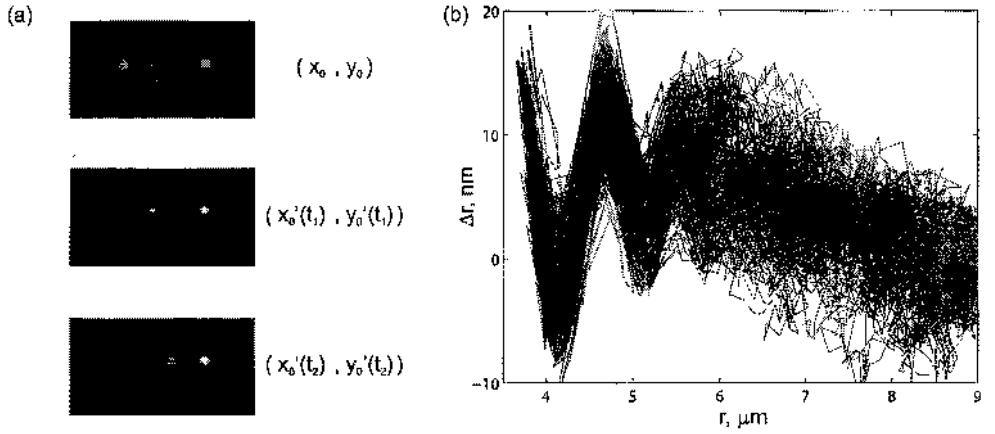

FIGURE 3.4: (a) An experimental schematic of determining the error in separation measurements. Top: two particles were separate far enough to prevent their images from overlapping with each other. (x_0,y_0) denotes the true position of the stuck particle. Middle and bottom: the trapped particle was moved towards to the stuck particle step by step. (b) The plot of experimentally determined Δr versus measured separation between particles $r(t)$ in each step during the approach of two particles. The solid line is the binned data.

stuck particle needs to be carfully controlled so that sampled positions of mobile particle can cover the whole range of separations which needs to be calibrated. To save time, the mobile particle was trapped with a laser power of 10mW, which allows it to sample positions in a relative wide range in each step due to the weak strength of optical trap. For silica particles with 3.2μm in diameter, the relationship between the error in separation measurement Δr and the measured separation r is plotted in Fig 3.4(b), which shows a maximum error of 15nm. Due to its similar magnitude as

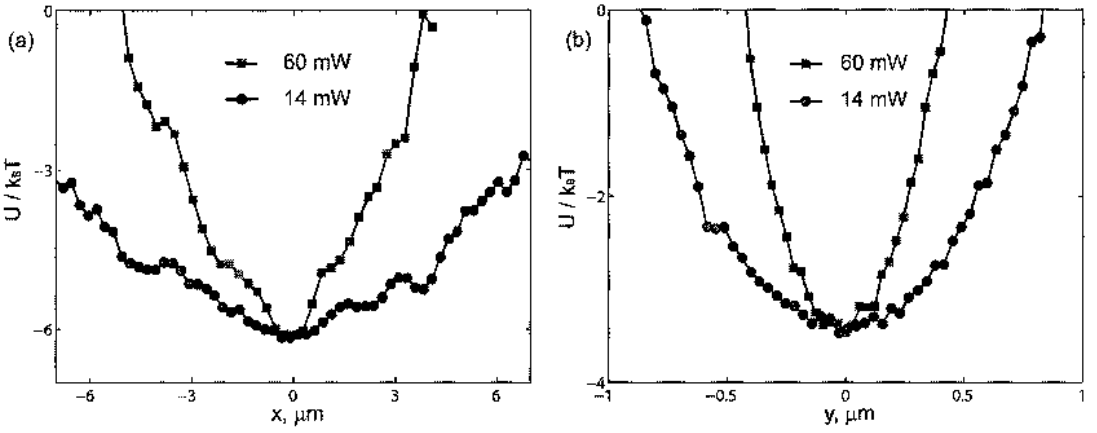

FIGURE 3.5: The measured trapping potential profiles of a 60μm line trap with laser output power of 60mW and 14mW in direction of (a) along the line (b) perpendicular to the line.

the precision of particle tracking algorithm, such errors in separation measurements due to image overlap can be neglected for a pair of 3.2μm diameter particles.

Pair Interaction Measurements of Bare Silica Particles

For pair interaction measurements, small amounts of dilute silica particle suspension were pipetted into deionized water, which is contained in an 8-well chamber with No.1.0 borosilicate coverglass bottoms (Lab-Tek, Nalge Nunc International). A line trap with a length of 60μm was focused near the chamber bottom where particles were sedimented by gravity. In order to hold particles near the center of line, $\sigma = 7.5\mu$m in Eq(3.7) was used in line trap generation. Two particles were randomly selected for pair potential measurement, and their motions around line trap were captured at 16 frames per second over a 10μm $\times$ 40μm area. First, only single particle was pulled in the line trap to characterize its potential

profiles under laser powers of 14mW and 60mW, respectively, which are shown in Fig.3.5. The data show the dependence of potential profile on laser power. Along the line, $U(x)$ under each laser power is not flat. The available length of line trap is about 10μm for laser power at 14mW, which is twice as long as that with laser power of 60mW. Perpendicular to the line in focal plane, particle behaves as that trapped in a point trap, their motions can be described by harmonic oscillators with different stiffness coefficients. Particles will be confined more tightly with a higher laser power. Pair potentials U as a function of center-to-center separation r are plotted in Fig.3.6. The measured pair potentials $U_{obs}(r)$, which are directly derived from $P_{obs}(r)$, show a repulsive interaction in the short range and an attractive interaction in the long range for both laser power. However, the calculated true pair potentials $U(r)$s by Eq(3.22) under both laser powers are similar and purely repulsive, which can be fitted to Eq(3.13) with $\kappa^{-1} = 126$nm and $Z = 2200$. The fitted Debye length corresponds to a salt concentration of 6μM, likely due to the dissolved carbon dioxide in water, which is consistent with other measurements of screening in water [100].

The similarity, especially in the short range, of pair potential curves measured under different laser powers demonstrates the lack of optical binding effect, which is not surprising due to the low laser power applied. In addition, we did not measure the separation of particles in the direction perpendicular to the focal plane. Considering the gravity of paricle, we neglect the contribution of its out-of-plane fluctuation to separation. The height measurement will be introduced in next

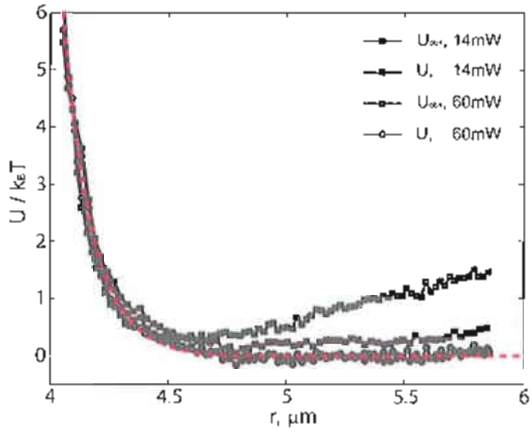

FIGURE 3.6: Pair interaction energies of 3.2 μm diameter silica particle. Both the naive pair potential U_{obs}, which is deduced from P_{obs}, and the true pair potential U are plotted as a function of center-to-center particle separation r. The pair potential measurements were performed under two different applied laser powers. The red dot line is a fit to Eq(3.13).

chapter. More importantly, Our data do not show like-charge attraction between bare silica particles.

3.4 Summary

In this chapter, based on the review of techniques to characterize colloidal interactions, we introduced the experimental schemes to quantify pair interaction energies of colloidal particles in suspensions. In Sec.3.2, line trap generation by SLM was described. We first showed that line trap with flat intensity distribution can not provide flat trapping potentials for particle due to the scattering force. After analyis of forces exerted on trapped particle, we found that a line trap with a Gaussian intensity distribution can make particle freely diffuse in one dimension. Then, the

method to calculate the corresponding phase mask was investigated, which was focused on the relationship between intensity modulation and pixel distribution in SLM. We finally test our method by observing the motion of a single particle. With a proper Gaussian width σ of line trap, a trapped particle can sample positions in one dimension, the range of which are enough to cover the full pair interaction range. In Sec.3.3, following with analysis of some factors related to the measurements of true colloidal pair potentials, the experimental scheme for $U(r)$ measurements was described. At the end, as a demonstration, we measured the pair potential of bare silica particles, which shows a purely repulsive interaction.

CHAPTER IV

REFLECTION CONTRAST INTERFERENCE MICROSCOPY

In this chapter, we will first introduce the fundamentals of conventional reflection contrast interference microscopy (RICM). Then, with a scheme to measure the particle-wall separation by contrast comparison, the separation between silica particles and a glass bottom of chamber in solutions are determined.

4.1 Introduction

In order to understand interactions between surfaces in aqueous environments, the distance between them needs to be accurately measured. For transparent surfaces, this task can be accomplished by total internal reflection microscopy (TIRM) or RICM as we have mentioned in a previous chapter, both of which can provide non-intrusive and high-precision separation measurements. Unlike TIRM, in which surfaces are illuminated by evanescent waves emitted from a laser, RICM can employ a conventional light source to illuminate objects near a transparent

substrate surface in solutions, Beam rays reflected from surfaces of an object and a substrate interfere to form a RICM image of the object, so that inter-surface distance, related to the intensity distribution of the interference pattern in the RICM image, can be extracted without florescence labeling or staining. RICM was first introduced by Curtis in 1964 [101], when he measured the separation between a glass substrate and a cell adhering to it under water. Restricted by the contrast of image, RICM in its early stage could only offer qualitative separation measurements. With some improvements in optics, RICM now has been widely applied in studies of cell adhesion [102, 103, 104], membrane fluctuation [105, 106] and film wetting [107, 108] with an optimal precision of 1nm in separation determination. Interactions between colloidal particles and surfaces [100, 109] is another area intensively investigated using RICM. Its suitability to provide quantitative measurement of particle-surface separation has been demonstrated in various applications. The tracked trajectories of colloidal ensembles can serve as probes to map the topography of underlying substrate surfaces [110, 111]. The height correlation function of particle can be used to characterize viscoelastic properties of surfaces in rheology [112, 113].

In our experiments, there are two motivations to measure the separation between particle and chamber wall. First, as we have pointed out in previous chapters, we need to quantify the fluctuating range of particle out of the focal plane, which is neglected when we determined separations between particles in pair potential measurements. Second, the reported confinement-induced like-charge attraction [16, 21] is related to

the particle-wall interaction, and the strength of attractive interaction depends on the particle-wall separation. Therefore, the measurement of particle-wall separation can provide a fundamental understanding of wall-mediated colloidal pair interactions. Due to its simplicity of setup, high resolution, and suitability for measurements as we mentioned above, RICM was employed to measure particle-wall separation in our experiments.

4.2 Fundamentals of RICM

As is shown in Fig.4.1(a), a particle with a radius of R, which is illuminated by a monochromatic light, is observed by inverted microscopy. A RICM image is formed by the superposition of light waves reflected from the top layer of the glass chamber I_1 and the bottom surface of the particle I_2. Considering a minimum distance h between the particle and the surface of glass substrate , the intensity of interference pattern in the radial direction x is given by [111]

$$I(x) = I_1 + I_2 + 2\sqrt{I_1 I_2}\gamma_{12}\cos\{\frac{4\pi n}{\lambda}[g(x) + h] + \delta\} \tag{4.1}$$

where $g(x) = R - \sqrt{R^2 - x^2}$ describes the contour of particle, n is the refractive index of surrounding medium, λ is the wavelength of illuminating light, δ denotes the phase shift of light reflected from medium-particle interface, and γ_{12} is related to the coherence degree. For example, a stuck silica particle with 3.2 μm in diameter on the glass chamber bottom was illuminated by light from a mercury arc lamp filtered by a 535$\pm$20nm band pass filter. Its RICM image is shown in Fig4.1(b), which consists

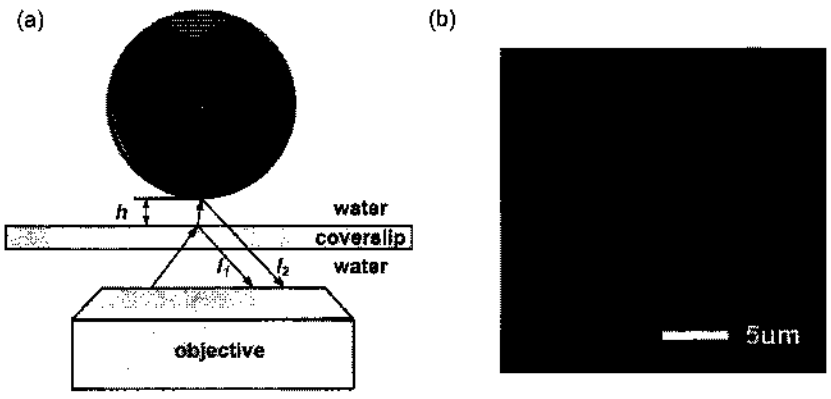

FIGURE 4.1:(a) A schematic diagram of interferogram formation. Lights I_1 and I_2, reflected from coverslip and particle, respectively, interfere at image plane to form RICM image.(b) RICM image of a stuck 3.2μm diameter silica particle. The edge on the upper left corner is the aperture diaphragm.

of a set of interference rings. $I(x)$ as a function of h can be calculated according to Eq(4.1), which yields a theoretically calculated library of RICM interferograms. The comparison of intensity distribution between a RICM image obtained in experiment and calculated RICM interferograms can give some information about corresponding height of particle above the bottom. However, absolute height still cannot be solely determined in this way, because I_1 and I_2 are unknown and $I(x)$ is a function of h modulo a factor of $\lambda/2n$. Without amplitude information, the intensity distribution of a RICM image can be fitted to Eq(4.1) with multiple values of h, which are at an interval of $\lambda/2n$ corresponding to the same interference fringes. However, absolute height determination is possible when it is certain that the particle is close to glass surface in a range between 0 and $\lambda/2n$. As is shown in Fig.4.2(a), the fitted RICM

intensity distribution of a stuck particle should give an absolute height around zero. For the green filter used in our experiments, $\Delta h = \frac{\lambda}{2n} \approx 250\text{nm}$.

In order to reconstruct absolute height, dual-wavelength RICM (DW-RICM) technique [111]has been developed to eliminate the ambiguity in height determination with single-wavelength RICM (SW-RICM). In which, RICM images are simultaneously recorded at two different wavelengthes with intensity distributions of $I(\lambda_a)$and $I(\lambda_b)$, respectively. The ratio of $\frac{I(\lambda_a)}{I(\lambda_b)}$ varies with h in a certain range so that h can be uniquely assigned with the additional introduced amplitude comparison. However, for DW-RICM, light from an arc lamp needs to be split to pass two band pass filters, the simultaneity of image capture from two wavelength channels complicates the optical setup and experimental control. In addition, ambiguity in height determination still exists, absolute height can be determined in a limit range, even though it is bigger than that using SW-RICM.

4.3 Experimental Motivation

In the above section, we have introduced the fundamentals of SW-RICM, which show its incapability of determining absolute height of particle above glass chamber bottom. With another periodicity introduced by additional wavelength in RICM intensity, the ambiguity in height determination can be eliminated by DW-RICM to some extent. However, considering the simplicity of SW-RICM system, we still want to figure out a way to use it to quantify the separation between silica particles and

charged glass bottom of chamber. γ_{12} in Eq(4.1) is almost ignored, which depends on the illumination numerical aperture (INA) of microscope

$$\gamma_{12} = \frac{\sin\theta}{\theta} e^{-i\theta} \tag{4.2}$$

with $INA = n\sin\alpha$ and $\theta = \frac{2\pi h}{\lambda}\sin^2(\frac{\alpha}{2})$, where α is the half angle of illumination cone. Due to the phase term in γ_{12}, periodicity of intensity is stretched. The same phase distribution of intensity recurs every elevation $\Delta h \approx 250$nm of particle with the green filter used in our experiments. Moreover, contrast of a RICM image is given by

$$D = I_{max} - I_{min} = 4\sqrt{I_1 I_2}\frac{\sin\theta}{\theta} \tag{4.3}$$

in which, if considering the unchanged separation between chamber bottom and objective lens, I_1 is almost constant. As particle elevates, the amount of reflected beam rays from particle, which are collected to contribute to intensity I_2, decreases due to the finite NA of the objective lens. The same situation happens with the γ_{12} related term in Eq(4.2) as well. Therefore, followed by the rise of particle, even though the same phase distribution of intensity in its RICM images occurs periodically, the contrast will decrease monotonically. An example is shown in Fig.4.2(b). RICM images of a particle in DI water were selected at three different moments which exhibit the same phase distribution of intensity. The drop of contrast between adjacent curves implies a rise of Δh in particle's height between corresponding moments. To make use of such contrast differences, first, the position of focal plane must be fixed during RICM image acquisition. Therefore, the field

diaphragm, which is located on the conjugate focal plane, is partially closed to provide a sharp edge for focusing (upper left corner in Fig.4.1(b)). Second, an objective lens with high NA is preferred, because it can provide a short depth of image field, which gives rise to a sensitive response of contrast to changes in height. The NA=1.2 60X water-immersion objective lens was also used in RICM image acquisition. The contrast of RICM image can be maximized by adjusting the correction collar of the objective lens. To characterize absolute heights, contrast needs to be calibrated.

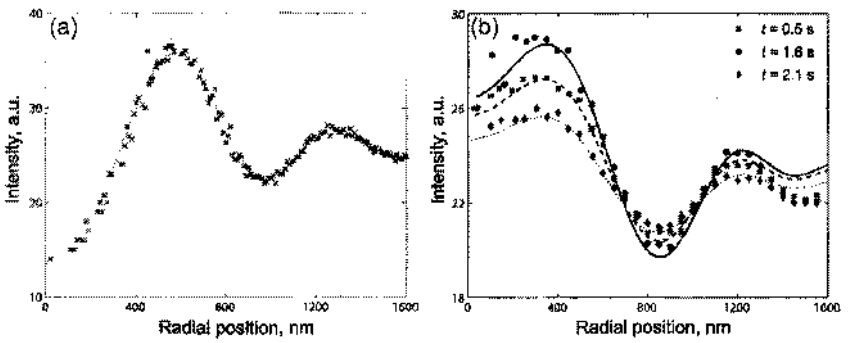

FIGURE 4.2: Radial intensities of RICM images of 3.2μm diameter silica particle.(a) Particle sticking on coverslip.(b) Particle in deionized water, in which it experiences vertical Brownian motion. The selected RICM images at three moments show the same phase distribution of intensity with different contrasts. In both plots, the colored dots are binned image intensities. Lines are fitting curves obtained from similar procedures as in Ref [100]

The total energy of a colloidal particle above a charged glass plate can be calculated by the summation of gravity and electrostatic interaction potentials. Van

Der Waals interaction is ignored due to the large separation h between them.

$$U(h) = \Psi_e(h) + F_g h \tag{4.4}$$

where $\Psi_e(h)$ is the electrostatic potential energy between particle and wall due to the overlap of their electrostatic double layer. If Debye length k^{-1} is smaller than particle-wall separation ($\kappa h > 1$) and smaller than the radius of particle ($\kappa a > 1$), $\Psi_e(h)$ can be determined by DLVO theory [100]. For a 1:1 electrolyte solution,

$$\Psi_e(h) = \Psi_0 e^{-\kappa h} \tag{4.5}$$

with

$$\Psi_0 = 64\pi\epsilon a(\frac{k_B T}{e})^2 \tanh(\frac{e\varphi_p}{4k_B T}) \tanh(\frac{e\varphi_w}{4k_B T}) \tag{4.6}$$

where ϵ is the dielectric constant of water, e is the elementary charge, and φ_p and φ_w denote surface potentials of particle and wall, respectively. The gravitational force to the particle is given by

$$F_g = \frac{4}{3}\pi a^3(\rho_p - \rho_w)g \tag{4.7}$$

where ρ_p and ρ_w are densities of silica particle and water, respectively, g is gravitational acceleration. By taking the derivative of Eq(4.5), The equilibrium height h_{eq} corresponding to minimum energy potential is

$$h_{eq} = \kappa^{-1} \ln(\frac{\kappa\Psi_0}{F_g}) \tag{4.8}$$

Assuming that φ_p and φ_w are constant, there is a monotonic relationship between h_{eq} and κ^{-1}, in which the particle will be repulsed further away from the charged glass bottom in solutions with weaker ionic strengths.

Based on above analysis of the RICM image contrast and the particle-wall interaction, we can see that the equilibrium height of silica particle varies with the ionic strength of solution, whereas the contrast of RICM image decreases monotonically with the elevation of particle. Therefore, in experiment, we should observe the contrast difference between RICM images of particle in solutions with different ionic strengths. Let us first examine height distributions of a silica particle in solutions with two different salt concentrations. Two adjacent wells of an 8-well chamber with No.1.0 borosilicate glass bottom contain salt solutions with concentrations of 100μM and 1000μM, respectively. A single silica particle in a well was focused by objective lens, and its RICM images in a 12μm$\times$12μm field of view were continuously recorded by the camera at 48 frames per second over 5 minutes to form a movie. Then the objective lens was switched to another well with the same measurement repeated again.

For each RICM movie, the height corresponding to each frame of a RICM movie was first determined in the range of $[0, \Delta h]$. As in [100], the center of interference rings was located first, then the intensity profile of each RICM image was compared with that of theoretically calculated RICM interferograms. The height can be determined in a precision of 10$\sim$15nm. After this step, heights h_i ($i = 1, 2, ..., m$ m is the number of frame, $h_i \in [0, \Delta h]$) can be obtained for each frame in a RICM movie.

A situation commonly happening during particle's Brownian motion was neglected in the first step, in which, a particle crosses Δh between two consecutive frames. To

address this situation, first, by the observation of the interference rings, the special frame j corresponding to the lowest height h_j of the particle in a RICM movie can be located. Then the 'naive' height of particle corresponding to each frames should be equal or greater than h_j, which can be denoted by

$$H_i = h_i + n\Delta h \qquad (n = 0, 1, 2, ... \quad H_i \geq h_j \ , \quad h_j \in [0, \Delta h]) \tag{4.9}$$

Because particles can easily jump back and forth around the critical value Δh, n is determined by the assumption that height difference between two consecutive frames should be minimum ($\min(H_{i+1} - H_i)$). In other words, we assume that the particle cannot move more than 250nm in height in one 20ms interval. Since the average step size is about 100nm, this assumption is reasonable. The 'naive' height distribution is constructed based on the lowest height h_j in the RICM movie instead of the absolute height value.

The 'naive' height distribution of particles in salt solutions with concentrations of 1000μM, 100μM and 50μM are plotted in Fig.4.3. A height with maximum probability appears for each concentration. If we consider the height with maximum probability in 'naive' height distribution as the true equilibrium height, our data show that silica particle will be repulsed further away from charged glass bottom in salt solution of 1000μM than that of 100μM, which contradicts with DLVO theory. Then, let us examine contrasts of RICM images, the contrast of each frame was obtained by subtraction I_{min} from I_{max}. Because two 'naive' height distributions overlap around $H = 140$nm, frames of RICM movies corresponding to 'naive' heights

in the range of 140 ± 10nm were selected to construct a contrast profile for each salt concentration, which are shown in Fig.4.3 inset. Contrasts of RICM images with salt concentration of 100μM are lower than that of 1000μM. The noticeable contrast decline implies the separation between particle and wall should be larger in salt solution with concentration of 100μM than that of 1000μM.

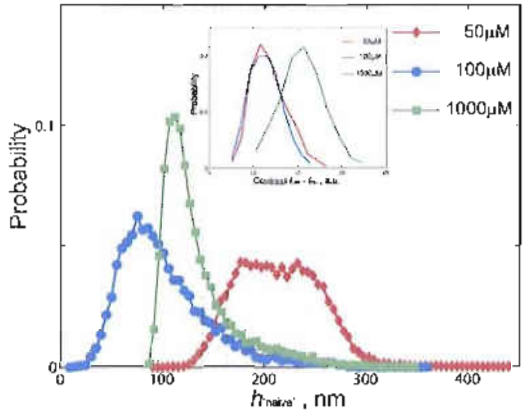

FIGURE 4.3: 'Naive' height distribution of a 3.2 μm diameter silica particle in solutions with salt concentrations of 50μM, 100μM and 1000μM, respectively. Inset: Contrast profiles constructed from RICM images corresponding to the determined 'naive' heights in the range of 140 ± 10nm(grey box with dot line) for each solution.

4.4 Absolute Height Measurements

In the above section, we have shown the possible capability of contrast comparison in absolute height determination by SW-RICM. However, the relationship between contrast and absolute height still needs to be characterized. The ionic strength of solution is a powerful tool to manipulate the separation between silica particle and wall. In a solution with high ionic strengths ([NaCl] > 10mM), particle will

stick on the surface of glass bottom with the separation between them around zero (Fig.4.1(b)), because Van Der Waals attraction between particle and wall will overcome the electrostatic repulsion between them. From this point, RICM images of particle in solutions with a series of salt concentrations in a descending order can be captured separately. Correspondingly, The equilibrium height of particle should be in an ascending order due to the nature of screened Coulomb repulsion. Discrete salt concentrations are carefully chosen so that particle in solutions of two adjacent salt concentrations each can sample absolute heights with a partially overlapped range, in which, RICM images of particles from two solutions should give similar contrast profiles. For example, as is shown in Fig.4.3, another 'naive' height distribution of silica particles is measured in a solution with salt concentration of 50μM. Frames corresponding the same range of 'naive' height as above were picked to construct a contrast profile which is similar to that with salt concentration of 100μM. Therefore, the shared 'naive' heights in salt concentration of 50μM and 100μM represent a range of absolute heights which particle can sample in both solutions. In this way, as heights of particle in different solutions are lined up, each solution for which the particles cross the critical value Δh can be determined. Finally, the absolute height distribution of silica particle in each solutions can be determined from its 'naive' height distribution by

$$H_i^{true} = H_i + N\Delta h \qquad (N = 0, 1, ...) \tag{4.10}$$

In experiments, salt solutions with several concentrations were respectively pipette

into each well of a 8-well glass bottom chamber. Absolute height distribution of silica particle in each solution was characterized by above method. Curves are shown in Fig.4.4(a). To further evaluate this method, equilibrium heights of silica particle versus salt concentrations are plotted in Fig.4.4(b). Mean heights $\langle h \rangle$ were used especially for solutions with low ionic strengths. Assuming surface potentials $\varphi_p = \varphi_w$, equilibrium heights can be well fitted using Eq(4.8) to get an estimated surface potential of 127mV, which agrees with the result previously measured [114].

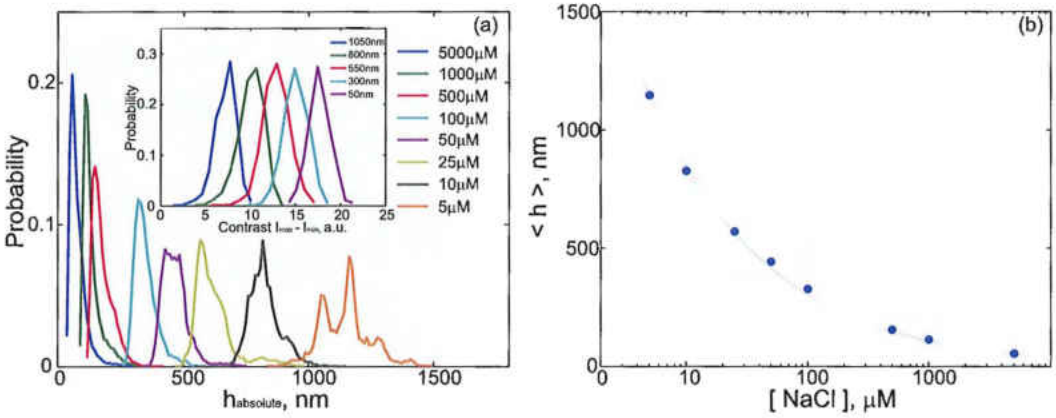

FIGURE 4.4: (a) Absolute height distributions of 3.2 μm diameter silica particle above glass bottom of chamber in solutions with a series of salt concentrations. Inset: Contrast profiles of RICM images corresponding to absolute heights.(b) Measured mean height $\langle h \rangle$ (blue dot) of 3.2μm silica particles in salt solutions with different concentrations. $\langle h \rangle$ can be fitted with Eq(4.8) (grey line) with surface potential of 127 ± 13 mV.

With the constructed absolute distributions above, the relationship between contrast and absolute height of particle can be figured out. For example, frames corresponding to absolute heights in a series of ranges of $(50 + N\Delta h) \pm 10$nm $(N = 0, 1, 2, 3, 4)$ are selected to construct contrast profiles, which are shown in

Fig.4.4(a) inset. For each increment Δh of absolute height, contrasts decrease with an equal amount of intensity shift. The maximum contrast should be set by the RICM image of stuck particle. According to Eq(4.4), the magnitude of contrast depends on the absolute height of particle. Therefore, the amount of contrast shift may varies with the range of absolute heights selected to compare. For the particle in a given RICM image, its relative height h ($h \in [0, \Delta h]$) can be determined by the fitting of image intensity. Image contrast will provide the number of periodicity $N\Delta h$, which needs to be added to h to get the absolute height of particle. In this way, absolute height of particle in an unknown solution can be easily determined without the non-trivial deduction process among solutions with different ionic strengthes.

To get a series of comparable contrasts between RICM images, the emitting intensity of arc lamp and the exposure time of camera should be fixed in all measurements. A silica particle with the diameter of 3.2μm experiences intense Brownian motions in solutions, especially in those with low ionic strengths, in which, between the interval of two consecutive frames (Δt = 20ms), particle can jump up and down with a span of 150 nm, which is a challenge for fast image acquisition and the 'naive' height determination. As particle becomes higher above wall, its position sometimes can be almost out of the focus depth of the objective lens, which will lower the signal to noise ratio in its RICM image. Moreover, despite of the help from field diaphragm in focusing, positions of focal plane still vary between measurements. These factors will affect the magnitude of contrast and hence the

constructed contrast profiles. In addition, contrast profiles are constructed based on particle with specific properties, any changes in particle, such as material, size, surface roughness, etc may result in the reconstruction of contrast profiles for absolute height determination. For lipid and protein functionalized particles, even though the coated layer is only several nanometers in thickness, the modified surface may lower the amount of reflective intensity collected by objective lens, and hence the contrast of RICM image due to its absorption and roughness. The RICM image contrast of a stuck functionalized particle can be compared with that of a stuck bare silica particle. If the difference between them is negligible, the contrast profiles obtained from unfunctionalized particle can be still applied to characterize absolute heights of functionalized particles. Otherwise, if screened Coulomb repulsion still dominates the interaction between wall and functionalized particles, absolute heights in a solution with specific ionic strength can be deduced step by step using a series of solutions with an descending order of ionic strength, in which, the maximum ionic strength can make particle stuck on glass bottom and yield an absolute height of zero, while, the minimum ionic strength is set by the solution where the particles are in. However, if particle is surrounded by deionized water, solutions with more specific salt concentrations are needed to figure out its absolute height. This process is time consuming.

4.5 Summary

In summary, we realized the measurement of particle's absolute height above a charged glass bottom in a solution by SW-RICM. Due to the nature of screened Coulomb repulsion, particles will rise following the decrease of ionic strength in solutions. During this process, even though the same phase distribution of intensity in RICM image repeats, the contrast will be monotonically reduced, which can eliminate ambiguity in absolute height determination by SW-RICM. With initial ionic strength set by stuck particle which gives an absolute height of zero, several salt concentrations are carefully selected in a descending order, in which absolute height of particles in each solution can be determined step by step with the help of contrast comparison. The method is demonstrated by the fit of measured absolute heights to the DLVO theory. Moreover, the relationship between contrast and absolute height can be constructed. The resulting contrast profiles can simplify the height determination process and make it applicable to particles in a variety of experimental contexts.

CHAPTER V

MODULATION OF COLLOIDAL PAIR INTERACTIONS BY LIPID FUNCTIONALIZATION

5.1 Introduction

Since 1994 [15], confinement-induced like-charge attraction has been intensively studied in experiments. In general, limitations in our understanding of this mysterious attraction contribute to the slow progresses in self-assembled microparticle superstructures. These difficulties arise in large due to the lack of experimental system with tunable, long-range, attractive interparticle interactions.

Due to their varieties and specific interactions, Biomolecules provide a new way to control colloidal interactions. Strong attractions between colloidal particles can be achieved by coating biomolecules with high binding affinities, such as biotin and streptavidin [115]. However, such attractions are poorly controlled and will lead to irreversible aggregation of particles. DNA is another widely used biomolecule to control colloidal interactions [91]. Hybridization between

complementary DNA strands can make DNA-linked particles attract each other. In addition, the temperature-dependent binding of DNA molecules allows reversibility of particle-particle adhesion. But due to the highly charged phosphate backbone of DNA molecules, hybridization affinity needs to compete with electrostatic repulsion between single strand DNA molecules. The resulting control of inter-particle interaction is only short-ranged, usually several tens of nanometers in scale. Recently, lipid bilayers, the ubiquitous bimolecular coating for cells, began to appear as a candidate for colloidal functionalization. Lipid vesicles can self-assemble on the surface of colloidal silica particles to form a lipid bilayer, where surface charge density can be easily regulated by tuning lipid compositions. Also membrane proteins can be incorporated to provide specific inter-particle linkages. Recent studies by Baksh et.al. [53]and Winter et.al. [54] have shown that phase transitions of lipid functionalized microparticle ensembles can be triggered by peripheral protein binding. The underlying physics of such phenomena suggests the potential of lipid bilayers to control colloidal pair interactions, but these interactions still remain poorly quantified.

In this chapter, we present pair potential measurements of lipid functionalized silica particles. The energy U as a function of center-to-center separation r of two identical particles was measured by our tunable line traps (Chapter III) near the glass chamber bottom . The adjustment of lipid composition gives rise to the modulation of charge density on particle surface, which results in tunable, long-range, attractive

colloidal pair interactions. The tunability of interactions allows the decomposition of pair potentials into charge-dependent and -independent terms, the former of which is found to be purely repulsive. The linear relationship between interaction energy and fraction of charged lipids suggests the influence of a confining wall as a dominant determinant on pair potential measurements. Finally, we will comment on the measured mysterious attractive colloidal interactions.

5.2 Experimental Methods

Silica Particles

Silica particles with 3.2μm in diameter were purchased from Bang Laboratories (cat.no.SS05N, density $\approx 2 g/cm^3$) as suspensions with 10^9 beads/ml. 30μl of bead suspension was diluted with 1ml DI water in a eppendorf tube followed by pulse vortexing. Centrifugation of the tube allowed particles to sediment on the bottom, the top supernatants were pipetted out. Then after the addition of fresh DI water and vortexing, the dispersed bead suspension in the tube were sonicated for 5 minutes in an ultrasound bath to detach stuck small impurities from particle surfaces. The surface roughness of particle was verified to be less than 10nm via scanning electron microscopy (Zeiss Ultra Scanning Electron Microscope)

Lipid Functionalized Silica Particles

The lipids listed below are purchased from Avanti Polar Lipids: 1,2-dioleoyl-sn-glycero-3-phosphocholine (DOPC, cat.no.850375), 1,2-diachyl-sn-glycero-

3-phosphoserine (DOPS, cat.no.840035), 1,2-dioleoyl-3-trimethylammonium-propane (DOTAP, cat.no.890890). Each kind of lipid is originally dissolved in chloroform. DOPC is a zitterionic (net neutral) lipid, whereas a net positive/negative charge exists in the headgroup of DOTAP/DOPS lipid molecule, respectively. Each kind of lipid has two unsaturated fatty acid chains, and is fluid in room temperature. The fluorophore-conjugated lipid Texas Red 1,2-dihexadecanoyl-sn-glycero-3-phosphoethanolamine purchased from Invitrogen (Texas Red DHPE, cat.no. T-1395MP) is originally in the form of powder, which is dissolved in chloroform after arrival. Texas Red DHPE is used as fluorescent label to examine the intactness of coated lipid bilayers on the surface of silica particle. In addition, it is anionic, contributing a net negative charge per molecule to the mixture of lipids. Each kind of lipid is diluted with additional chloroform to desired stock concentrations and stored in a glass vial for later use.

For each lipid composition, the total mass of mixed lipids was 1mg, and the volume of each lipid in chloroform was calculated according to its molar percentage in lipid mixture and its stock concentration. Lipids were mixed together in a pear-shaped flask which was cleaned by piranha solution and rinsed by chloroform before use. Each sample was dried in vacuum for 2 to 3 minutes and then evacuated for at least 2 hours to make chloroform evaporate completely. The dried lipid film in flask were hydrated with 1ml DI water and kept overnight at 4 °C in the dark to protect fluorophore from bleaching.

A lipex extruder (Northen Lipids) was used to generate small unilamellar vesicles (SUVs). Lipid suspension from previous day was pipetted into extruder with a 100nm polycarbonate filter placed in its bottom. The pressure of flowing nitrogen gas inside extruder pushes lipid suspension to pass through the filter and the extruded sample was collected. SUVs with uniform size (about 100nm in diameter) were formed by repeating this process at least 10 times. Before the extrusion of next sample, the filter was washed by extruding 1ml of DI water for several times to clean any lipid residue left from previous sample.

A spreading solution was prepared by mixing 30μl SUVs solution with 60μl 1X phosphate buffered saline (PBS) in an eppendorf tube. 30μl bead suspension was pipetted into the spreading solution followed by pulse vortexing. Lipid bilayers self-assembled on the surface of silica particle after several minutes of incubation. Centrifugation of the tube allows the sediment of functionalized particle at its bottom, then the top fluid in the tube was exchanged with DI water, and particle suspension was vortexed to mix again. Unruptured SUVs were rinsed out by repeating these steps.

Optical Line Traps

Optical line traps were generated by the method introduced in chapter III. In brief : A spatial light modulator (SLM) was illuminated by a diode laser(Meshtel RS655-70, 655nm, maximum output 70mW)at a output power of 14mW. The diffracted beam with modulated wavefront was focused by a NA = 1.2, 60X water immersion

lens (Nikon) on a Nikon TE2000-S inverted microscope to create a 60μm line trap in the focal plane. In order to hold particle near the line center to decrease the time of separation sampling, $\sigma = 7.5$ in Eq(3.7) was adopted in line trap generation to introduce a net gradient force exerted on particles.

Pair Potential Measurements

A dilute lipid functionalized bead suspension was pipetted into a 8-well chamber with NO.1.0 borosilicate coverglass bottoms (Lab-Tek, Nalge Nunc International) containing DI water. Particles were allowed to sediment by gravity near the glass bottom of chamber with density of several particles per 100μm $\times$ 100μm field of view. Images of particles were captured in a 10μm $\times$ 40μm area with a rate of 16 frames per second. For each set of measurement, examined by fluorescence appearance, two lipid-coated particles with uniform fluorescence intensity each were selected. First, a single particle was confined in a line trap with its motion captured in 60 minutes. Then the second particle was pulled in the trap, and the images of colloidal pair were recorded for 50 $\sim$ 60 minutes. The true pair interaction was calculated based on the method described in Chapter III. For each lipid composition, 5 $\sim$ 10 sets of particle pair were selected with pair potential measured each and $U(r)$s plotted in this chapter are typical curves. Supposing that the calculated interaction energy from Boltzmann relationship is $U(r)$ plus an arbitrary offset, the offset can be determined by $U(r \to \infty) \to 0$ with large-r limit of U evaluated by $\frac{dU}{dr} < 0.1 k_B \mathrm{T}/\mu\mathrm{m}$. The well depth, ΔU, was evaluated from a cubic fit of $U(r)$ near the vicinity of minimum.

Particle Tracking

Positions of particles were tracked by home-made MATLAB programs based on the well-established tracking algorithm [77]. The precision of locating particle center is about 20 nm as estimated by tracking the position of stuck particle. The error in separation determination due to image artifacts has been characterized in Chapter III, the magnitude of such effect is negligible with a shift of observed separation about 15nm. Moreover, this error would be presented in all our measurements and so that it cannot affect the relative difference between $U(r)$s measured for different lipid compositions.

5.3 Experimental Results

Single, continuous lipid bilayers readily self-assemble on silica surfaces [116]. Lipid functionalized silica microparticles were made using established techniques [53, 54]. Membrane coatings consist primarily of the zwitterionic (neutral) phospholipid DOPC, with 0.5mol% anionic fluorescence probe Texas Red DHPE and various amounts of the negatively charged lipid DOPS or the positively charged DOTAP. See the experimental methods section for abbreviations and details of sample preparation. Silica microspheres coated by membranes with net molar percentages of positively charged lipids, Z_{lipid}, between -4.5 and +3.5, were examined. Fluorescence microscopy shows the uniform fluorescence appearance of the particles.

In experiments, we focused on pair interactions of lipid functionalized microparticles

near a confining wall, motivated by the mysterious confinement-induced like-charge attraction and by the triggered phase transitions in membrane-coated particle ensembles near a glass wall [53, 54]. 3.2μm diameter silica particles are massive enough to settle near the glass chamber bottom by gravity, while still being small enough to undergo significant lateral Brownian motion. Therefore, we allowed a dilute beads suspension to settle near the vicinity of glass chamber bottom. As is shown in Fig.5.1(a), two particles coated by membranes with the same lipid composition were confined in a line trap. The interaction energy between them was characterized by the procedure described in the experimental methods section. At least 5 measurements were performed for each composition. The power of laser illuminating line trap (14mW) was too low to move the trapped particles perpendicular to focal plane followed by the shift of laser focus. The height of particles above the wall was still determined by the balanced between its gravity and electrostatic repulsion from the wall, with a small shift ($<$ 50nm) induced by the laser focus position, as measured by RICM.

The measured pair potential curves are shown in Fig.5.1(b). We found that the pair interaction energies can be tuned over a wide range by altering the lipid compositions. The tuning range of attractive interactions is about $1k_BT$. At short separations, the measured pair potential curves in all data sets are roughly parallel with each other, which suggests a similar screening length of electrostatic repulsion independent of lipid compositions. For highly negatively charged membranes

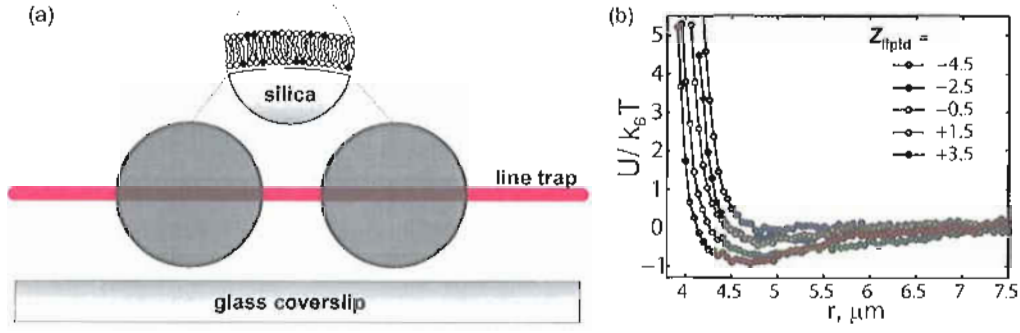

FIGURE 5.1:(a) A schematic diagram of pair interaction measurements of lipid-only functionalized microparticles. Two membrane-coated microparticles are confined by line trap near the vicinity of glass chamber bottom. Two silica particles were coated with membrane with the same compositions.(b) Representative pair interaction energies, U(r). The net molar percentage of ionizable lipids, Zlipid, was controlled via the fraction of anionic DOPS ($Z_{lipid} < 0$) and cationic DOTAP ($Z_{lipid} > 0$) lipids in the membrane. The overall particle charge is negative in all cases. The data points are connected by lines as guides to the eye.

(4mol.% DOPS, Z_{lipid}= -4.5%), the pair interaction of particle is purely repulsive. With increasing positive membrane, attractive minima in $U(r)$ began to appear and become deepest with Z_{lipid}= + 3.5% (4mol.% DOTAP). Particles coated with membranes containing more than 4mol.% DOTAP stuck on the glass chamber bottom without the exhibition of Brownian motion. Studies on lipid bilayer supported by planar substrate have shown that Z_{lipid}− 4% counterbalances the negative charge of glass substrate [117]. Therefore, for particles coated by membranes with Z_{lipid}= 4%, it is most likely to be positively charged and immobilized on the negatively charged glass bottom of chamber by electrostatic adhesion.

5.4 Analysis and Discussion

In the above section, we have shown that attractive pair colloidal interactions can be modulated by coated membranes. These results arouse our contemplation on one of deepest mysteries in colloidal science: attractions between likely charged colloidal particles near the vicinity of confining wall, which contradicts with the prediction of DLVO theory. Even though several theoretical explanations have been proposed, none of them can explain the mysterious attraction in all experimental conditions. Previous experiments were based on silica or polymer particles, which were chemically simple and the electrostatic properties of their surfaces cannot be readily altered. Here, the modulation process of attraction presented in our experiments is absent in previous studies, the dependence of attractive colloidal interaction on the amount of charged lipid in coated membrane can yield insights into like-charge attraction.

Analysis of modulated $U(r)$s allows the separation of various contributions to pair potential. As is shown in Fig.5.1(b) and 5.2, there is a dependence of pair potentials on Z_{lipid}, the amount of charged lipids in coated membrane on microparticle. There is a linear relationship between the depth of attractive potential, ΔU and Z_{lipid} (Fig 5.2(a)). Considering the original charges on the surface of silica microsphere, which is related with an offset term Z_0, the total charges of lipid-coated particles can be denoted by $Z = Z_{lipid} + Z_0$. Then we can write $U(r, Z) = f(Z)U_e(r) + U_n(r)$, where $f(Z)$ is a function of Z. The pair interaction energy can be decomposed into two parts. $U_e(r)$ is the potential of interactions between particles directly related to Z, whereas

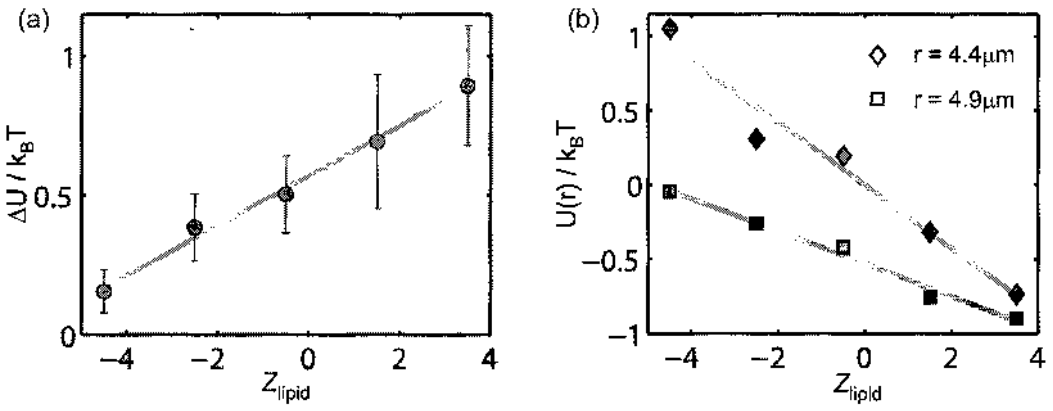

FIGURE 5.2: (a) The depth of attractive potential ΔU vs Z_{lipid}. The points are averages of at least 5 data sets with each composition and the error bars indicate standard deviations. The solid line is a linear fit. (b) $U(r)$ versus Z_{lipid} for two values of r (points), with linear fits (lines).

$U_n(r)$ includes indirect electrostatic and non-electrostatic interactions independent of lipid compositions. Carefully examining pair potential curves, we found that not only is the depth of attractive potential well, ΔU linearly proportional to Z_{lipid} (Fig.5.2(a)), but also, for any given separations r, $U(r)$ alters linearly with Z_{lipid} (Fig.5.2(b)). This suggests that $f(Z)$ is a linear function: $f(Z) = -Z = -(Z_{lipid} + Z_0)$, the minus sign reflects the increasing of repulsion with the addition of negatively charged lipids. $U(r)$ can therefore be denoted as

$$U(r, Z_{lipid}) = -(Z_{lipid} + Z_0)U_e(r) + U_n(r) \tag{5.1}$$

Therefore, by fitting $U(Z_{lipid})$ linearly with Z_{lipid} at each given separation r, $U_e(r)$ can be given by the slope, plotted in Fig5.3(a). At each r, the average of $U(r)$s from several data sets with each membrane composition were examined as a function of Z_{lipid}

derived as $U(Z_{lipid})|_r$. $U_e(r)$ was calculated from $U(Z_{lipid})|_r$ for each composition. Two such data sets of $U(Z_{lipid})$ are plotted in Fig.5.2(b) at $r = 4.4$ and 4.9μm, respectively. Note that $f(Z)U_e(r)$ is a measure of energy; $U_e(r)$ alone measures energy per unit Z. We find that $U_e(r)$ is purely repulsive, in agreement with predictions of electrostatic interaction [96]. However, instead of a simple form of Coulomb screening repulsion, it can be well fitted with a superposition of two such forms (Fig.5.3(a))

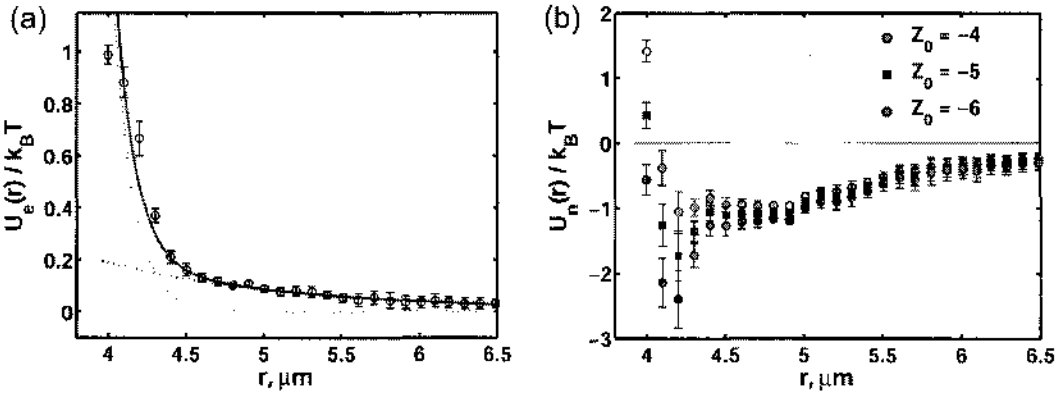

FIGURE 5.3: (a) $U_e(r)$, the particle-charge-dependent contribution to the pair interaction energy per unit Z_{lipid}. The error bars indicate uncertainties in the linear fits of U versus Z_{lipid}. The solid line is a fit to the sum of two exponential curves, each term of which is indicated with dashed lines. (b) $U_n(r)$, the particle-charge-independent contribution to $U(r)$, derived with different assumed values of the offset charge Z_0. Distances are plotted in terms of the center to center distance r.

$$U_e(r) = A_1 \frac{\exp(\kappa_1 r)}{r} + A_2 \frac{\exp(\kappa_2 r)}{r} \tag{5.2}$$

One screening length, $\kappa_1^{-1} = 0.13 \pm 0.01\mu$m, agrees with the fitted Debye screening length obtained from pair potential measurement of bare silica particles in Chapter III. The other, $\kappa_2^{-1} = 1.5 \pm 0.1\mu$m, is fairly large and comparable to the radius of

particle. Both Z_0 and $U_n(r)$ contribute to the intercept of linear fit of $U(Z_{lipid})$ with Z_{lipid}. Considering that membranes with more than 4 mol.% DOTAP coated on planar silica substrate will cancel out the original negative charges on silica surface, the offset term Z_0 should be around -4. $U_n(r)$s with $Z_0 = -4$ to -6 are plotted in Fig.5.3(b). Even though the form of $U_n(r)$ cannot be determined, $U_n(r)$s for all given values of Z_0 are attractive with a similar depth of $1k_BT$.

The linear relationship between U and Z_{lipid} is amazing. For the range of Z_{lipid} investigated in our experiments, recent measurements of separation between individual lipid-coated silica microsphere and coverslip revealed a linear relationship between particle surface potential ψ and Z_{lipid} with $|\psi| < 50$mV. Therefore, our observation implies $U \sim \psi$. For small surface potential $|\psi| < 25$mV, we would expect that the pair potential of identical spherical colloidal particles should increase quadratically with its surface potential, as $U \sim \psi^2$. However, the linear scaling $U \sim \psi$ implies that particle-wall interaction dominates pair colloidal interaction measurements, in which, $U \sim \psi_{particle}\psi_{wall}$ rather than $U \sim \psi_{particle}\psi_{particle}$. If considering the constant surface potential of wall, particle-wall interaction can be characterized by $U \sim \psi$.

The actual charge density on the surface relates with Z_{lipid}, but the scaling relation between them are complicated. Since the average separation between charges is on the order of 10nm, less than the Debye screening length, interactions between charged groups of hydrophilic heads are significant. The molar percentage of lipids with

net charges in solution may be far less than Z_{lipid}, so we cannot expect the actual charge density scales linearly with Z_{lipid}. Further, we cannot conclude that ψ is linear proportional to the actual charge density.

For like-charge attractions examined in our experiments, we also attempted to fit pair potentials to some models, e.g. DLVO model. For example, The pair potential with maximum attractive well (4mol.% DOTAP) can be well fitted with Eq(3.17). If we take the attractive pair potential for granted as Van Der Waals interaction, the fitting yields a Hamaker constant 200 times larger than that of silica in aqueous solutions. This suggests that Van Der Waals interaction cannot account for this mysterious attraction between particles, in agreement with the conclusion made by Kepler in 1994 [15]. Even though the lipid bilayer is coated on silica particle surface, it is so thin that its contribution to Van Der Waals attraction between particles is negligible. Unruptured SUVs (100nm in diameter) have been rinsed out before pair potential measurements, and less than 1μl beads suspension was pipetted into a well of chamber containing 400 μl DI water. Concentrations of small particles, such as SUVs or impurities originally on silica particles, are too low to provide prominent depletion attraction between particles. However, considering the structure of lipid-coated silica particle, the membrane on the silica surface is still a fluid, and ionized lipids can move around. With the presence of the negatively charged confining wall, the ionization of molecules in the area on particle surface close to the wall will be more strongly influenced than that in other areas. The

same situation also happens in the area of one particle close to the other. Such effects will give rise to an asymmetric charge distribution on particle, and hence an asymmetry in counterion clouds around the particle. We speculate that the resulting dipolar or higher-order forces between microparticles may be important. The length scales of such interactions will be similar to that of charge inhomogeneity, on the order of particle radius. This scale is similar to the second screening length κ_2^{-1} deduced above. Some studies [118, 119] have shown the existence of attraction between particles with inhomogeneous charge distributions. However, it is still unclear whether this explanation can be applied to confined colloidal particles. In addition, due to Brownian motion of particle, such asymmetric charge distributions on the surface of lipid-coated microspheres can be modulated by particle-particle and particle-wall separations, the resulting charge fluctuations further complicate the situation. Other factors, including the dynamics of local ion clouds and the rotational Brownian motion of the particles, may also contribute to the exact form and magnitude of these interactions.

5.5 Summary

In this chapter, following the introduction of experimental methods, we presented the pair potential measurements of lipid functionalized microparticles near the vicinity of a charged confining wall. By tuning lipid compositions to modify the charge density on colloidal surfaces, attractive colloidal interactions can be

modulated in a range of $1k_BT$, and the depth of attractive potential was found to be linearly proportional to Z_{lipid}. Compared with previous results on confinement-induced like-charge attraction, our data provided a set of $U(r)$s and showed the modulation process of attractive interactions, which makes it possible to separate factors contributing to interactions among the microparticle and the confining wall. The particle-charge-dependent term is purely repulsive, making it clear that the mysterious attraction is not simply due to charge. Moreover, the linear relationship between $U(r)$ and Z_{lipid} implies the domination of particle-wall interactions on colloidal pair interaction measurements. Even though our data cannot provide a solution of like-charge attraction, the control of colloidal interactions by lipid functionalization illuminates this long-standing unsolved puzzle in colloidal science.

CHAPTER VI

MODULATIONS OF ATTRACTIVE COLLOIDAL INTERACTIONS BY LIPID AND PROTEIN FUNCTIONALIZATION

6.1 Introduction

In previous chapter, we have shown the modulation of attractive colloidal interactions by lipid functionalization. However, even though the decomposition of pair potentials can remove the paradox inherent in like-charge attraction, as the attraction is not (directly) due to the first order charge-charge interaction, the mystery of like-charge attraction is still unsolved.

The functionalization of microparticles with lipid bilayer membranes has been demonstrated as a powerful methodology for achieving control of particle properties. Surface charge density of particle can be readily altered by the control of lipid compositions, the ability of which to mediate colloidal interactions has been shown in previous chapter. In addition, lipid bilayers with enhanced mechanical stability

offered by microparticles make it possible to simulate the real environments of cellular membranes. Surface of silica microparticles can be further modified by binding peripheral proteins on membrane coatings. Ionized groups in bound proteins can also modulate the surface charge density of particle, and the change of diffusion coefficient in supported lipid bilayers have been observed with the presence of bound proteins [53, 54]. Moreover, Recent studies have shown that binding peripheral proteins Cholera Toxin Subunit B (CTB) to lipid ligand monosialogangsolioside G_{M1} on the microsphere-supported membrane, can trigger dramatic transitions between condensed and dispersed phases in many-body systems. This suggests that protein binding can be another effective method to mediate interactions between microparticles. However, it is still unclear whether such transitions is governed by two-body or higher order interactions, and fundamental interactions between such functionalized particles, i.e. pair interactions, still remain unexplored.

In this chapter, we will first report the measurements of pair interaction energies between lipid-plus-protein functionalized silica microparticles. Our data show the control of pair interactions can be achieved by binding different numbers of CTB to its ligand lipid G_{M1} coated on silica microparticles. Depths of attractive potentials are weakened followed by the increased number of CTB bound on G_{M1}, in a relation similar with that obtained in many-body measurements. Next, we will compare modulations of attractive colloidal interactions provided by lipid-only and lipid-plus-protein functionalizations. Analysis from potential curves and measurements

of particle-wall separations show remarkably differences between these two systems. Besides the demonstration of a new biomimetic way to control colloidal interactions, our results imply that mechanisms underlying like-charge attraction may be not unique and several factors may account for its existence.

6.2 Experimental Methods

Materials

The same silica particles with 3.2μm in diameter were used as those described in preparations of lipid-only functionalized particles. For lipid-plus-protein functionlized particle, coated membranes consist of 97.5 mol% 1,2-dimyristoleoyl-sn-glycero-3-phosphocholine (DMOPC, zwitterionic), 1.5 mol % 1,2-dioleoyl-sn-glycero-3-ethylphosphocholine (DOEPC, one net positive charge per lipid molecule), 0.5 mol % Ganglioside G_{M1} (G_{M1}, one net negative charge per lipid molecule), 0.5 mol % fluorophore-conjugated lipid TR-DHPE (one net negative charge per lipid molecule). For lipid-only functionalized particles, the compositions are the same as those described in the previous chapter. All lipids were purchased from Avanti Polar Lipids except for TR-DHPE, which was purchased from Invitrogen. FITC-labeled florescence CTB powder was purchased from Sigma-Aldrich. Initially, CTB powder was dissolved in 1X PBS solution for later use

Sample Preparation

Lipid functionalized microparticles were prepared by the procedures described

in previous chapter. For lipid-plus-protein functionalized particle, dilute lipid functionalized particle suspension were mixed with CTB solutions with various concentrations (1 to 1000nM) which were diluted from stock concentration in PBS. These mixtures in eppendorf tubes were placed on a rotating rack in dark to incubate for about 45 minutes to 1 hour. After that, unbound CTB was removed by repeated rinsing steps of centrifugation and vortex mixing.

Examination of FITC-labeled CTB on Particles

Fluorescence of FITC-labeled CTB on particle was examined by florescence microscopy. For each CTB incubation concentration, a fluoresence image of a single particle was recorded over an area of $12 \times 12\mu m^2$. Fluorescence intensities of particles were determined by subtracting the average intensity in background area from that in particle area. The plotted points in Fig.6.1(a) represent the averaged fluorescence intensity from 20 to 25 particles.

Pair Potential Measurements

Pair interaction energies $U(r)$ were measured as described in detail in the previous chapter.

Particle-wall Separation Measurements

The separation between particle and confining glass chamber bottom was determined using RICM with a precision of 10nm. Light from a mercury lamp filtered by a 535 ± 20nm band-pass filter was used to illuminate particle. RICM

images of single particles were captured over a $12 \times 12 \mu m^2$ area with 48 frames per second. For each composition or experimental configuration, 10 to 15 sets of RICM data were taken, The mean particle-wall separation $\langle h \rangle$ was calculated from the Brownian distribution of h. The detailed procedures of mean height measurement have been introduced in Chapter IV.

6.3 Experimental Measurements

FITC-labeled CTB was bound to lipid-functionalized silica microparticles by the procedures described above. Florescence images show uniform CTB binding (Fig.6.1(a)). The normalized fluorescence intensity was plotted as a function of the incubated CTB concentration in Fig.6.1(b), which can be well fit to a langmuir isotherm with a dissociation constant of $K_{D,fluor} = 35 \pm 8$nM. This result is consistent with other measurements of CTB binding to supported membranes [54], indicating that the protein binds to the lipid bilayer as expected.

Two particles with the same incubated CTB concentrations were confined in a line trap. Pair potentials were measured near the vicinity of glass chamber bottom (Fig.6.2(a)). Interaction energies for microspheres prepared with varying [CTB] are shown in Fig.6.2(b) and exhibit tunable pair interaction energies that can be strongly attractive. The well depth of attractive potential, ΔU, decreases monotonically with incubated CTB concentration in a manner well fit by a Langmuir isotherm

$$\Delta U = \Delta U_0 \frac{K_D}{K_D + [CTB]} \tag{6.1}$$

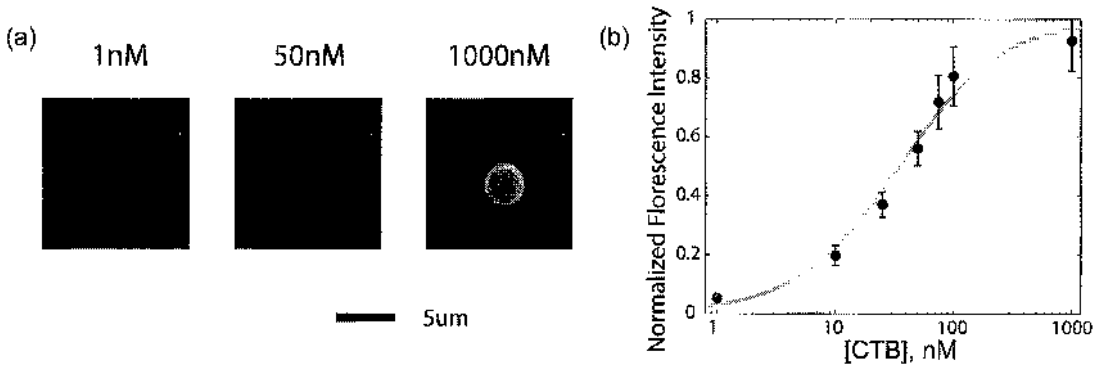

FIGURE 6.1: (a) Typical fluorescence images of lipid-plus-CTB functionalized silica microparticles with different CTB incubation concentrations. (b) Normalized, background-subtracted fluorescence intensity of CTB on particles versus CTB incubation concentration. Solid line is a fit to a langmuir isotherm with an effective dissociation constant of $K_{D,fluor}$=35±8 nM.

where ΔU_0 is the depth of attractive potential as [CTB] $\rightarrow$ 0. The fitting gives $K_D = 33 \pm 6$nM, which is identical within uncertainty to $K_{D,fluor}$ noted above.

Measured mean separations between particle and glass chamber bottom, $\langle h \rangle$, are shown in Fig.6.3. For CTB-bound microparticles, $\langle h \rangle$ decreases as more CTB were bound on the surface of particle. The height of a particle is determined by a balanced between its gravity and electrostatic repulsion from the negatively charged glass bottom. Increasing the concentration of bound CTB leads to more positively charges to counterbalance original negative charges on silica microspheres so that particles will become closer to the charged wall. The relation between $\langle h \rangle$ and [CTB] can be well fitted to a Langmuir isotherm with a similar dissociation constant, $K_{D,h} = 33 \pm 8$nM. For lipid-only functionalized microparticles, $\langle h \rangle$ versus Z_{lipid}, the net molar percentage of positively charged lipids, is plotted in Fig.6.3. As

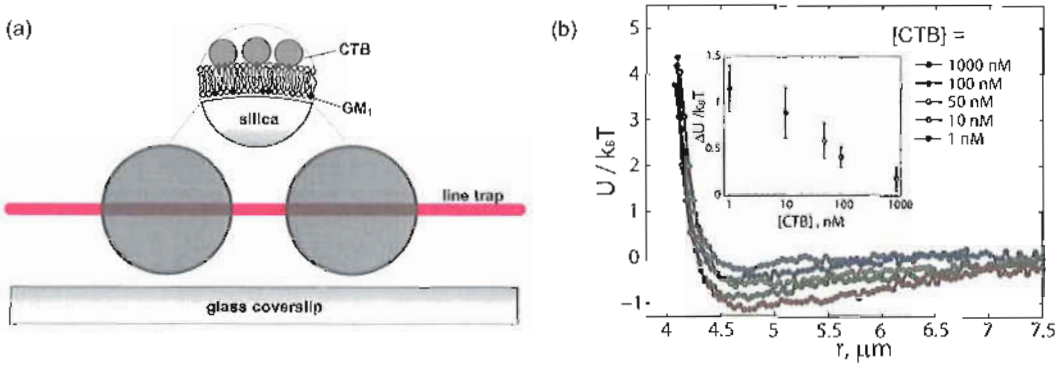

FIGURE 6.2: (a) A schematic diagram of pair interaction measurements of lipid-plus-CTB functionalized microparticles. (b) Representative pair interaction energies, $U(r)$. Pair interaction energies, $U(r)$, for silica microspheres functionalized with lipid membranes containing 0.5mol% G_{M1} and incubated with different concentrations of CTB. Inset: Attractive well depth, ΔU, versus [CTB]. The solid curve is a fit to a Langmuir isotherm with an effective dissociation constant of K_D=33±6 nM.

expected, the more neutral the coated membrane is, the closer the particle is to the wall. Particles with $Z_{lipid} > +3$ (i.e. with membrane containing more than 3 mol% DOTAP) adhered to the glass bottom.

6.4 Analysis and Discussion

The data show that lipid-plus-protein functionalization yields attractive pair potentials between microparticles, which can be modulated by [CTB]. Properties such as the fluorescence intensity of bound CTB on particle, the depth of attractive potential ΔU and the particle-wall mean separation $\langle h \rangle$ each shows a dependence on [CTB], well described by a Langmuir isotherm with $K_D \approx 33$nM. The common Langmuir form reveals that both ΔU and $\langle h \rangle$ are simply linear proportional to the amount of CTB bound on supported membrane. K_D is also identical within

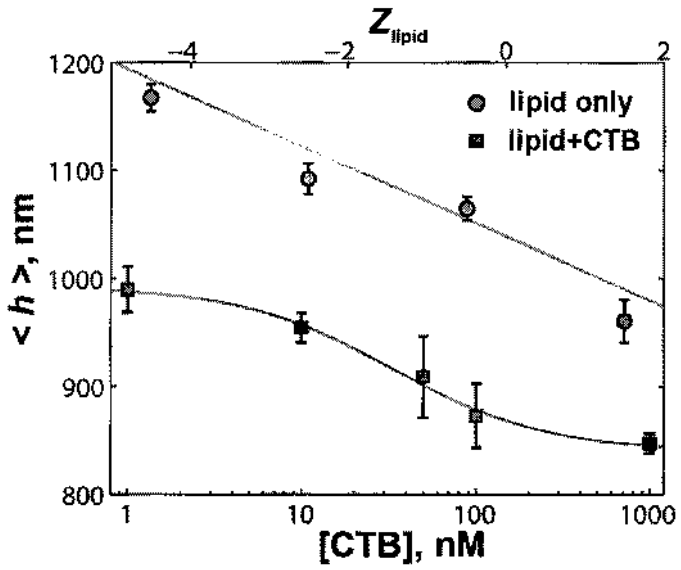

FIGURE 6.3: Mean particle-wall separation, $\langle h \rangle$. For lipid-only particles, $\langle h \rangle$ is plotted as a function of the net molar percentage of ionizable lipids, Z_{lipid}; the solid line is a linear fit. For CTB-bound particles, $\langle h \rangle$ is plotted as a function of the incubation concentration of CTB; the solid curve is a fit to a Langmuir isotherm with an effective dissociation constant of $K_{D,h}$=33 ± 8 nM

uncertainty to the effective dissociation constant measured in many-body particle distribution function. This implies that previous reported CTB-triggered colloidal phase transitions[54] may be understood in the context of pairwise interaction.

Both lipid-plus-CTB and lipid-only functionalizations examined in previous chapter lead to tunable, attractive pair interactions. Both lipid bilayers (thickness ~ 5nm) and CTB (a few nanometers in extent) provide molecular scale surface coatings for 3.2μm diameter silica core. From the similar structures, we would expect the same mechanisms of regulating surface charge density of the composite particle. Therefore, we predicted that both functionalizations should yield similar forms of

colloidal pair interactions, and two sets of measurements could be simply mapped onto one another. Surprisingly, the analysis of the data shows this is not the case.

The analysis of potential curves shows a fundamental difference in interacting forms between lipid-only and lipid-plus-CTB functionalization. Two properties that characterize $U(r)$ are ΔU and the effective range of attraction, $\langle r \rangle$, which is defined by

$$\langle r \rangle = \frac{\int_{U<0} rU(r)dr}{\int_{U<0} U(r)dr} \tag{6.2}$$

The data from measurements of lipid-only functionalized microparticles show a negative correlation between ΔU versus $\langle r \rangle$ (Fig.6.4(a) circles), whereas for lipid-plus-CTB functionalizaiton, the correlation is positive; the strongest attractions are the longest ranged. The lipid-only data show a linear dependence of ΔU on the molar fraction of charged lipids, Z_{lipid}, ΔU varies with [CTB] in a form of Langmuir isotherm, as does the fluorescence intensity of bound CTB varies with [CTB]. The identical dissociation constant within uncertainty indicates the a linear dependence of ΔU on the surface density of protein. However, the shared dependence of ΔU on surface concentration for both charged lipids and CTB does not lead to shared behavior of the interaction range but rather the qualitatively different behavior plotted in Fig.6.4(a)

Analogous to decomposition of lipid-only data into charge-dependent and -independent terms, pair potentials of CTB-bound microparticles can be decomposed

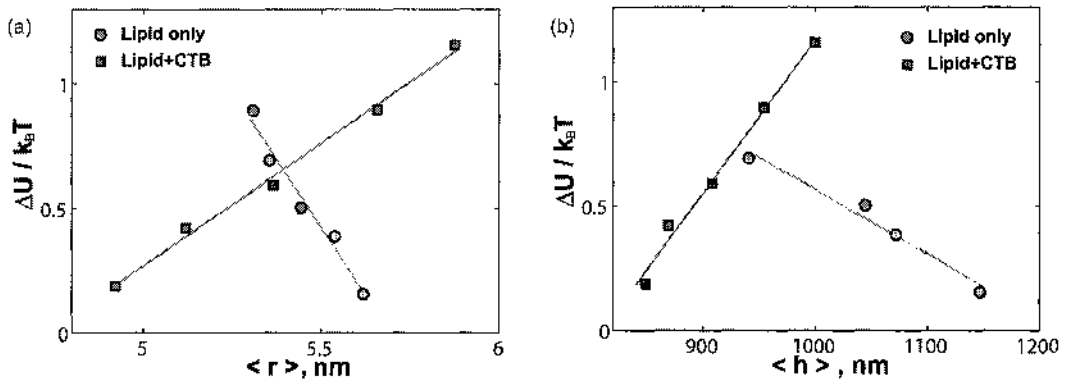

FIGURE 6.4: (a) Attractive well depth, ΔU, versus the interaction range,$\langle r \rangle$, for lipid-only and lipid-plus-CTB membrane-functionalized particles. The solid lines are linear fits. (b) Attractive well depth, ΔU, versus the mean particle height, $\langle h \rangle$, for lipid-only and lipid-plus-CTB membrane-functionalized particles. The solid lines are linear fits.

into two parts.

$$U(r, \sigma) = f(\sigma) U_{CTB}(r) + U_m(r) \tag{6.3}$$

where σ is the surface concentration of bound CTB and U_{CTB} and U_m are terms that do and do not depends on CTB coverage, respectively. The quantification of CTB fluorescence provides a measure of σ, and there is a roughly linear relationship between ΔU and σ at each fixed r (Fig.6.5(b)inset). The slopes and intercepts give U_{CTB} and U_m respectively. As shown in Fig.6.5(a), U_{CTB} is repulsive but not monotonic, whereas the CTB-independent term U_m (Fig.6.5(b)) is similar to $U(r)$ from lipid-only particles. On the whole, the bound CTB gives rise to a long-range repulsive interaction between particles to conterbalance the induced attraction by lipid coating. However, we cannot provide qualitative explanations of this behavior but speculate

that CTB dissociating from the membrane forms a cloud of large macroions, which may induce nontrivial electrostatic or entropic interactions between particles. The very low off-rate of CTB binding to G_{M1} [120], $k_{off} = 10^{-5}s^{-1}$, indicates that such a cloud would be very dilute and would fluctuate greatly, and its effect are likely beyond the reach of mean-field theory.

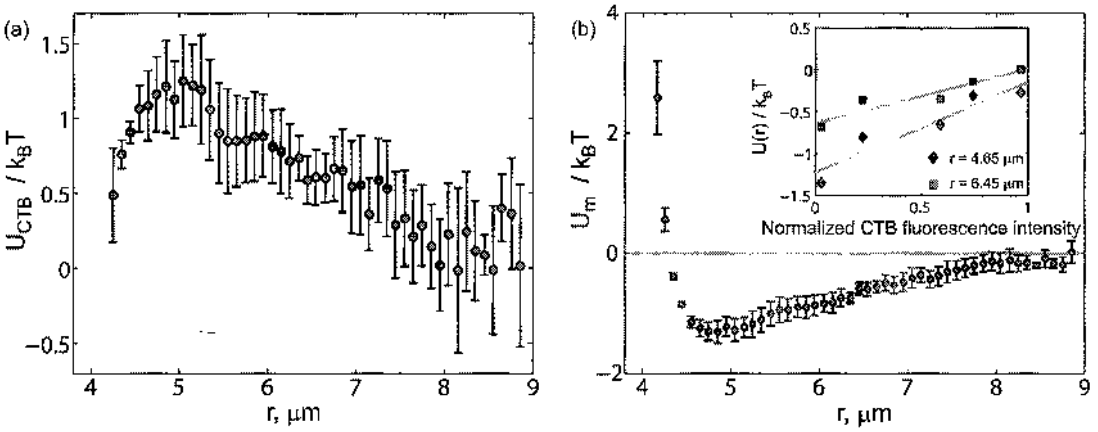

FIGURE 6.5: (a) $U_{CTB}(r)$, the [CTB]- dependent contribution to the pair interaction energy. (b) $U_m(r)$, the [CTB]-independent contribution to $U(r)$. The error bars indicate uncertainties in the linear fits. (Inset) $U(r)$ versus the fluorescence intensity of bound CTB (proportional to the surface concentration of the protein) for two values of r (points), with linear fits (lines).

The analysis of ΔU versus $\langle h \rangle$ provides further evidence of different behaviors from different biomolecular functionalizations. Both functionalization show dependence of $\langle r \rangle$ on composition(Z_{lipid} or [CTB]), and give a range of $\Delta U \approx k_BT$ corresponding to a range of $\langle h \rangle$ about 200nm. This indicates that like-charge attraction is sensitive to the particle-wall separation, as has been exhibited in previous experiments [16]. However, as shown in Fig.6.4(b), the correlation between ΔU and $\langle h \rangle$ is opposite

for the lipid-only and CTB bound microparticles. For CTB-bound particle with [CTB] = 1nM, it would be slightly positively charged. Correspondingly, its $\langle h \rangle$ is well located between that of Z_{lipid}= -0.5 mol% and +1.5 mol%. From this point, increasing the amount of negatively charged lipids will increase $\langle h \rangle$ and lower ΔU for lipid-only functionalized microparticles, whereas on CTB-bound side, more CTB bound on particle yields weaker attractions with larger particle-wall separations. This leads to an important conclusion that the particle-wall separation cannot be the primary determinant of like-charge attraction in colloidal systems. In other words, earlier studies [15, 16, 121] have demonstrated that the confining wall is important for the generation of attractive interparticle forces. In previous chapter, we have shown that pair interaction energies between lipid-only functionalized microparticles scale linearly with particle's surface potentials, which implies that the particle-wall interaction mediates pair interaction measurements between particles. With the comparison of attractive colloidal interaction modulations provided by two different functionalizations, we can further conclude that the wall is important, but its role cannot be solely characterized by $\langle h \rangle$. $\langle h \rangle$ does not uniquely specify the interparticle interaction energy.

6.5 Summary

In summary, we showed another effective way to control attractive colloidal interactions by lipid-plus-CTB functionalization. By altering the concentration of

CTB bound on microparticles, attractive interaction energies can be modulated in a range of $1k_BT$. Our demonstration of tunable attractive pair potentials in lipid- and CTB-functionalized particles reveals a new route to controlling colloidal interactions. The difference in the behaviors observed for lipid-coated and lipid-plus-protein-coated silica microspheres shows that properties such as the attraction energy and interaction range can be controlled separately from one another. The former particles, for example, show ΔU decreasing with $\langle r \rangle$ whereas the latter show the opposite behavior. The ability to influence particular aspects of interactions will be useful in many important contexts, for example, in controlling colloidal crystallization.

More fundamentally, we provide quantitative measurements of a well-defined colloidal system that we hope will motivate deeper insights into the long-standing mystery of like-charge attraction in weak monovalent electrolytes. Unfortunately, we cannot at present solve this mystery. In fact, our results show that a solution may be more complex than has been previously suspected. Differently functionalized particles show radically different interaction properties. The separation distance between particles and the confining wall, although important, is not a simple determinant of attractive interaction strength. We note that CTB functionalization should alter the characteristics of the particles other than surface charge density, such as roughness, membrane fluidity [122] and local ion concentration that we

suspect alter interparticle and particle-wall interactions in ways that transcend simple mean-field theories.

CHAPTER VII

MODULATIONS OF ATTRACTIVE COLLOIDAL INTERACTIONS BY LIPID FUNCTIONALIZED SILICA MICROPARTICLES AND GLASS CHAMBER BOTTOM

7.1 Introduction

In chapter V, analysis of modulated pair potentials reveals that there is a linear relationship between pair potential $U(r)$ and molar percentage of positively charged lipids Z_{lipid} at each separation r. From DLVO theory (Eq.(3.13)), we would expect that $U(r)$ should be quadratically proportional to Z_{lipid}, $U \sim Z_{lipid}^2$. However, the linear relationship between $U(r)$ and Z_{lipid} indicates that particle-wall interaction may dominate pair colloidal interaction measurements since the charge density of the glass chamber bottom is constant C, and the linear relationship can be explained by $U \sim Z_{lipid} \cdot C$. Our data show that it is necessary to characterize the dependence of pair colloidal interaction on the charge density of chamber wall.

In Chapter VI, we demonstrated that relationships between the magnitude of

attractive potential and particle-wall separation are oppositely different between lipid-only and lipid-plus-CTB functionalized silica microparticles. Our data indicate that particle-wall separation cannot be the only determinant of confinement-induced like-charge attraction. But we still need to emphasize that the presence of wall is important to the generation of like-charge attraction, because early studies [16] have shown that such mysterious attraction did not appear in isolated colloidal system. Moreover, in our experiments, for both lipid-only and lipid-plus-CTB functionalized silica microspheres, the magnitudes of attractive pair interaction energy ΔU is very sensitive to mean particle-wall separation $\langle h \rangle$. ΔU can be modulated in a range of $1k_BT$ by the change of $\langle h \rangle$ in 200 nm. However, the oppositely different modulation relations $\Delta U \sim \langle h \rangle$ indicate that the modulation of like-charge attraction by confining wall is more complicated than has been previously thought. Characterization of particle-wall separation is not enough to understand confining wall modulated colloidal attractions. Therefore, we need to open a new avenue to further characterize the effect of confining wall on like-charge attraction.

The electrostatic properties of the glass chamber bottom can be modified in a similar way as those of colloidal particles. In an electrolyte solution, the surface of wall is normally negatively charged due to the dissociation of silanol groups. The particle-wall separation is mainly due to the long range electrostatic repulsion between particle and wall. Therefore, it is also possible to modulate particle-wall interaction by the modification of the electrostatic properties (e.g. charge density) of glass chamber wall.

Such active modifications may facilitate to understand the function of the confining-wall on like-charge attraction. One such examples has been reported by Polin.et.al [20]: mysterious attraction between silica microparticles appears near the vicinity of the glass chamber bottom, whereas, pair colloidal interaction is purely repulsive under the confinement of gold coated chamber bottom which is almost uncharged. They proposed a phenomenological form to explain the wall-charge-dependent like-charge attraction, which suggested that the magnitude of attractive potential is linearly proportional to the charge density of chamber wall. Moreover, because the lack of charge on confining surface will decrease particle-wall separation, the resulting purely repulsive interaction with gold coated surface seems contradictory with experimental results obtained by Larsen et.al [16], in which like-charge attraction only appears in a short particle-wall separation.

The lipid bilayer is also a good candidate to modify the electrostatic property of the planar substrate. Unlike gold coatings, lipid bilayers can self-assemble on the surface of planar glass surface to form uniform membrane coatings, and the charge density of glass chamber bottom can be easily tuned by lipid compositions. Recent studies [123] on many body colloidal systems, in which, lipid bilayers with the same composition functionalized both colloidal particles and the glass chamber bottom, revealed that the magnitude of like-charge attraction depends on the overall charge signs of particle and chamber bottom. Particles above the chamber wall, both of which were coated with negatively charged lipid bilayers, exhibited stronger

like-charge attraction than those coated with positively charged lipid bilayers. Even though the underlying modulation mechanism is not clear, at least it demonstrated that lipid bilayers can be used to modulate the electrostatic property of glass chamber bottom, and hence enable us to characterize the effect of particle-wall interaction on pair colloidal interactions. In this chapter, we will introduce pair interaction measurements of lipid functionalized silica particles above lipid functionalized glass chamber walls, as well as the measurements of mean particle-wall separations. The net amounts of negative charge on both particle and chamber wall were modulated by the composition of coated lipid bilayers, which is similar as those used in pair interaction measurements introduced in Chapter V. The data show that the control of the magnitude and range of attractive interparticle interactions can be achieved by modulating charge densities of confining wall. However, the modulation mechanism in this case is different from the situation in which only the particles were functionalized with lipid bilayers. Our results demonstrate that confining wall plays an important role in generating like-charge attraction.

7.2 Experimental Methods

Since most materials and experimental methods used are similar to those described in experimental methods sections in Chapter V and IV, in this section we will only focus on methods which were not introduced before.

Chamber

The chamber holder was made by two pieces of PolyChloroTriFluoroEthylene (KEL-F PCTFE), KEL-F PCTFE is a kind of plastic with a high chemical resistance and a high compression, impact and tensile strength. A coverslip was put at the bottom of lower part of chamber holder, then the upper part of chamber holder was inserted on the top of the lower part. The coverslip was then sealed by a viton O-ring on its top and tightened by plastic screws connecting upper and lower parts of chamber holder to prevent any leakages of solution. The clear aperture of the chamber on the microscope is about 10mm in diameter. The No.1.0 borosilicate coverslip attached at the bottom of homemade chamber has similar electrostatic properties as the coverglass bottom of 8-well chambers (Lab-Tek, Nalge Nunc International) used in previous experiments. RICM measurments show that the difference of mean particle-wall separations for 3.2 μm diameter silica particles above these two kinds of coverslips in DI water was about 50 nm. Therefore, the effect of change of glass chamber bottom on pair interaction measurements can be neglected.

Lipids

Lipids used in experiments are the same as those described in the experimental method section of Chapter V, which include 1,2-dioleoyl-sn-glycero-3-phosphocholine (DOPC), 1,2-diachyl-sn-glycero-3-phosphoserine (DOPS), 1,2-dioleoyl-3-trimethylammonium-propane (DOTAP) and fluorophore-conjugated lipid Texas Red 1,2-dihexadecanoyl-sn-glycero-3-phosphoethanolamine (Texas Red

DHPE). Texas Red DHPE is anionic, contributing to the Z_{lipid} values stated in the text.

Supported Lipid Bilayers on Glass Coverslips

Supported lipid bilayers were formed on 25mm diameter circular coverslips, which are made from NO.1.0 boroslicate glass. Coverslips were cleaned by piranha solution before use. To facilitate the rupture of Small unilamellar vesicles (SUVs) on the glass surface, smaller SUVs (30nm in diameter) with desired compositions were made following the procedure introduced in Chapter V. A spreading solution was prepared by mixing 1 : 5 SUVs : 1X PBS buffer in an eppendorf tube. Then, 50 μl spreading solution was pipetted in the center of the top of culture dish (Falcon, 35 mm in diameter). A clean coverslip was held by a tweezer at a 45° angle with one edge touching the dish, over the drop of spreading solution but not touching it. The coverslip then was dropped quickly to ensure no bubbles trapped in the thin layer of spreading solution between coverslip and dish. After 15 minutes incubation in dark, the coverslip together with the dish was placed into a large beaker of distilled water. Unruptured SUVs were removed by picking up the coverslip and agitating it underwater for about 10 seconds. This process can be repeated several times if necessary. Finally, the coverslip was mounted on the chamber holder underwater. To further make sure that all unruptured SUVs were gone, the water inside the chamber can be exchanged with deionized water (Millipore). Note that supported lipid bilayer should be never exposed to air.

Other Methods

Preparations of SUVs and lipid functinoalized silica particles, particle tracking and measurements of pair interaction energies and particle-wall separations were performed and described in previous chapters.

7.3 Experimental Results

Single, continuous lipid bilayers readily self-assemble on surfaces of both silica particles and glass chamber bottoms using established techniques. Membrane coatings consisted primarily of zwitterionic (neutral) lipids DOPC, with 0.5 mol% of the anionic fluorescent probe Texas Red DHPE and various fractions of the acidic lipid DOPS or the cationic DOTAP. Membranes with net molar percentages of positively charged lipids, Z_{lipid}, between -4 and +4 were examined. Overall, both particle and confining wall were negatively charged with the negative charge density modulated by membrane coatings. Fluorescence microscopy revealed uniformly membrane coatings on both silica microspheres and glass chamber bottom, and the fluidity of supported lipid bilayers on the glass chamber bottom was examined by fluorescence recovery after photobleaching (FRAP), which was introduced in Chapter I.

Dilute lipid functionalized silica microsphere suspensions were pipetted into the chambers containing DI water. 3.2 μm diameter silica particles were sedimented by gravity near the vicinity of the lipid functionalized glass chamber bottom. Random

particle pairs were trapped in a line optical trap and pair interaction energies $U(r)$s were measured (Fig.7.1(a)). At least 5 measurements were performed for each combination of membrane compositions on the particles and chamber wall.

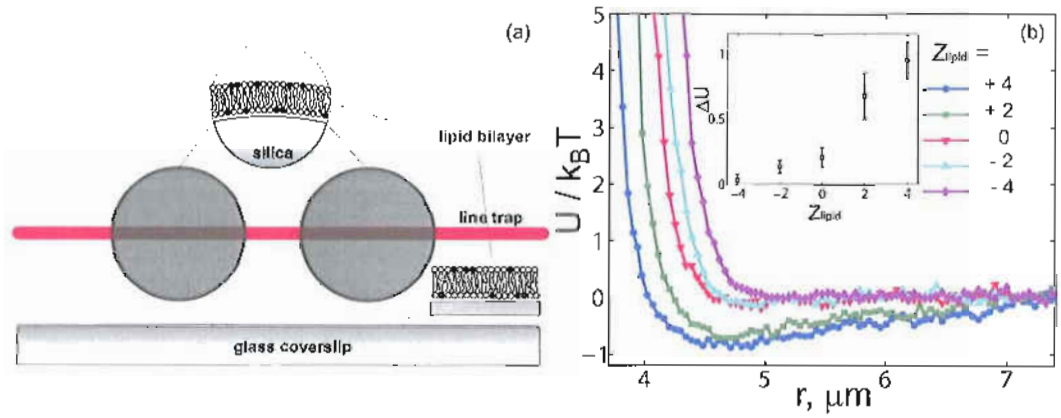

FIGURE 7.1: (a) A schematic diagram of pair interaction measurements. (b) Representative pair interaction energies, $U(r)$, versus center-to-center particle separation, r, varying with Z_{lipid}. $U(r)$s were measured for 3.2 μm diameter silica particles above the glass chamber bottom. Both the particles and the chamber bottoms were functionalized with lipids of the same composition. Inset: Attractive well depth, ΔU, versus Z_{lipid} (points). The gray line is a quadratic fitting.

For the case in which both silica microspheres and the chamber bottom were functionalized with membranes of the same composition, the data show that colloidal pair interaction energies, especially attractive interaction energies, can be modulated by altering lipid compositions (Fig.7.1(b)). At low interparticle separations, all potential curves are almost parallel with each other which indicates a similar electrostatic repulsion screening length independent of membrane compositions. Particles coated with negative or neutral lipids ($Z_{lipid} \leq 0$) exhibit very weak attractive ($\leq 0.1 k_B T$) or purely repulsive pair interaction. Particles with positive

charged membranes ($Z_{lipid} > 0$) show strong attractive minima in $U(r)$, the strongest attractive colloidal pair interaction appears for membranes with $Z_{lipid} = +4$ (4.5 mol% DOTAP). Studies [117] on planar supported lipid bilayers have shown that membranes with $Z_{lipid} = +4$ almost neutralize the negative charges of underlying silica. Therefore, both particles and chamber bottom coated with membranes consisting of more than 4.5 mol% DOTAP should be positively charged. Colloidal pair interactions in this condition are not discussed in this chapter. Instead of a linear relationship between the depth of attractive well, ΔU and Z_{lipid}, which we obtained from the pair potential measurements of lipid functionalized silica microspheres above a bare glass chamber bottom, ΔU varies quadratically with Z_{lipid} for membranes of the same composition functionalized on glass chamber bottom as well (Fig.7.1(b)inset).

Further, we picked two membrane compositions, $Z_{lipid} = -4$ (3.5 mol% DOPS) and $Z_{lipid} = +2$ (2.5 mol% DOTAP) to differently functionalize silica microspheres and the glass chamber bottom ($Z_{lipid} = -4$ on glass chamber bottom, $Z_{lipid} = +2$ on silica particles or vice versa), and measured pair potentials of lipid functionalized silica particles. Combined with the data obtained above, the results showed that attractive colloidal pair interactions can be modulated by altering lipid compositions on glass chamber bottom. For particles coated with highly negatively charged membranes($Z_{lipid} = -4$), pair potentials are always purely repulsive no matter whether the chamber bottom was highly($Z_{lipid} = -4$)or weakly($Z_{lipid} = +2$)

negatively charged (Fig.7.2(a)). However, particles with membranes of $Z_{lipid} = +2$ exhibit much stronger attractive pair interaction energy above chamber bottom coated with membranes of $Z_{lipid} = +2$ than that of $Z_{lipid} = -4$ (Fig.7.2(b)).

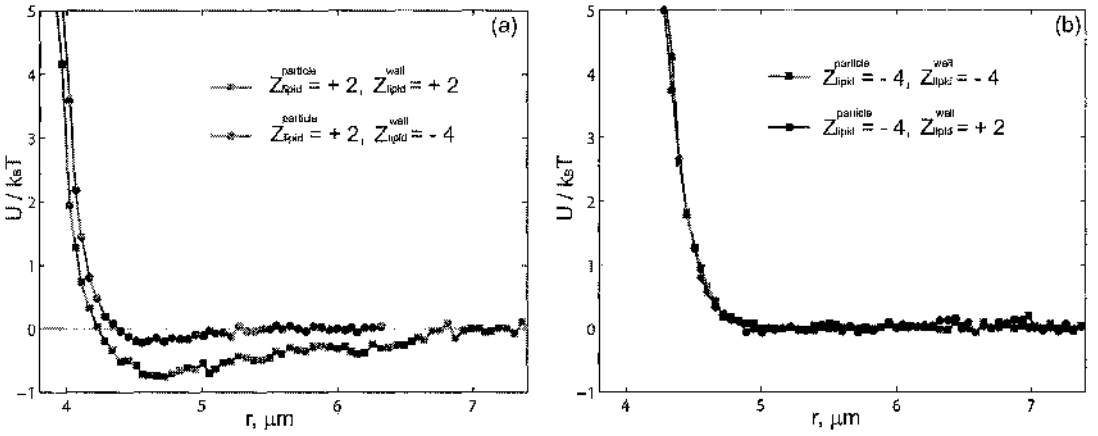

FIGURE 7.2: Comparisons of representative pair interaction energies,$U(r)$ for lipid functionalized silica microspheres above lipid functionalized glass chamber wall. Silica particles and the glass chamber walls were coated with lipid bilayer of the same or different compositions (Z_{lipid}). (a) $Z_{lipid}^{particle} = +2$ with $Z_{lipid}^{wall} = +2$ and -4.(b) $Z_{lipid}^{particle} = -4$ with $Z_{lipid}^{wall} = +2$ and -4.

The mean particle-wall separations $\langle h \rangle$ were measured by the method introduced in Chapter IV for each combination of lipid compositions on silica microspheres and chamber bottom. As is shown in Fig 7.3, the more neutral the same membrane functionalization (overall less negatively charged) on both particle and chamber wall, the shorter the particle-wall separation is. There is a roughly linear relationship between $\langle h \rangle$ and Z_{lipid}. From $Z_{lipid} = -4$ to $Z_{lipid} = +4$, the range of $\langle h \rangle$ is about 400 nm, which is larger than that we measured with lipid functionalized particle above a glass chamber bottom.

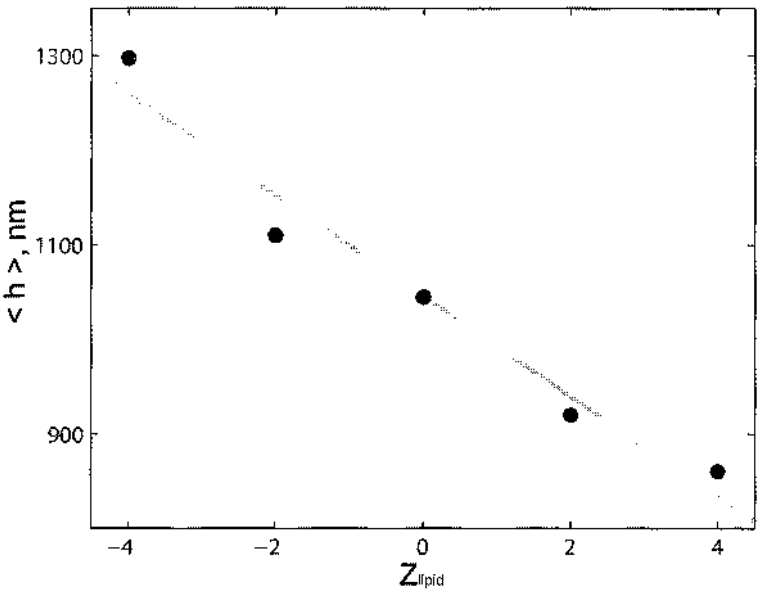

FIGURE 7.3: Mean heights $\langle h \rangle$ of lipid functionalized silica microspheres above lipid functionalized glass chamber bottom. Both of them were functionalized with lipid bilayer of the same composition.

7.4 Discussion and Analysis

Pair interaction measurements of lipid functionalized silica microspheres above lipid functionalized glass chamber bottoms were performed with a homemade chamber system with NO.1.0 borosilicate coverslip. 8-well chambers with NO.1.0 borosilicate coverglass bottoms (Lab-Tek, Nalge Nunc International) used in previous experiments were not employed in this case. Unruptured SUVs can be trapped in the sealing gaps of the 8-well chambers and hard to flush out, which will change the Debye screening length of the solution inside the chamber.

For lipid functionalized particle above bare glass chamber bottom, previous experiments have shown that followed by increasing the amount of positively charged

lipids coated on particle, particle become closer to the chamber wall and attractive colloidal pair interactions become stronger. There is a linear relationship (positive slope) between the depth of attractive potential well, ΔU and Z_{lipid}. For both silica particles and glass chamber bottom functionalized with lipids of the same composition, particles with less negatively charged membrane exhibit stronger attractive colloidal pair interactions. The closer the particle is to the chamber bottom, the stronger the attractive pair potential is. These two fundamental trends are consistent in both cases of functionalizations. However, the relationship between ΔU and Z_{lipid} is not linear when both surfaces are functionalized. When both particle and lipid were functionalized with neutral or negatively charged lipids ($Z_{lipid} \lesssim 0$), colloidal pair interactions are purely repulsive or very weakly attractive ($\Delta U \leq 0.1 k_B T$) in a long range. Obvious attractive minima appear in $U(r)$ for positively charged lipids functionalization. For the same lipid composition, the magnitudes of ΔU is comparable to that measured in the case of particle functionalized only. On the whole, ΔU varies quadratically with Z_{lipid}. Compared with previous experimental setup, the only difference introduced here is the functionalization of lipid membranes on glass chamber bottom, which mainly modifies the electrostatic properties (i.e. charge density) of confining coverslip. The different $\Delta U \sim Z_{lipid}$ obtained in this experiment indicates that confinement-induced like-charge attraction can be modulated by altering the electrostatic property of confining wall.

For particles with $Z_{lipid} = 2$, attractive colloidal pair potential is stronger when they are above a chamber wall with $Z_{lipid} = 2$ than with $Z_{lipid} = -4$. This is another indication of modulation of like-charge attraction by confining wall, in which, ΔU dramatically decrease by varying the chamber wall from slightly ($Z_{lipid} = 2$) to highly ($Z_{lipid} = -4$) negatively charged. Separations between particle with $Z_{lipid} = 2$ and chamber wall with $Z_{lipid} = -4$ or vice versa are similar as that with ($Z_{lipid} = 0$) for both particle and wall. Correspondingly, all three $U(r)$s only contain very weakly attractive minima ($\Delta U \leq 0.2 k_B T$) or purely repulsive. Obvious attractive interactions between lipid functionalized silica particles in DI water only appear when particle-wall separation is less than 1μm. Compared with the results reported in Ref[20] in which highly charged chamber bottom yields like-charge attractions, our data show opposite relationship between ΔU and $\langle h \rangle$. The weaker the electrostatic repulsion between particle and chamber wall is, the closer the particle is to the chamber wall, and the stronger the like-charge attraction is.

7.5 Summary

In this chapter, we extend our experiments introduced in Chapter V by additionally functionalizing lipid membranes on glass chamber bottom. The resulting modified electrostatic properties of chamber wall have experimentally demonstrated its ability to modulate attractive colloidal pair interactions. For the case in which both particles and chamber wall were functionalized with lipid

membranes of the same composition, the depth of attractive colloidal pair potential ΔU varies quadratically with Z_{lipid}. Moreover, for particles with $Z_{lipid} = 2$, ΔU can be decreased by varying the chamber bottom from slightly to highly negatively charged. Our data also show the dependence of ΔU on mean particle-wall separation $\langle h \rangle$, particles closer to the chamber bottom exhibit stronger attractive colloidal pair interaction, which is consistent with the results obtained in Chapter V.

CHAPTER VIII

CONCLUSIONS AND FUTURE DIRECTIONS

In this final chapter, we first conclude the dissertation with a summary of our experimental accomplishments. Then, we give an outlook for possible future research directions on the mechanism of like-charge attraction modulated by lipid membranes and the application to generate colloidal self-assembly.

8.1 Conclusions

To accomplish the research presented in this dissertation, we first generated line traps via a new holographic optical tweezers (HOTs) technique. By incorporating phasemasks of line traps with Gaussian intensity distributions on a spatial light modulator (SLM), the intensity along the trap can be tuned to balance gradient and scattering forces exerted on trapped particles. Line traps with tunable Gaussian intensity distributions [55] can make particle almost freely diffuse in one dimension, which makes it possible to characterize colloidal pair interaction energy via a Boltzmann relationship. As a demonstration of our line trap design and our methods to measure colloidal pair interactions, pair potential of bare silica microparticles near the vicinity of a glass chamber bottom were measured, and the data show that the

pair potential of silica microsphere is purely repulsive and in agreement with DLVO theory [56].

Confinement-induced like-charge attraction has received much attention since 1994 [15]. However, it is still an unsolved puzzle in colloidal science nowadays due to the lack of tunable, attractive long-range interparticle interactions. Furthermore, the modification of intrinsic electrostatic properties of colloidal particles and walls has been largely ignored as a route to investigate this topic. In this dissertation, we recruited lipids and proteins to functionalize silica microspheres and chamber bottoms to modify their electrostatic properties. By varying the type and amount of charged lipids in the lipid composition, charge densities of particle and chamber bottom can be easily modulated, and protein incorporated in the lipid membrane can provide additional functionalization.

We measured the pair interaction of lipid and protein functionalized silica microspheres in three cases : lipid-only functionalized particles above bare glass chamber bottoms, lipid-plus-protein functionalized particles above bare glass chamber bottoms and lipid functionalized particles above lipid functionalized glass chamber bottoms. For each case, the data show tunable, long-range attractive pair interactions. Compared with previous studies, first, the results presented in this dissertation illuminates the control of confinement-induced like-charge attraction, instead of simply observing the appearance of such mysterious attraction. Second,

we also compared the attractive colloidal interactions obtained from each case, and provide insights into the mechanism of like-charge attraction.

Our Major Experimental Findings are as follows

1. We measured the pair interaction energies of lipid functionalized silica microspheres above bare glass chamber bottoms. Varying the molar percentage of positively charged lipid, Z_{lipid}, the depth of attractive colloidal pair potential well, ΔU, can be modulated in a range of approximately $1k_BT$. The relationship between $U(r)$ and Z_{lipid} yields the separation of $U(r)$ into charge-related term, which is purely repulsive, and a term not directly related to charge. The linear relationship between $U(r)$ and Z_{lipid} indicates that the pair potentials of lipid functionalized silica microspheres are mediated by the chamber wall nearby. Our data provide the first ever characterization of the charge dependence of like-charge colloidal attraction.

2. We measured the pair potentials of lipid-plus-protein functionalized silica microspheres near the vicinity of glass chamber bottom. Attractive colloidal pair interaction energies can also be tuned in a range of $1k_BT$ followed by varying the concentration of cholera toxin subunit B (CTB) bound on the surface of lipid functionalized silica microspheres containing the lipid ligand monosialogangsolioside G_{M1}. The relationship between $U(r)$ and incubation concentration of CTB, [CTB], also allow us to separate $U(r)$ into CTB-related

term, which is repulsive, and a membrane-related term. Moreover, from potential curve analysis and mean particle-wall separation measurements, we found that the mechanisms of like-charge attraction modulation are different between lipid-only and lipid-plus-CTB functionalized silica microspheres. This indicates that the situation of like-charge attraction is more complicated than previously thought, and there are probably more than one mechanism to account for like-charge attraction.

3. To quantify the effect of the chamber wall on like-charge attraction, we functionalized the glass chamber bottom with lipid bilayers, and measure pair potentials of lipid functionalized silica microspheres above it. For both particles and wall functionalized with lipids of the same composition, attractive colloidal interactions become stronger following the increase of Z_{lipid}. However, unlike the case of only particles being functionalized, ΔU varies quadratically with Z_{lipid}. Moreover, varying the composition of lipid functionalized on the chamber bottom, ΔU between particles changes dramatically. These results quantify the way that like-charge attraction can be controlled by the electrostatic properties of confining wall.

8.2 Future Directions

In this dissertation, the center-to-center separation r between two particles along the line trap was sampled for a period, then colloidal pair interaction energy

was calculated from the probability distribution of separations $P(r)$ according to Boltzmann relationship (Eq.3.1). However, short separations between two particles cannot be sampled due to the strong electrostatic repulsion. Therefore, pair potential profile cannot be reconstructed in the whole interaction range between particles, especially in the range of short separations. 'Blinking' optical traps [87, 88] can be used to characterize such short-range interactions. Depending on the laser power, two particles can be stably trapped by two point optical traps close to each other. By repeating turning on and off the optical traps, pair interaction energy $U(r)$ can be characterized for each initial trap separation r. The drawback of 'blinking' traps is that they are time-consuming, and measurements need to be intensively performed for different separations. However, for future research, it is worth measuring colloidal pair interaction using 'blinking' traps, because first, it can provide short-range pair colloidal interaction energy measurements which cannot be done by line traps; and second, we can compare the precisions offered by 'blinking' traps and line traps in colloidal pair interaction measurements.

For functionalized silica microspheres, the coated lipid bilayers not only change the electrostatic properties (i.e. charge density) of particle surface, but also its fluidity. Unlike the charge originally on the surface of silica, the charged lipids can flow around the surface. Such charge mobility can lead to inhomogeneous charge distributions around particle surface and hence the inhomogeneous distribution of counterions around the particle. Such inhomogeneities can also depend on the

particle-particle or particle-wall separations. Therefore, it is worth investigating the effect of membrane mobility on like-charge attraction. First, we can try to use lipid monolayers to functionalize particles and measure colloidal pair interactions. The coated lipid monolayers is not fluidic around the surface of particle. Or second, we can use lipids with saturated carbon chains to functionalize particles. Because the critical temperature of such lipids is around room temperature, it will be easy to decrease their mobility by lowering the temperature to trigger phase transitions. We can measure pair potential interaction energies when the coating membrane is in an ordered as well as a disordered state (solid-like as well as fluid-like). Both methods can decrease the mobility of membrane, and hence the measured pair potential will show the relevance of membrane fluidity on like-charge attraction. On the theoretical side, some studies [118] have shown that charge inhomogeneity can lead to attractive colloidal interactions. However, such theories can only be applied in the situation of short separations(nm range) between particles, and it may worth expanding such theoretical approaches to account for long-range attractive colloidal interactions.

Many body interactions play an important role in generating colloidal self-assembly. From colloidal pair interaction measurements, we can step by step increase the number of particles and measure interparticle interactions. Some studies [124] have shown strong changes in colloidal pair interactions in the presence of the third particle. Using 'blinking' traps, we can easily set a symmetric initial state for many

particles (i.e. equilateral triangle, square,..) and measure the resulting interaction energies.

BIBLIOGRAPHY

[1] J.K.G.Dhont, *An Introduction to Dynamics of Colloids* (Elsevier, Amsterdam, 1996).

[2] J.Lyklema, *Fundamental of Interfaces and Colloids Science* (Academic Press, London, 1991).

[3] S.Suresh, "Crystal deformation : Colloid model for atoms," Nat.Mater. **5**, 253–254 (2006).

[4] D.Babič, C.Schmitt, and C.Bechinger, "Colloids as model systems for problems in statistical physics," Chaos **15**, 026 114 (2005).

[5] E.R.Weeks and D.A.Weitz, "Properties of cage rearrangement observed near the colloidal glass transition," Phys. Rev. Lett. **89**, 095 704 (2002).

[6] A.D.Dinsmore, V.Prasad, I.V.Wong, and D.A.Weitz, "Microscopic Structure and Elasticity of Weakly Aggregated Colloidal Gels," Phys. Rev. Lett. **96**, 185 502 (2006).

[7] R. J. Hunter, *Introduction to Modern Colloid Science* (Oxford University Press Inc., New York, 1993).

[8] H.Siedentopf and R.Zisigmondy, "Ueber Sichtbarmachung und Grössenbestimmung ultramikroscopischen Teilchen, u.s.w," Ann. Physik. **10**, 1- 39 (1903).

[9] J.D.Joannopoulos, P.R.Villeneuve, and S.Fan, "Photonic crystals : putting a new twist on light," Nature **386**, 143–149 (1997).

[10] Y.A.Vlasov, X.Bo, J.C.Sturm, and D.J.Norris, "On Chip natural assembly of silicon photonic bandgap crystals," Nature **414**, 289–293 (2001).

[11] F.Meseguer, "Colloidal crystals as photonic crystals," colloids.surf. **270**, 1–7 (2005).

[12] R.K.Iler, *The Chemistry of Silica* (Wiley, New York, 1979).

[13] B.V.Derjaguin and L. Laudau, "Theory of stability of highly charged liophobic sols and adhesion of highly charged particles in solutions of electrolyte," Acta.Physicochim.URSS **14**, 633 (1941).

[14] E.J.Verwey and J.T.G.Overbeek, *Theory of the stability of lyophobic colloids* (Elsevier, Amsterdam, 1948).

[15] G.M.Kepler and S.Fraden, "Attractive potential between confined colloids at low ionic strength," Phys. Rev. Lett. **73**, 356–359 (1994).

[16] A.E.Larsen and D.G.Grier, "Like-charge attractions in metastable colloidal crystallites," Nature **385**, 230–233 (1997).

[17] Y.Han and D.G.Grier, "Confinement-induced colloidal attractions in equilibrium," Phys. Rev. Lett. **91**, 038 302 (2003).

[18] J.C.Butler, T.Angelini, J.X.Tang, and G.C.L.Wong, "Ion multivalence and like-charge polyelectrolyte attraction," Phys. Rev. Lett. **91**, 028 301 (2003).

[19] T.E.Angelini, H.Liang, W.Wriggers, and G.C.L.Wong, "Like-charge attraction between polyelectrolytes induced by counterion charge density waves," Proc.Natl.Acad.Sci.USA. **91**, 028 301 (2003).

[20] M.Polin, D.G.Grier, and Y.Han, "Colloidal electrostatic interactions near a conducting surface," Phys. Rev. E **76**, 041 406 (2007).

[21] J.C.Crocker and D.G.Grier, "When like charges attract:the effects of geometrical confinement on long-range colloidal interactions," Phys. Rev. Lett. **77**, 1897–1900 (1996).

[22] T.M.Squire and M.P.Brenner, "Like-charge attraction and hydrodynamic interaction," Phys. Rev. Lett. **85**, 4976–4979 (2000).

[23] R. Roij and J.P.Hansen, "Van der Waals-like instability in suspensions of mutually repelling charged colloids," Phys. Rev. Lett. **79**, 3082–3085 (1997).

[24] D.G.Grier and Y.Han, "Anomalous attractions in confined charge-stabilized colloid," J.Phys.:Condensed.matter **16**, S4145–4157 (2004).

[25] S.J.Singer and G.L.Nicolson, "The fluid mosaic model of the structure of cell membrane," Science **175**, 720–731 (1972).

[26] L.K.Tamm, "The substrate supported lipid bilayer - a new model membrane system," Klin.Wochenschr. **62**, 502–503 (1984).

[27] L.K.Tamm and H.M.McConnell, "Supported phospholipid bilayers," Biophys.J. **47**, 105–113 (1985).

[28] H.M.McConnell, T.H.Watts, R.M.Weis, and A.A.Brain, "Supported planar membranes in studies of cell-cell recognition in the immune system," Biochim.Biophys.Acta **864**, 95–106 (1986).

[29] T.H.Watts and H.M.McConnell, "Biophysical aspects of antigen recognition by T cells," Annu.Rev.Immunol. **5**, 461–475 (1987).

[30] B.C.Lagerholm, T.E.Starr, Z.N.Volovyk, and N.L.Thompson, "Rebinding of IgE Fabs at haptenated planar membranes: measurement by total internal reflection with fluorescence photobleaching recovery," Biochemistry. **39**, 2042–2051 (2000).

[31] J.A.Zasadzinski, C.A.Helm, M.L.Longo, A.L.Weisenhorn, S.A.Gould, and P.K.Hansma, "Atomic force microscopy of hydrated phosphatidylethanolamine bilayers," Biophys.J. **59**, 755-760 (1991).

[32] H.Egawa and K.Furusawa, "Liposome adhesion on mica surface studied by atomic force microscopy," Langmuir. **15**, 1660–1666 (1999).

[33] P.S.Cremer and S.G.Boxer, "Formation and spreading of lipid bilayer on planar glass supports," J.Phys.Chem.B **103**, 2554–2559 (1999).

[34] V.P.Delrouyre, J.M.Laval, and C.Bourdillon, "Formation of steptavidin-supported lipid bilayers on porous anodic alumina : electrochemical monitoring of triggered vesicle fusion," J.Am.Chem.Soc. **123**, 9176–9177 (2001).

[35] L.K.Tamm, "Polymer-supported membranes as models of the cell surface," Nature **437**, 656–663 (2005).

[36] E.Sackmann and M.Tanaka, "Supported membranes on soft polymer cushions: Fabrication, Characterization and applications," Trends.Biotechnol. **18**, 58–64 (2000).

[37] R.P.Richter, R.Brat, and A.R.Brisson, "Formation of solid-supported lipid bilayers : an integrated view," Langmuir. **22**, 3497–3505 (2006).

[38] R.P.Richter, A.Mukhopadhyay, and A.R.Brisson, "Pathways of lipid vesicle deposition on solid surfaces : A combined QCM-D and AFM study," Biophys.J. **85**, 3035–3047 (2003).

[39] D.Axelrod, D.E.Koppel, J.Schlessinger, E.Elson, and W.W.Webb, "Mobility measurement by analysis of fluorescence photobleaching recovery kinetics," Biophys.J. **16**, 1055–1069 (1976).

[40] J.M.Crane, V.Kiessling, and L.K.Tamm, "Measuring lipid asymmetry in planar supported bilyers by fluorecence interference contrast microscopy," Langmuir. **21**, 1377–1388 (2005).

[41] R.P.Richter and A.R.Brisson, "Following the formation of supported lipid bilayer on mica : a study combining AFM, QCM-D and Ellipsometry," Biophys.J. **88**, 3422–3433 (2005).

[42] E.Kalb, J.Engel, and L.K.Tamm, "Binding of proteins to specific target sites in membranes measured by total internal reflection fluorescence microscopy," Biochemistry. **29**, 1607–1613 (1990).

[43] N.L.Thompson, K.H.Pearce, and H.V.Hsieh, "Total internal reflection fluorescence microscopy : application to substrate-supported planar membranes," Eur.Biophys.J. **22**, 367–378 (1993).

[44] M.Merzlyakov, E.Li, and K.Hristova, "Directed assembly of surface-supported bilayers with transmembrane helices," Langmuir. **22**, 1247–1253 (2006).

[45] P.Hinterdorfer, G.Baber, and L.K.Tamm, "Reconstitution of membrane fusion sites: A total internal reflection fluorescence microscopy study of influenza hemagglutinin-mediated membrane fusion," J.Biol.Chem. **269**, 20360–20368 (1994).

[46] V.Kiessling, "Imaging fast SNARE mediated-membrane fusion in planar-supported bilayers," Biophys.J. **89**, 2185–2186 (2005).

[47] A.A.Brian and H.M.McConnell, "Allogeneic stimulation of cytotoxic T cells by supported planar membranes," Proc.Natl.Acad.Sci.U.S.A. **81**, 6159–6163 (1984).

[48] H.Wu, T.O.Pangburn, R.E.Beckham, and M.A.Bevan, "Measurement and interpretation of particle-particle and particle-wall interactions in levitated colloidal ensembles," Langmuir. **21**, 9879–9888 (2005).

[49] H.M.Reinl and T.M.Bayerl, "Lipid transfer between small unilamellar vesicles and single bilayer on solid support : self-assembly of supported bilayers with asymmetric lipid distribution," Biochemistry. **33**, 14091–14099 (1994).

[50] J.Schmitt, B.Danner, and T.M.Bayerl, "Polymer cushions in supported phospholipid bilayers reduce significantly the frictional drag between bilayer and solid surface," Langmuir. **17**, 244–246 (2001).

[51] A.Ma and Z.Rosenzweig, "Systhesis and analytical properties of micrometric biosensing lipobeads," Anal.Bioanal.Chem. **382**, 28–36 (2005).

[52] A.L.Stahlhofen, A.Eckert, T.Hartmann, and M.Schöttner, "Solid-supported lipid membranes as a tool for determination of membrane affinity : high-throughput screening of physicochemical parameter," J.Pharm.Sci. **90**, 599–606 (2001).

[53] M.M.Baksh, M.Jaros, and J.T.Grove, "Detection of molecular interactions at membrane surfaces through colloid phase transitions," Nature **427**, 139–141 (2004).

[54] E.M.Winter and J.T.Grove, "Surface binding affinity measurements from order transitions of lipid membrane-coated colloidal particles," Anal.Chem. **78**, 174–180 (2006).

[55] G.T.tietjen, Y.Kong, and R.Parthasarathy, "An efficient method for the creation of tunable optical line traps via control of gradient and scattering force," Opt.Express. **16**, 10341–10348 (2008).

[56] Y.Kong and R.Parthasarathy, "Modulation of attractive colloidal interactions by lipid membrane functionalization," Soft Matter. **5**, 2027–2029 (2009).

[57] Y.Kong and R.Parthasarathy, "Different modulation mechanisms of attractive colloidal interactions by lipid and protein functionalization," Langmuir. **26**, 10541–10545 (2010).

[58] A.Ashkin, "Acceleration and trapping of particles by radiation pressure," Phys. Rev. Lett. **24**, 156–159 (1970).

[59] A.Ashkin and J.M.Dziedzic, "Optical levitation by radiation pressure," Appl.Phys.Lett. **19**, 283–285 (1971).

[60] A.Ashkin, J.M.Dziedzic, J.E.Bjorkholm, and S.Chu, "Observation of a single-beam gradient force optical trap for dielectric particles," Opt.Lett. **11**, 288–290 (1986).

[61] A.Ashkin and J.M.Dziedzic, "Optical trapping and manipulation of viruses and bacteria," Science **235**, 1517–1520 (1987).

[62] D. S.M.Block and H.C.Berg, "Compliance of bacterial flagella measured with optical tweezers," Nature **338**, 514–518 (1989).

[63] A.Ashkin and J.M.Dziedzic, "Internal cell manipulation using infrared laser traps," Proc.Natl.Acad.Sci.USA. **86**, 7914–7918 (1989).

[64] R.W.Steubing, S.Cheng, W.H.Wright, Y.Numajiri, and M.W.Berns, "Laser induced cell fusion in combination with optical tweezers : the laser cell fusion trap," Cytometry. **12**, 505–510 (1991).

[65] K.Svoboda, C.F.Schmidt, B.J.Schnapp, and S.M.Block, "Direct observation of kinesin stepping by optical trapping interferometry," Nature **365**, 721–727 (1993).

[66] J.A.Stratton, *Electromagnetic theory* (McGraw-Hill, New York, 1941).

[67] M.Kerker, *The scattering of light and other electromagnetic radiation* (Academic, New York, 1969).

[68] E.Fallman and O.Axner, "Design for fully steerable dual-trap optical tweezers," Appl.Opt. **36**, 2107-2113 (1997).

[69] J.R.Moffitt, Y.R.Chemla, D.Izhaky, and C.Bustamante, "Differential detection of dual traps improves the spatial resolution of optical tweezers," Proc.Natl.Acad.Sci.USA. **103**, 9006–9011 (2006).

[70] D.L.J.Vossen, A.V.Horst, M.Dogterom, and A.V.Blaadern, "Optical tweezers and confocal microscopy for simultaneous three-demensional manipulation and imaging in concentrated colloidal dispersions," Rev.Sci.Inst. **75**, 2960–2970 (2004).

[71] J.M.R.Fournier, M.M.Burns, and J.A.Golovchenko, "Writing diffractive structures by optical trapping," Proc.SPIE **2406**, 101–111 (1995).

[72] E.R.Dufresne and D.G.Grier, "Optical tweezer arrays and optical substrates created with diffractive optics," Rev.Sci.Instrum. **69**, 1974–1977 (1998).

[73] M.Reicherter, T.Haist, E.U.Wagemann, and H.J.Tiziani, "Optical particle trapping with computer-generated holograms written on a liquid-crystal display," Opt.Lett. **24**, 608–610 (1999).

[74] J.Liesener, M.Reicherter, T.Haist, and H.J.Tiziani, "Multi-functional optical tweezers using computer-generated holograms," Opt.Commun. **185**, 77–82 (2000).

[75] J.E.Curtis, B.A.Koss, and D.G.Grier, "Dynamic holographic optical tweezers," Opt.Commun. **207**, 169–175 (2002).

[76] J.E.Curtis and D.G.Grier, "Structure of optical vortices," Phys. Rev. Lett. **90**, 133 901 (2003).

[77] J.C.Crocker and D.G.Grier, "Methods of digital video microscopy for colloidal studies," J. Colloid Interface Sci. **179**, 298–310 (1996).

[78] B.Chu, *Laser light scattering* (Academic Press, New York, 1974).

[79] W.I.Goldburg, "Dynamic light scattering," Am.J.Phys. **67**, 1152–1160 (1999).

[80] R.Z.Bar, A.Meller, T.Tlusty, E.Moses, J.Stavans, and S.A.Safran, "Localized daynamic light scattering : Probing single particle dynamics at the nanoscale," Phys. Rev. Lett. **78**, 154–157 (1997).

[81] N.Janaky and X.Liu, "Protein Interactions in Undersaturated and Supersaturated Solutions: A Study Using Light and X-Ray Scattering," Biophys.J. **84**, 523–532 (2003).

[82] G.Binnig, C.F.Quate, and C.Gerber, "Atomic force microscope," Phys. Rev. Lett. **56**, 930–933 (1986).

[83] W.A.Ducker, T.J.Senden, and R.M.Pashley, "Direct measurement of colloidal forces using an atomic foce microscope," Nature **353**, 239–241 (1991).

[84] D.C.Prieve and B.M.Alexander, "Hydrodynamic measurement of double-layer repulsion between colloidal particle and flat plate," Science **231**, 1269–1270 (1986).

[85] B.M.Alexander and D.C.Prieve, "A hydrodynamic technique for measurement of colloidal forces," Langmuir. **3**, 788–795 (1987).

[86] D.C.Prieve, "Measurement of colloidal forces with TIRM," Advan.Colloid Interface Sci. **82**, 93–125 (1999).

[87] J.C.Crocker and D.G.Grier, "Microscopic measurement of the pair interaction potential of charge-stabilized colloid," Phys. Rev. Lett. **73**, 352–355 (1994).

[88] S.K.Sainis, V.Germain, and E.R.Dufresne, "Statistics of particle trajectories at short time intervals reveal fN-scale colloidal forces," Phys. Rev. Lett. **99**, 018303 (2007).

[89] R.Verma, J.C.Crocker, T.C.Lubensky, and A.G.Yodh, "Entropic colloidal interactions in concentrated DNA solutions," Phys. Rev. Lett. **81**, 4004–4007 (1998).

[90] J.C.Crocker, J.A.Matteo, A.D.Dinsmore, and A.G.Yodh, "Entropic attraction and repulsion in binary colloids probed with a line optical tweezer," Phys. Rev. Lett. **82**, 4352–4355 (1999).

[91] P.L.Biancaniello, A.J.Kim, and J.C.Crocker, "Colloidal interactions and self-assembly using DNA hybridization," Phys. Rev. Lett. **94**, 058302 (2005).

[92] P.L.Biancaniello and J.C.Crocker, "Line optical tweezers instrument for measuring nanoscale interactions and kinetics," Rev.Sci.Instrum. **77**, 113702 (2006).

[93] Y.Roichman and D.G.Grier, "Projecting extended optical traps with shape-phase holography," Optic.Lett. **31**, 1675–1677 (2006).

[94] M.A.Golub, I.N.Sisakyan, and V.A.Soifer, "Infrared radiation focusators," Opt.Lasers.Eng. **15**, 297–309 (1991).

[95] T.Dresel, M.Beyerlein, and J.Schwider, "Design and fabrication of computer-generated beam-shaping holograms," Appl.Opt. **35**, 4615–4621 (1996).

[96] J.N.Israelachvili, *Intermolecular and Surface Forces (2nd edition)* (Academic Press, New York, 1991).

[97] L.Bergström, "Hamaker constants of inorganic materials," Advan. Colloid Interface Sci. **70**, 125–169 (1997).

[98] M.M.Burns, J.M.Fournier, and J.A.Golovchenko, "Optical binding," Phys. Rev. Lett. **63**, 1233–1236 (1989).

[99] J.Baumgartl, J.L.Arauz-Lara, and C.Bechinger, "Like-charge attraction in confinement: myth or truth?" Soft Matter **2**, 631–635 (2006).

[100] N.G.Clack and J.T.Groves, "Many-particle tracking with nanometer resolution in three dimensions by relection interference contrast microscopy," Langmuir. **21**, 6430–6435 (2005).

[101] A.S.Curtis, "The mechanism of adhesion of cells to glass : A study by interference reflection microscopy," J.Cell.Biol. **20**, 199–215 (1964).

[102] A.Albersdörfer, T.Feder, and E.Sackmann, "Adhesion-induced domain formation by interplay of long-range repulsion and short-range attraction force: a model membrane study," Biophys.J. **73**, 245–257 (1997).

[103] D.Riveline, E.Zamir, N.Q.Balaban, U.S.Schwarz, T.Ishizaki, S.Narumiya, Z.Kam, B.Geiger, and A.D.Bershadsky, "Externally applied local mechanical force induces growth of focal contacts by an mdial-dependent and rock-independent mechanism," J.Cell.Biol. **153**, 1175–1186 (2001).

[104] R.Simson, E.Wallrlaff, J.Faix, J.Niewöhner, G.Gerisch, and E.Sackmann, "Membrane bending modulus and adhesion energy of wild-type and mutant cells of dictyostelium lacking talin or cortexillins," Biophys.J. **74**, 514–522 (1998).

[105] J.O.Rädler, T.J.Feder, H.H.Strey, and E.Sackmann, "Fluctuation analysis of tension-controlled undulation forces between giant vesicles and solid substrates," Phys. Rev. E **51**, 4526–4536 (1995).

[106] A.Hategan, K.Sengupta, S.Kahn, and E.Sackmann, "Topographical pattern dynamics in passive adhesion of cell membranes," Biophys.J. **87**, 3547–3560 (2004).

[107] G.Wiegand, T.Jaworek, G.Wegner, and E.Sackmann, "Studies of structure and local wetting on heterogeneous micropatterned solid surfaces by microinterferometry," J.Colloid.Interface.Sci. **196**, 299–312 (1997).

[108] L.Vonna, L.Limozin, A.Roth, and E.Sackmann, "Single-filament dynamics and long-range ordering of semiflexible biopolymers under flow and confinement," Langmuir. **21**, 9635–9643 (2005).

[109] J.Rädler and E.Sackmann, "On the measurement of weak repulsive and frictional colloidal forces by reflection interference contrast microscopy," Langmuir. **8**, 848–853 (1992).

[110] K.Sengupta, J.Schilling, S.Marx, M.Fischer, A.Bacher, and E.Sackmann, "Mimicking tissue surfaces by supported membrane coupled ultrathin layer of hyaluronic acid," Langmuir. **19**, 1775–1781 (2003).

[111] J.Schilling, K.Sengupta, S.Goennenwein, A.R.Bausch, and E.Sackmann, "Absolute interfacial distance measurements by dual-wavelength reflection interference contrast microscopy," Phys. Rev. E **69**, 021 901 (2004).

[112] C.Picart, K.Sengupta, J.Schilling, G.Maurstad, G.Ladam, A.R.Bausch, and E.Sackmann, "Microinterferometric study of the structure, interfacial potential, and viscoelastic properties of polyelectrolyte multilayer films on a planar substrate," J.Phys.Chem.B. **108**, 7196–7205 (2004).

[113] G.Wiegand, K.R.Neumaier, and E.Sackmann, "Microinterferometry: Three-dimensional reconstruction of surface microtopography for thin-film and wetting studies by reflection interference contrast microscopy(RICM)," J.Appl.Opt. **37**, 6892–6905 (1998).

[114] H.Wu and M.A.Bevan, "Direct measurement of single and ensemble average particle-surface potential energy profiles," Langmuir. **21**, 1244–1254 (2005).

[115] A.L.Hiddessen, D.A.Weitz, and D.A.Hammer, "Rheology of binary colloidal structures assembled via specific biological cross-linking," Langmuir. **20**, 6788–6795 (2004).

[116] S.G.Boxer, "Molecular transport and organization in supported lipid membranes," Curr. Opin. Chem. Biol. **4**, 704–709 (2000).

[117] R.Parthasarathy, P.A.Cripe, and J.T.Groves, "Electrostatically driven spatial patterns in lipid membrane composition," Phys. Rev. Lett. **95**, 048 101 (2005).

[118] D.Velegol and P.K.Thwar, "Analytical model for the effect of surface charge nonuniformity on colloidal interactions," Langmuir. **17**, 7687–7693 (2001).

[119] S.Perkin, N.Kampf, and J.Klein, "Long-range attraction between charge-mosaic surfaces across water," Phys. Rev. Lett. **96**, 038 301 (2006).

[120] G.M.Kuziemko, M.Stroh, and R.C.Stevens, "Cholera toxin binding affinity and specificity for gangliosides determined by surface plasmon resonance," Biochemistry **35**, 6375–6384 (1996).

[121] J.C.Neu, "Wall-mediated forces between like-charged bodies in an electrolyte," Phys. Rev. Lett. **82**, 1072–1074 (1999).

[122] V.Yamazaki, O.Sirenko, R.J.Schafer, and J.T.Groves, "Lipid mobility and molecular binding in fluid lipid membranes," J.Am.Chem.Soc. **127**, 2826–2827 (2005).

[123] E.W.Gomez, N.G.Clack, H.Wu, and J.T.Groves, "Like-charge interactions between colloidal particles are asymmetric with respect to sign," Soft Matter. **5**, 1931–1936 (2009).

[124] M.Brunner, J.Dobnikar, and H.V.Grünberg, "Direct measurement of three-Body interactions amongst charged colloids," Phys. Rev. Lett. **92**, 078301 (2004).